Astronomy & Astrophysics manuscript no. aanda_rev2_2col
November 12, 2020

Physics of ULIRGs with MUSE and ALMA: The PUMA Project

I. Properties of the Survey and first MUSE data results

M. Perna[1,2⋆], S. Arribas[1], M. Pereira Santaella[1], L. Colina[1], E. Bellocchi[3], C. Catalán-Torrecilla[1], S. Cazzoli[4], A. Crespo Gómez[1], R. Maiolino[5,6], J. Piqueras López[1], and B. Rodríguez del Pino[1]

[1] Centro de Astrobiología, (CAB, CSIC–INTA), Departamento de Astrofísica, Cra. de Ajalvir Km. 4, 28850 – Torrejón de Ardoz, Madrid, Spain
[2] INAF - Osservatorio Astrofisico di Arcetri, Largo Enrico Fermi 5, I-50125 Firenze, Italy
[3] Centro de Astrobiología (CSIC-INTA), ESAC Campus, 28692 Villanueva de la Cañada, Madrid, Spain
[4] IAA - Instituto de Astrofísica de Andalucía (CSIC), Apdo. 3004, 18008, Granada, Spain
[5] University of Cambridge, Cavendish Laboratory, Cambridge CB3 0HE, UK
[6] University of Cambridge, Kavli Institute for Cosmology, Cambridge CB3 0HE, UK

Received September 15, 1996; accepted March 16, 1997

ABSTRACT

Context. Ultraluminous infrared galaxies (ULIRGs) are characterised by extreme starburst (SB) and active galactic nucleus (AGN) activity, and are therefore ideal laboratories to study the outflow phenomena and their feedback effects. We have recently started the "Physics of ULIRGs with MUSE and ALMA" (PUMA) project, a survey of 25 nearby ($z < 0.165$) ULIRGs observed with the integral field spectrograph MUSE and the interferometer ALMA. This sample includes systems with both AGN and SB nuclear activity in the pre- and post-coalescence phases of major mergers.
Aims. The main goals of the project are: (i) study the prevalence of (ionised, neutral and molecular) outflows as a function of the galaxy properties, (ii) constrain the driving mechanisms of the outflows (e.g. discriminate between SB and AGN winds), (iii) identify and characterise the presence of feedback effects on the host galaxy. In this first paper, we present details on the sample selection, MUSE observations and data reduction, and the derivation of first high-level data products.
Methods. MUSE data cubes are analysed to study the dynamical status of each of the 21 ULIRGs so far observed, taking into account the stellar kinematics and the morphological properties inferred from MUSE narrow-band images. We also locate the ULIRG nuclei, taking advantage of near-infrared (HST) and mm (ALMA) data, and study their optical spectra to infer (i) the ionisation state via standard optical line ratio diagnostics, and (ii) the presence of outflows in both atomic ionised ([OIII], Hα) and neutral (NaID) gas.
Results. We show a good consistency between the morphological and stellar kinematic classifications, proving that post-coalescence systems are more likely associated with ordered motions, while interacting (binary) systems are dominated by non-ordered and streaming motions. We also find broad and asymmetric [OIII] and NaID profiles in almost all nuclear spectra, with linewidths in the range [300 – 2000] km/s, possibly associated with AGN- and SB-driven winds. This result reinforces previous findings indicating that outflows are ubiquitous during the pre- and post-coalescence phases of major mergers.

Key words. Galaxies:active - Galaxies: starburst - Galaxies: ISM - Galaxies: interactions

1. Introduction

Theory and observations suggest that galaxies are open systems that evolve into a quasi-stationary state, where flows of baryons determine the growth and evolution of their stellar populations and the supermassive black hole (BH) at their center (see e.g. Schaye et al. 2010; Bothwell et al. 2013; Sánchez Almeida et al. 2014; Hopkins et al. 2016; Naab & Ostriker 2017; Dekel et al. 2019). Gas accretion from the cosmic web or from merging interactions trigger star formation (SF) and active galactic nuclei (AGN) activity; in turn, the energy released by the AGN and the stars heat and push the surrounding interstellar medium (ISM), regulating with feedback mechanisms the formation of new stars and the accretion onto the BH (e.g. Silk 2013; Hopkins 2012; Hopkins et al. 2016). The role of these outflows is believed to be crucial, as they not only regulate (and possibly quench) SF, but also redistribute dust and metals over large distances within the galaxy, or even expel them into the circumgalactic and intergalactic media (e.g. Veilleux et al. 2005, 2020). In this scenario, the galaxy mass function (e.g. Somerville & Davé 2015), the mass-metallicity relation (Maiolino & Mannucci 2019), and the black hole-spheroid mass correlation (Kormendy & Ho 2013), are shaped by outflows.

Although this general scenario is relatively well established, many details of the processes involved remain largely unknown. An intrinsic difficulty is associated to the fact that the self-adjusted balance among gas accretion, gas outflow and SF/AGN activity depends on the coupling between physical processes that involve multi-phase (ionised, neutral and molecular) gas at very different physical scales, from cosmic web structures and mergers to molecular clouds (where SF occurs), and the vicinity of the BH (Sánchez Almeida et al. 2014).

In recent years, the study of outflows at high-z has gained much interest. Being the Early Universe characterised by episodes of intense SF and AGN activity (Madau & Dickinson 2014), models predict that the presence of powerful outflows had a key role in shaping primeval galaxies and their subsequent evo-

⋆ E-mail: mperna@cab.inta-csic.es

lution (e.g. Ceverino et al. 2018; Pillepich et al. 2018; Davé et al. 2019). Although the observational constraints provided by current facilities are limited, they indeed suggest that galactic winds are highly prevalent at the peak of SF ($z \sim 1-3$; e.g. Genzel et al. 2014; Brusa et al. 2015; Carniani et al. 2016; Föerster-Schreiber et al. 2018; Villar Martín et al. 2020; Kakkad et al. 2020), and may be extremely powerful at very early epochs (e.g. Maiolino et al. 2012; Bischetti et al. 2019).

Local ultraluminous infrared galaxies (ULIRGs, with rest-frame [8 − 1000 μm] L_{IR} in excess of $10^{12} L_{\odot}$) are powered by strong SBs (Genzel et al. 1998) and/or AGN (Nardini et al. 2010), and therefore are ideal laboratories to study the outflow phenomena. While scarce in the nearby universe, luminous star-forming galaxies (SFGs) are much more numerous at high-z, being responsible for $\sim 50\%$ of the total star-formation rate (SFR) density at $z \sim 2$ when their number density is a factor ~ 800x higher than locally (e.g., Pérez-González et al. 2005; Magnelli et al. 2013; Casey et al. 2014). For high-z luminous SFGs, however, some properties may differ of those of their local counterparts. While local ULIRGs are dominated by strong interactions and major mergers, recent morphological studies have found that distant luminous SFGs appear to be a mixture of merging, interacting systems and disk galaxies (e.g., Arribas et al. 2012; Kartaltepe et al. 2012; Kaviraj et al. 2013; Hung et al. 2014; Alcorn et al. 2019; Wisnioski et al. 2018), and, therefore, a fraction may maintain their large observed SFRs by continuous gas accretion via cold gas flows and minor mergers (Ocvirk et al. 2008; Dekel et al. 2009). Nevertheless, local ULIRGs offer the opportunity of investigating the properties of strong outflows and their feedback effects at similar SFR levels that observed at high-z, but at much higher spatial resolution and signal-to-noise ratio.

ULIRGs have been in the past the target of numerous studies, which have demonstrated the presence of ionized (e.g. Heckman et al. 1990; Colina et al. 1999; Bedregal et al. 2009; Colina et al. 2012; Westmoquette et al. 2012; Rupke & Veilleux 2013a; Rodríguez Zaurín et al. 2013; Bellocchi et al. 2013; Arribas et al. 2014; Rich et al. 2011, 2015), neutral (e.g. Martin 2005; Rupke et al. 2005a,b,c; Rupke & Veilleux 2013a; Cazzoli et al. 2016), and molecular (e.g. Feruglio et al. 2010; Sturm et al. 2011; Spoon et al. 2013; Veilleux et al. 2013; Rupke & Veilleux 2013b; Cicone et al. 2014; Emonts et al. 2018; Pereira-Santaella et al. 2018; Fluetsch et al. 2019) outflows. Most of these previous works, however, are limited to the study of a specific gas phase, or have resolutions unable to trace in detail the outflow structure.

To overcome these limitations, we have recently started a project aimed at studying the outflow phenomena in a sample of 25 representative ULIRGs, based on integral field spectroscopy (IFS) with MUSE at the VLT and interferometric ALMA data (PUMA: "Physics of ULIRGs with MUSE and ALMA"). The combination of the data provided by these two facilities offers the possibility to study the multi-phase structure of the outflow at sub-kpc angular resolutions over a field of view (FOV) that covers the main body of the system. The key goals of this project include: i) to study prevalence of outflows as a function of the galaxy and BH properties, ii) to establish the relative role of the different gas phases in gas flows, iii) to constrain the driving mechanisms of the outflow (e.g. discriminate between SB and AGN driven winds), iv) to identify and characterise the presence of negative and/or positive feedback, and quantify their effects on the host galaxy. The first such a detailed study of the multi-phase, galaxy-scale outflows has been recently presented for the closest ULIRG in our sample, Arp 220 (Perna et al. 2020).

In this paper, we present the MUSE data for the entire PUMA sample, required to trace and characterise the ionized and neutral components of the outflows, while in Pereira-Santaella et al. (in prep.) we describe the associated ALMA data to study the molecular phase. The present MUSE data represent a significant improvement in quality with respect to previous surveys of ULIRGs based on the use of first generation IFS instruments like INTEGRAL (García-Marín et al. 2009a,b) and VIMOS (Arribas et al. 2008). The MUSE data presented here will also provide a complementary view of outflow phenomena with respect to other MUSE surveys, for instance targeting local Seyfert galaxies (e.g. MAGNUM, Mingozzi et al. 2019; CARS, Husemann et al. 2019), whose outflows would likely originate from AGN, or galaxies with prominent nuclear rings and bars (TIMER, Gadotti et al. 2019), whose outflows would probably originate from AGN/SB activity triggered by secular processes.

The present manuscript is organized as follows. In Sect. 2 we describe the sample selection. Section 3 presents the MUSE observations and data reduction. In Sect. 4 we describe the main morphological properties of our ULIRGs, as inferred from MUSE optical continuum and line features structure, and from HST near-infrared (near-IR) images. In Sect. 5 we describe the dynamical status of each ULIRG, taking into account the morphological properties and the stellar kinematics derived in this work. Section 6 presents the nuclear gas properties inferred from the analysis of MUSE spectra, in terms of ionisation conditions and presence of multi-phase (ionised and neutral) outflows. Finally, Sect. 7 summarises our conclusions. Throughout this paper, we adopt the cosmological parameters $H_0 = 70$ km/s/Mpc, $\Omega_m = 0.3$ and $\Omega_\Lambda = 0.7$.

2. Sample selection

The PUMA project is designed to investigate the main properties of outflows in a representative distance-limited (< 800 Mpc, $z < 0.165$) sample of ULIRGs. The targets are selected to cover the widest possible range in host galaxy properties, like: (i) activity class (i.e., considering systems with both AGN and SB nuclear activity); (ii) interaction stage (from advanced interacting pairs to mergers); and (iii) 8 − 1000 μm IR luminosity.

The parent sample is assembled from the IRAS 1 Jy Survey (Kim & Sanders 1998), the IRAS Revised Bright Galaxy sample (Sanders et al. 2003), and the Duc et al. (1997) catalogue. From these surveys, we select ULIRGs with declination between −65 and +20 degrees, and within the required distance range (i.e. $z < 0.165$). We also request the targets to have mid-IR Spitzer spectroscopy, to reliably estimate the AGN contribution even if it is completely obscured at optical wavelengths (e.g., Veilleux et al. 2009, 2013; Spoon et al. 2013). More than 80% of the general population of ULIRGs are in close pairs or in already coalescence systems (Veilleux et al. 2002). Therefore, we focus our sample on advanced interacting systems with nuclear projected separations smaller than 10 kpc (i.e., systems classified as IIIb, IV and V under the Veilleux et al. 2002 scheme). There are 44 systems fulfilling all these criteria, from which we select 23 objects which uniformly sample the parameter space discussed above. In particular, about half (12) of the systems are pre-mergers of type IIIb (interacting stage hereinafter), while the rest of targets are in the later type IV and V (merger) stages.

The AGN contribution to the total bolometric luminosity, α_{AGN}, has been derived considering the 30 to 15 μm flux ratio (following Veilleux et al. 2013): a median value of 32% is obtained for both the selected sample of 23 targets, as well as for the parent sample of 44 objects. We will consider targets with α_{AGN} above this median value as significantly affected by the AGN. We also add to the group of 23 targets the Arp220 system

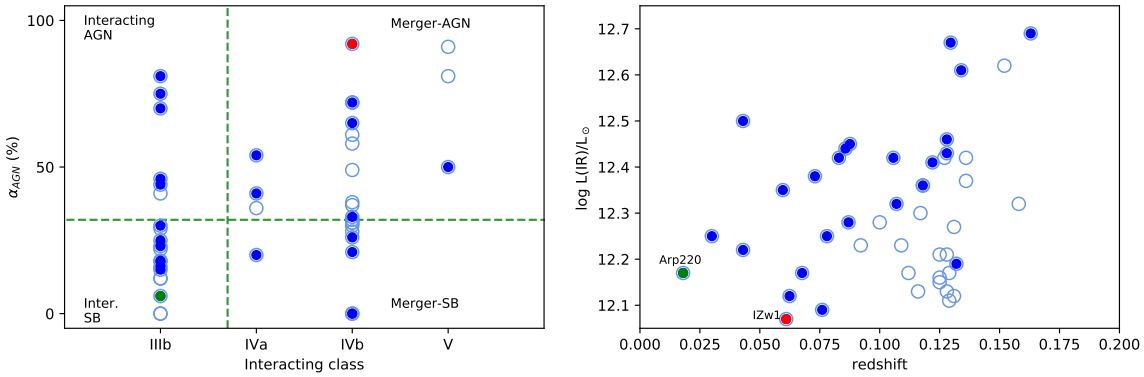

Fig. 1. Sample properties. Parent sample formed by the 44 targets that meet the selection criteria (empty and solid blue circles), and the 25 objects selected for the MUSE-ALMA sample (filled blue circles), including Arp220 (green) and IZw1 (red). See text for selection details. *Left*: interacting class classification, according to the Veilleux et al. (2002) scheme, versus contribution of the AGN to the total luminosity, according to method 6 of Veilleux et al. (2009). The vertical green line distinguishes between interacting galaxies and mergers in a more simplified classification; the horizontal line is used to separate SB and AGN targets. *Right*: redshift versus IR luminosity. For IZw1 the bolometric luminosity is considered instead of L_{IR}.

(despite of having a slightly higher declination) and the IZw1 galaxy (whose infrared luminosity does not meet the ULIRG criterion, though $L_{bol} > 10^{12}$ $L_\odot$). These two systems are often considered archetypical of the local luminous SB (Arp220) and type-1 AGN (IZw1). Their inclusion does not alter either the AGN/SB, nor the interacting/merger distributions, as each of these targets belongs to one of these categories.

We finally note that all but three sources obey the well known radio−far-IR correlation, with a mean q-parameter of 2.37 (Yun et al. 2001). The only source with an excess in its radio emission is F13451+1232, with $q = -0.34$. This object hosts the powerful radio source 4C 12.50, with its twin-jet morphology (Lister et al. 2003). The systems 20087−0308 and F22491−1808 are instead associated with an infrared excess ($q = 3.009$ and 3.025, respectively; Yun et al. 2001), possibly indicating the presence of dust enshrouded AGN or compact SBs.

The so far presented properties of the final sample of 25 systems are reported in Table 1. The left panel of Fig. 1 shows the distribution of the PUMA systems in the α_{AGN}− interacting class (IC) space: the horizontal line separates SB from AGN systems, while the vertical line separates interacting from merger targets. Our selected sources uniformly sample this two-dimensional parameter space. In addition, the selected objects also uniformly sample the ULIRG luminosity range (right panel of Fig. 1).

3. MUSE observations

MUSE observations were conducted as part of our programme "Sub-kpc multi-phase gas structure of massive outflows in Ultraluminous Infrared Galaxies" (ESO projects 0103.B-0391(A) and 0104.B-0151(A), PI: Arribas). The observations presented in this paper were carried out with VLT/MUSE in its adaptive-optics assisted Wide-Field Mode (AO-WFM; Bacon et al. 2010).

MUSE observations cover a $60'' \times 60''$ field of view (FOV) with a sampling of $0.2'' \times 0.2''$, resulting in a dataset of $\sim$ 90000 individual spectra. We used the nominal instrument setup, with a spectral coverage from 4750 to 9350 Å and a mean resolution of 2.65 Å (FWHM). Because of the use of AO with sodium laser guide system, the wavelength range 5800 – 5970 Å is blocked, to avoid contamination and saturation of the detector by sodium light. Note that for our sources the NaID feature is redshifted outside this wavelength range.

The requested observations were distributed in three 40-minutes observing blocks (OBs) with a total integration time of 2 hours on source for all ULIRGs systems. We split the exposures in each OB into four (dithered and 90°-rotated) frames of 612 s each. Observations were performed with seeing $\approx 1''$; the root mean square of the flux variation was $\approx 1\%$, as measured at night by the VLT DIMM station.

70 percent of the MUSE targets (i.e. 17 out the 25) have been observed as part of our programs. A few sources have not been observed with all requested time: for instance, only one frame has been obtained for the source F16090-0139. Additional frames have been instead obtained for 07251-02448, F11095-0238 and IZw1, as their first observations were classified as Grade C. In our analysis, we combined all these additional frames, after verifying that their inclusion does not affect negatively the quality of the final data cubes.

MUSE archival data exist for 4 out of the 8 remaining targets: 13120-5453, F14378-3651, 17208-0014 and F22491-1808 (already presented in Fluetsch et al. 2020[1]). These sources have been observed in seeing-limited WFM, and with $\sim$ 30 minutes exposure times. Because of the good seeing conditions during their observations, we decided to include the archival data of these four targets in our analysis.

Therefore, our PUMA Survey so far consists of 21 ULIRGs observed with MUSE-WFM; information about the MUSE data used in this work are collected in Table 2. At the mean distance ($\sim$ 400 Mpc) the MUSE spaxel scale, resolution and FoV correspond to 0.34 kpc, 1 kpc and $\sim 100 \times 100$ kpc^2, respectively.

3.1. Data reduction and astrometry registration

MUSE observations were reduced using the MUSE EsoReflex pipeline recipes (muse - 2.6.2), which provide a fully calibrated and combined MUSE data cube. In the last step of our data reduction, we identified and subtracted the residual sky contamination in the final data-cube using the Zurich Atmosphere Purge (ZAP) software package (Soto et al. 2016; see e.g. Sect. 3 in Perna et al. 2020).

[1] Seven of our selected sources are also part of the sample presented in Fluetsch et al. (2020): IZW1, 20100-1651 and 19542+1110, for which we present higher quality data, as well as 13120-5453, F14378-3651, 17208-0014 and 22491-1808.

Table 1. Sources in the PUMA Survey of ULIRGs.

IRAS ID (Other)	RA	DEC	D	log L_{IR}	q	SB/AGN	α_{AGN}	optical type		morph	IC	NS
	($^h:^m:^s$)	($^\circ:':''$)	(Mpc)	($L_\odot$)								(kpc)
(1)	(2)	(3)	(4)	(5)	(6)	(7)	(8)	(9)	(10)	(11)	(12)	(13)
F00091-0738	00:11:43.27	−07:22:07.34	519	12.27 ± 0.03	2.81	AGN	0.46(0.58)	HII	–	I	IIIb	2.3
F00188-0856	00:21:26.51	−08:39:25.99	563	12.41 ± 0.04	2.32	AGN	0.50(0.35)	LI(N)ER	Sy 2	M	V	< 0.3
F00509+1225 (IZw1)	00:53:34.93	+12:41:35.94	243	11.30 ± 0.05 [1]	2.51	AGN	0.92	Sy 1	Sy 1	M	IVb	< 0.2
F01572+0009 (Mrk 1014)	01:59:50.25	+00:23:40.88	717	12.63 ± 0.03	2.01	AGN	0.65(0.27)	Sy 1	Sy 1	M	IVb	< 0.4
F05189-2524	05:21:01.40	−25:21:45.30	189	12.17 ± 0.01	2.72	AGN	0.72(0.30)	Sy 2	Sy 2	M	IVb	<0.1
07251-0248	07:27:37.61	−02:54:54.25	390	12.41 ± 0.04	2.76	SB	0.30(0.39)	–	HII	I	IIIb	1.8
09022-3615	09:04:12.71	−36:27:01.93	268	12.30 ± 0.01	2.21	AGN ?	0.54(0.09)	HII	HII	M	IVa	< 0.1
10190+1322	10:21:42.94	+13:06:53.83	343	12.05 ± 0.03	2.41	SB	0.17	HII	HII	I	IIIb	7.2
F11095-0238	11:12:03.38	−02:54:22.94	477	12.28 ± 0.03	2.15	AGN	0.44(0.60)	LI(N)ER	?	I	IIIb	1.1
F12072-0444	12:09:45.12	−05:01:13:31	573	12.40 ± 0.03	2.55	AGN	0.75(0.41)	Sy 2	Sy 2	I	IIIb	2.3
F12112+0305	12:13:46.06	+02:48:41.53	329	12.33 ± 0.02	2.65	SB	0.17	LI(N)ER	–	I	IIIb	4.18
13120-5453 (WKK 2031)	13:15:06.32	−55:09:22.82	139	12.25 ± 0.03	2.91	AGN	0.33(0.01)	Sy 2	Sy 2	M	IVb	< 0.1
F13451+1232	13:47:33.36	+12:17:24.24	542	12.31 ± 0.04	−0.34	AGN	0.82(0.60)	Sy 2	Sy 2	I	IIIb	4.3
F14348-1447	14:37:38.28	−15:00:24.24	370	12.35 ± 0.02	2.37	SB	0.17(0.04)	LI(N)ER	?	I	IIIb	5.45
F14378-3651	14:40:59.01	−37:04:31.93	302	12.13 ± 0.02	2.35	AGN	0.21(0.01)	Sy 2	Sy 2	M	IVa	< 0.1
F15327+2340 (Arp220)	15:34:57.22	+23:30:11.50	82	12.17 ± 0.01	2.61	SB	0.06(0.17)	LI(N)ER	LI(N)ER	I	IIIb	0.37
F16090-0139	16:11:40.42	−01:47:06.35	592	12.57 ± 0.02	2.34	SB	0.41(0.24)	LI(N)ER	HII	M	IVa	<0.7[2]
F16156+0146	16:18:09.37	+01:39:21.76	585	12.11 ± 0.06	2.18	AGN	0.70(0.40)	Sy 2	–	I	IIIb	8.26
17208-0014	17:23:21.96	−00:17:00.86	189	12.50 ± 0.02	2.70	SB	0.00 (0.11)	HII	LI(N)ER	M	IVb	< 0.1
F19297-0406	19:32:22.30	−04:00:01.80	376	12.40 ± 0.02	2.49	SB	0.23(0.01)	HII	?	I	IIIb[3]	1.1
19542+1110	19:56:35.78	+11:19:05.03	284	12.12 ± 0.04	2.55	SB	0.26(0.04)	LI(N)ER	LI(N)ER	M	IVb	< 0.1
20087-0308	20:11:23.87	−02:59:50.71	463	12.44 ± 0.03	3.01	SB	0.20(0.03)	LI(N)ER	LI(N)ER	M	IVa	< 0.9
20100-4156	20:13:29.56	−41:47:35.21	571	12.64 ± 0.02	2.49	SB	0.26(0.20)	HII	LI(N)ER	I	IIIb	6.5
F20414-1651	20:44:18.16	−16:40:16.82	381	12.30 ± 0.08	2.47	SB	0.00	HII	–	M	IVb	< 0.2
F22491-1808	22:51:49.24	−17:52:23.66	339	12.19 ± 0.03	3.03	SB	0.15	HII	HII	I	IIIb	2.7

Note. Column (1): IRAS identification code (alternative name); (2) and (3): RA and DEC coordinates of the ULIRG nuclei, from this work; for binary systems, we report the coordinates of the near-IR brightest nucleus; (4): Hubble distance (from NED); (5): IR luminosity; (6): q radio-IR parameter (Condon et al. 1991); (7): simplified AGN/SB classification based on the information provided in columns (8) and (9); (8): fraction of AGN contribution to L_{bol} derived from the 30 to 15 μm flux ratio ($f30/f15$). Note that this ratio gives a good first order approach to contribution of the AGN to L_{bol}, as it agrees within 10 − 15% to the average value of the six methods considered in Veilleux et al. (2009). In order to homogenise the various calibrations of this ratio, we have taken as reference the results of Veilleux et al. (2013) and fit a second order polynomial to the $\log(f30/f15)$ function. The flux ratio values are from Veilleux et al. (2009, 2013) and Spoon et al. (2013). In brackets values according Nardini et al. (2010) method, which is based on the analysis of the 5 − 8 μm spectral range; (9-10) optical spectral type according to Veilleux et al. (2009, 2013), in column 9, and according to our classification obtained from nuclear spectra (Sect. 6), in column 10; (11): simplified morphology classes (I: interacting, M: mergers). See text for details; (12): IC according to the scheme by Veilleux et al. (2002), obtained from Veilleux et al. (2009) or derived from HST imaging; (13): Nuclear Separation, from Veilleux et al. (2009), Duc et al. (1997), and Kim et al. (2013).

[1] [40 − 500] μm IR luminosity from Petric et al. (2015). Note that this target does not meet the infrared luminosity criterion for being a ULIRG (though $L_{bol} > 10^{12}$ $L_\odot$), but it has been included as usually considered an archetypical type-1 AGN.

[2] No HST images are available for F16090-0139; therefore, the NS upper limit has been obtained on the basis of our ALMA images (Pereira-Santaella et al., in prep).

[3] **F19297-0406, originally associated with a single nucleus (Kim et al. 2013), is here classified as a IIIb system, because of the detection of two nuclei in near-IR HST and ALMA (Pereira-Santaella et al., in prep) images.**

We estimated the spatial resolution from the foreground stars in the MUSE FOV for all but Arp220 and F11095−0238, for which no stars are detected. For each bright star in the FOV, we performed a 2D Gaussian fit, and derived an estimate for the angular resolution from the FWHM of the Gaussian fit. The spatial resolution in the data cube of F11095−0238 has been obtained from a 2D Gaussian fit of the broad line region (BLR) emission of a QSO at z ∼ 2.2 (CXOGSG J111204.2-025415); Arp220 spatial resolution has been taken from Perna et al. (2020). Overall, thanks to the MUSE seeing enhancer mode (and the good seeing conditions during the acquisition of noAO-WFM data), we reached an average resolution of ∼ 0.7″, corresponding to physical scales in the range ∼ 0.2 − 2 kpc depending on the redshift of the system (Table 2).

The astrometric registration has been performed using the Gaia DR2 catalog (Gaia Collaboration 2018). We created continuum maps from the MUSE observations (see Sect. 4 and Fig. 2) where we measured the position of all the Gaia DR2 stars present in the MUSE FOV. Then, we shifted the MUSE cube astrometric solution to minimize the difference between the Gaia sky coordinates of these stars and those derived from the MUSE data. We took into account the proper motions of the stars as listed in the Gaia catalog. For most systems, we used between 2 and 35 Gaia stars to perform this correction. For 5 systems (F05189-2524, F12071-0444, F13451+1232, F14348-1447 and F11095-0238), less than 2 Gaia stars were available in the MUSE FOV; therefore, we used as reference HST optical images (F814W) whose astrometry was tied to Gaia DR2 using the method described above. Then, we used objects detected in both the HST and MUSE images to determine the MUSE astrometric solution. HST near-IR images (F160W) astrometry was similarly tied to Gaia DR2. We estimate an average uncertainty in the MUSE astrometric solution of 0.15″(0.7 MUSE spaxels) based on the comparison between measured and expected coordinates of the Gaia stars.

4. Stellar and ionized gas distributions

In order to appreciate the MUSE data quality and its scientific potential, in this section we present three-colour, continuum and emission line maps built directly from the MUSE data cubes, and briefly describe the general properties that can be inferred from

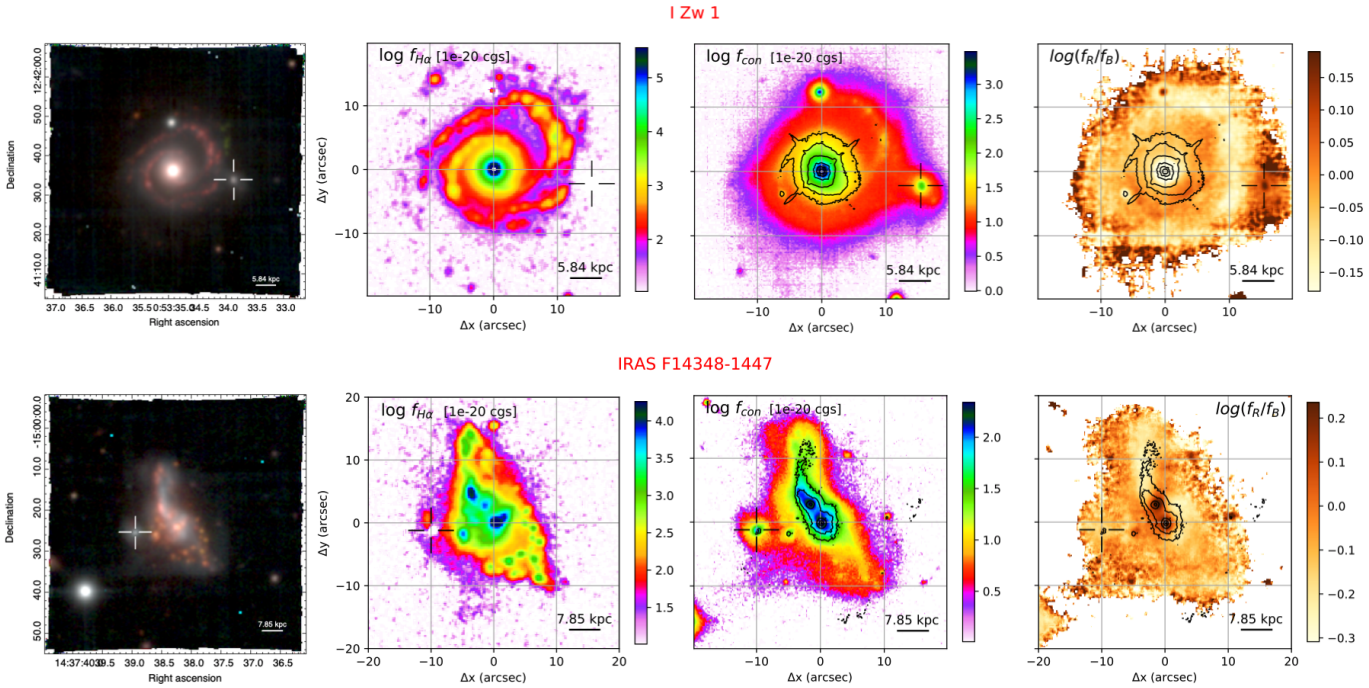

Fig. 2. IZw1 (top) and F14348-1447 (bottom) MUSE images. *Left column*: colour composite optical image, showing [OIII] (green), Hα (red) and continuum emission (blue). *Second column*: Hα map obtained collapsing the MUSE data cube on the emission line, after subtracting the continuum using adjacent regions at shorter and longer wavelengths. *Third column*: Red continuum ($\approx$ 8500Å) image from MUSE, with contours from HST/F160W. *Right column*: continuum colour map obtained from MUSE, by dividing the red continuum image ($\approx$ 8500Å) by the blue image ($\approx$ 4500Å); contours from HST/F160W. See Appendix C for further details. The cross markers in the panels show the detected satellites in the MUSE FOV.

them. A full characterization of the systems, similar to the one obtained for Arp220 (Perna et al. 2020; Catalán Torrecilla et al., in prep.), will be presented in future papers.

In particular, in this section we present the maps for two representative targets in our sample: IZw1, the type 1 AGN archetypical, hosted by an ongoing minor-merger (e.g. Scharwächter et al. 2007), and the ULIRG F14348-1447, a SB-dominated interacting system. Colour and flux images for the remaining targets in our sample are presented in Appendix C.

4.1. Color composite maps

Colour composites of the two representative targets are shown in Fig. 2 (left column). These maps are built using three images derived by collapsing the MUSE data cubes along the wavelength direction. The green and red images cover the [OIII]λ5007 ([OIII] hereinafter) and Hα line transitions[2] (with underlying continuum emission), respectively; the blue image is associated with the continuum emission at bluest wavelengths. The blue, green and red images have identical colour-bar scales and limits, and are combined to obtain an approximation to the actual relative contributions (and extensions) of [OIII], Hα and stellar continuum emission in the ULIRGs.

These composites provide a first-order description of the ULIRGs morphologies. Compact and regular galactic structures are observed only in three targets: IZw1 (Fig. 2, top-left), F00188-0856 (Fig. C.1) and 19542+1110 (Fig. C.74). The remaining ULIRGs present irregular morphologies (e.g. elongated along the merger axis; e.g. Fig. 2, bottom-left) and bright tidal tails extended over tens of kpc (e.g. Fig. C.22).

The three-colour images also allow us to compare continuum and ionised gas distribution, providing a hint of the physical processes in the ULIRGs. Hα emission generally matches the stellar continuum distributions, both in the innermost nuclear regions, tracing SB or AGN activity, and in the outer regions, tracing more diffuse ionised gas. Clumpy Hα emission is also detected along tidal arms. In a few targets, the [OIII] dominates over continuum and Hα emission, possibly indicating AGN ionisation conditions (see e.g. IZw1 nuclear and north-west regions in Fig. 2, top-left).

Finally, these images provide a first-order identification of foreground stars, generally associated with bright point-like sources, and galaxies at different redshifts, showing a heterogeneous mix of morphologies, colours and sizes (see also e.g. Perna et al. 2020). Nine ULIRGs in our sample present between one and two nearby satellites in the MUSE FOV, at projected distances from $\approx$ 5 to $\approx$ 50 kpc (see e.g. cross markers in Fig. 2), and with velocities within a few 100s km/s from the ULIRG systemics (Table A.1). A more detailed description of ULIRGs structures and environmental properties is reported in Sect. 5.3, where we combine optical (MUSE) and near-IR (HST) imaging information with stellar kinematics results.

4.2. Ionised gas and continuum emission maps

In Fig. 2 we also display the Hα maps (second column), the red continuum emission (third column), and the continuum colour

[2] For each target, we selected the wavelength ranges covering the [OIII] lines taking into account the line velocity variations observed across the MUSE FOV; the Hα maps have been constructed in similar fashion, but reducing the velocity range to avoid the contamination from the [NII] doublet. The individual wavelength ranges used to produce composite images are reported in the figures captions in Appendix C.

Table 2. MUSE observations resolutions and exposure times

IRAS ID	resolution (″ / kpc)	seeing (″)	t_{exp} (h)
(1)	(2)	(3)	(4)
F00188-0856	0.70 / 1.60	0.7	0.68
IZw1	0.70 / 0.80	0.8	2.72
F01572+0009	0.70 / 2.00	0.8	2.04
F05189−2524	0.60 / 0.50	0.7	2.04
07251−0248	0.55 / 0.45	0.7	2.55
09022−3615	0.60 / 0.70	0.9	2.04
10190+1322	0.7 / 1.00	0.8	2.04
F11095−0238	0.75 / 1.50	0.9	2.72
F12072−0444	0.80 / 1.90	0.8	0.68
13120−5453*	0.90 / 0.60	0.9	0.52
F13451+1232	0.75 / 1.70	0.9	2.04
F14348−1447	0.70 / 1.10	1.0	0.68
F14378−3651*	0.90 / 1.10	1.0	0.47
Arp220	0.55 / 0.20	1.0	0.65
F16090−0139	0.70 / 1.70	1.1	0.17
17208−0014*	0.55 / 0.45	0.4	0.39
F19297−0406	0.65 / 1.05	1.0	2.04
19542+1110	0.70 / 0.80	0.7	2.04
20087−0308	0.70 / 1.40	1.1	2.04
20100−4156	0.60 / 1.40	0.8	2.04
F22491−1808*	0.50 / 0.70	0.4	0.41

Note. Column (1): IRAS identification code. (2): measured angular resolution at 7000Å, and physical scale at the redshift of the detected target. (3): mean DIMM seeing during the time of the observation. (4) total integration time.
*: noAO-MUSE observations, from the programs 0102.B-0617(A) (13120-5453 and F14378-3651) and 0101.B-0368(B) (17208-0014 and F22491-1808).

maps (right column) for IZw1 and F14348-1447. In the last two columns, we show the HST/F160W emission with black contours. The Hα maps are obtained by collapsing the MUSE data cube on the emission line, after subtracting the continuum using adjacent regions at shorter and longer wavelengths; the red image is associated with the continuum emission at reddest wavelengths - but avoiding the range 9000 – 9300Å (observer-frame), sometimes affected by bad background subtraction; the continuum colour maps are instead built by dividing the red image by a blue one, derived by collapsing the MUSE data cube at wavelengths around ≈ 4500 Å. These maps are centred on the position of the ULIRGs nuclei, corresponding to the peak emission in the near-IR HST images (black contours in Fig. 2). For F14348-1447 (and other systems with double nuclei), the zero-position corresponds to the brightest nucleus in the HST/F160W image. Hα and continuum emission maps for the entire sample are reported in Appendix C.

The inspection of these images allows us a first identification of bright star forming clumps in the outermost regions, associated with strong Hα and blue continuum emissions (e.g. along the IZw1 galactic arms in Fig. 2), or old stellar populations with faint (or absent) Hα and red spectra (e.g. in the IZw1 west satellite). Tidal tails in our sample show both red and blue continuum emission (see e.g. Fig. C.22); blue tails are generally associated with Hα emission, suggesting the presence of certain sign of recent SF (e.g. Yuan et al. 2018).

The ULIRG innermost regions usually show strong Hα emission and red continuum, also associated with bright near-IR emission (black contours) in almost all our targets. This is reasonably due to the severe channelling of gas and dust during the merger process, capable of triggering intense AGN and SB activities (responsible of the Hα nuclear emission). A non-perfect match between the MUSE optical and HST near-IR peak positions is instead observed for 09022-3615, 17208-0014 and the W nucleus of F22491-1808: These discrepancies could be explained considering an even higher nuclear extinction, associated with cold circumnuclear material (Pereira-Santaella et al., in prep.) or with the presence of dust lanes across the galaxy cores (see e.g Fig. C.63). Blue nuclear spectra are observed in IZw1 (Fig. 2, top-right) and F01572+0009 (Fig. C.9), the two Seyfert 1 galaxies in our sample.

In Appendix C we also report [OIII] and [SII]$\lambda\lambda$6716, 31 maps for all targets. Hα emission is generally brighter and more extended than [OIII]: the former is generally detected in plumes, filaments and extended arcs (e.g. Fig. C.32) as well as in compact clumps (e.g. Fig. C.23), possibly indicating the presence of shocks (e.g. when bright [SII]$\lambda\lambda$6716, 31 is also detected) or SF activity.

Overall, ionised gas and continuum emission maps display a great richness in spatial details at different spatial scales. In all cases, they reveal the presence of different levels of galaxy interaction and strong nuclear activity, in line with their ULIRG nature.

5. Dynamical status

5.1. Stellar features modelling

We used the penalized pixel fitting routines (pPXF; Cappellari & Emsellem 2004; Cappellari 2017) to extract the stellar kinematics. We made use of the Indo-U.S. Coudé Feed Spectral Library (Valdes et al. 2004) as stellar spectral templates to model the stellar continuum emission and absorption line systems. The models, with a spectral resolution of 1.35Å, were broadened to the (wavelength dependent) spectral resolution of the MUSE data (∼ 2.6 – 2.9Å) before the fitting process (see e.g. Husser et al. 2016). pPXF fits were performed on binned spaxels using a Voronoi tessellation (Cappellari & Copin 2003) to achieve a minimum signal-to-noise S/N > 16 per wavelength channel on the continuum in the vicinity of the MgIb transitions. We note however that in the innermost nuclear regions, a large fraction of the original spaxels remains unbinned, because of the high quality of the MUSE data.

The entire wavelength range covered with MUSE (i.e. 4700-9300Å, observer-frame) was used in our analysis to model the stellar component and recover the stellar kinematics, after masking all optical emission lines detected in the data cubes. As the presence of broad emission lines alter the local continuum and the stellar absorption profiles causing bad pPXF fits, we used wider masks in the spatial regions where broad profiles are detected; for the two Sy 1 sources, much broader masks were used for the BLR lines in the innermost nuclear regions. In addition, we masked the resonant NaID transitions, as both stellar and interstellar absorption can be at the origin of these lines. Finally, we excluded from the analysis a narrow wavelength region at ≈ 7630Å (observer frame), associated with strong sky-subtraction residuals, and the region 5800-5970Å which is blocked by a filter to avoid contamination from the AO lasers (see Sect. 3).

During the fitting procedure, we used fourth-order multiplicative Legendre polynomials to match the overall spectral shape of the data. These polynomials are generally used instead of an extinction law, which was found to produce worse fits to the stellar continuum, and allow to correct for small inaccuracies in the flux calibration (see e.g. Belfiore et al. 2019).

5.2. Stellar velocity fields and velocity dispersion maps

pPXF best-fit results have been used to derive the systemic redshift of the ULIRGs. In particular, for the sources with one nucleus, we derived the zero-velocity measuring the stellar kinematics at the position of the nucleus; when two nuclei are instead detected, we set the $V_* = 0$ km/s measuring the stellar kinematics at the position of the brightest nucleus in the red wavelengths. The target 09022-3615 does not show well defined nuclear regions in the available HST images (covering the rest-frame UV and optical regimes); therefore, the nucleus of this target was located on the basis of ALMA mm continuum and CO(2-1) emission line maps (Pereira-Santaella et al., in prep.). Finally, for the two Sy 1 sources with strong continuum and BLR emission in the central regions (preventing the detection of stellar features), the systemic redshifts have been chosen to obtain a symmetric stellar velocity gradient along their major axis, taking advantage of their well defined rotational patterns (see below). All spectroscopic redshifts are reported in Table A.1, together with the coordinates of the nuclei; in this table, we also report the position and spectroscopic (pPXF) redshifts of the ULIRGs nearby companions detected in the MUSE data cubes.

Figure 3 shows the IZw1 (top) and F14348-1447 (bottom) stellar kinematic maps derived from pPxF analysis. In Appendix C we report the stellar kinematic maps for all ULIRGs in our sample. An ordered disk-like rotation can be observed in IZw1, as well as in other ten ULIRGs in our sample (e.g. Figs. C.3 and C.15). These galaxies show a well defined velocity gradient axis, with line-of-sight velocity amplitudes of $\approx \pm 100$ km/s. They also present regular velocity dispersion configurations, with σ_* of a few 100s km/s in the nuclear regions, and σ_* close to the MUSE spectral resolution outside. However, signatures of tidal interactions are present in many of them, especially in the outermost regions (e.g. Figs. C.11 and C.43).

F14348-1447 (Fig. 3, bottom) shows a kinematic axis following the ULIRGs elongated structure, on scales of $\approx$ 30 kpc and with amplitudes up to $\approx \pm 150$ km/s. The velocity dispersion map is quite irregular, although higher σ_* ($\approx$ 120 km/s) can be found at the location of its nuclei. 20087-0308 (Fig. C.78) and F22491-1808 (Fig. C.87) show very similar characteristics. Their kinematics are therefore reasonably strongly affected by the interaction of the merging galaxies.

Different configurations can be instead observed in 09022-3615 (Fig. C.24), F12072-0444 (Fig. C.38), F13451+1232 (Fig. C.47) and 20100-4156 (Fig. C.82): they show clear evidence of non-rotational motions, without preferential velocity gradient axes and with high σ_* (> 100 km/s) over the entire systems. Also for these ULIRGs, therefore, the stellar kinematics are reasonably dominated by tidal forces.

Finally, F11095-0238 (Fig. C.33) and F16090-0139 (Fig. C.61) do not show clear kinematic patterns. F11095-0238 pPXF maps could suggest a nearly face-on orientation, because of the small velocity amplitudes across the system, and the relatively higher σ_* in the innermost nuclear regions. The unconstrained kinematics in F16090-0139 are instead probably due to its very short exposure time (and low S/N).

We stress here that more regular kinematics could be present on sub-kpc scales in the innermost nuclear regions, and in the vicinity of the nuclei of binary systems (see e.g. Medling et al. 2014), even when large-scale motions are irregular or are dominated by streams. For instance, Pereira-Santaella et al. (2018) reported the presence of circumnuclear molecular disks around the F14348-1447 SW and NE nuclei. More detailed investigation of sub-kpc motions in individual systems will be presented in a forthcoming paper; here we focus on the main (kpc-scale) stellar kinematic features.

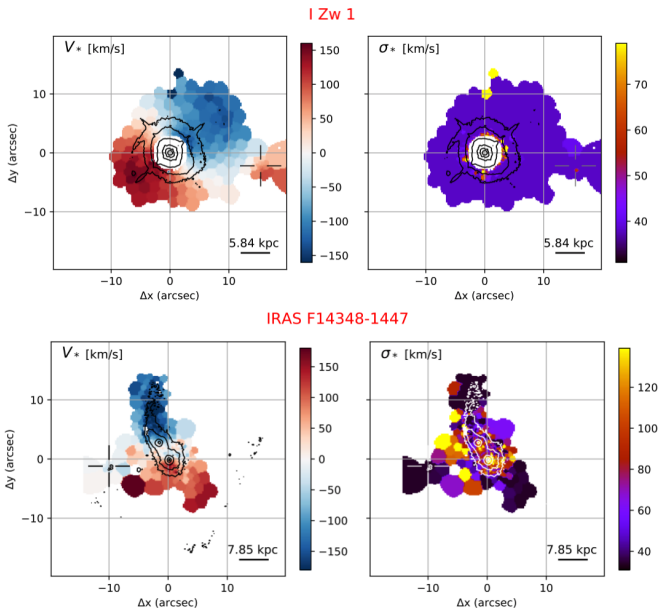

Fig. 3. pPXF stellar line-of-sight velocity (left) and velocity dispersion maps (right) for IZw1 (top) and F14348-1447 (bottom); σ_* are not corrected for instrumental broadening. Contours from HST/F160W images, starting from 3σ levels, equally spaced in steps of 0.5 dex. The IZw1 central pixels have been masked, because of the presence of strong continuum and BLR emission, which prevents the detection of stellar absorption features.

5.3. Stellar velocity versus Morphological classification

Table 3 summarizes the morphological and stellar kinematics information so far collected for our ULIRGs. They are based on the present MUSE colour and flux maps, HST/F160W imaging, and pPXF stellar kinematic results. For a more immediate visualization, we also report in Figs. 4 and 5 the MUSE Hα and stellar velocity maps already presented in Appendix C, within a simplified version of the α_{AGN}−IC diagram. These properties allow us to revise the morphological classification (with respect to the one used for the selection process in Sect. 2), and check consistency with the derived stellar kinematics.

According to Table 3, the observed 21 ULIRGs can be divided in four different groups, taking into account their IC and the presence of main stellar kinematic features. Namely, the first group contains eight sources characterised by ordered disk-like rotations and a merger classification, with a single nucleus and small nearby companions (F00188-0856, IZw1, F01572+0009, F05189-2524, 13120-5453, F14378-3651, 17208-0014 and 19542+1110). Almost all of them show additional detached (non-rotational) velocity structures in the outermost regions, possibly due to tidal tails.

The second group contains three systems, characterised by ordered disk-like motions and an interacting classification: 07251-0248, 10190+1322 and Arp220. 07251-0248 shows a disk-like rotation pattern with a kinematic centre close to the two nuclei, separated by 1.82 kpc, and a strong extended tidal tail. 10190+1322 shows two overlapping disks centered at the positions of the two nuclei, separated by $\sim$ 7 kpc. Finally, Arp220 show a disturbed kpc-scale disc in the innermost nuclear regions (see also Fig. 3 in Perna et al. 2020).

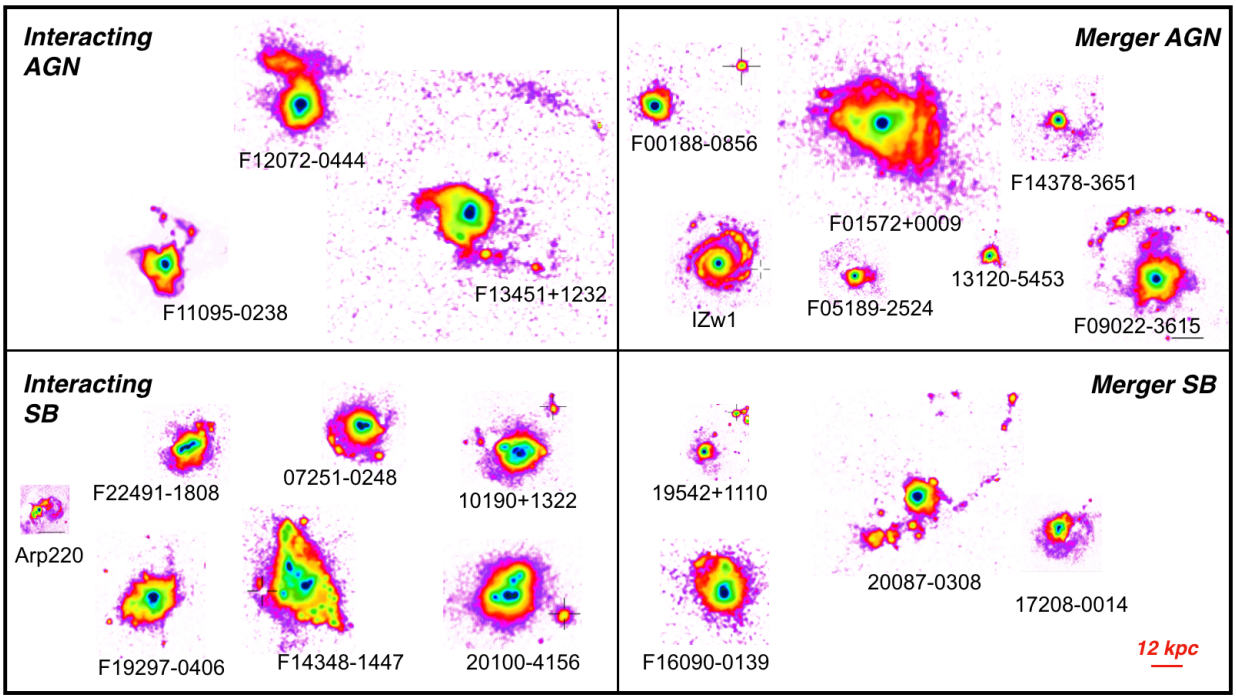

Fig. 4. MUSE Hα maps for all 21 ULIRGs of the PUMA sample. All maps are taken from the images shown in Appendix C. The galaxies are displayed in a simplified version of the $\alpha_{AGN}-$ IC plane shown in Fig. 1, with the same physical scale; North is up.

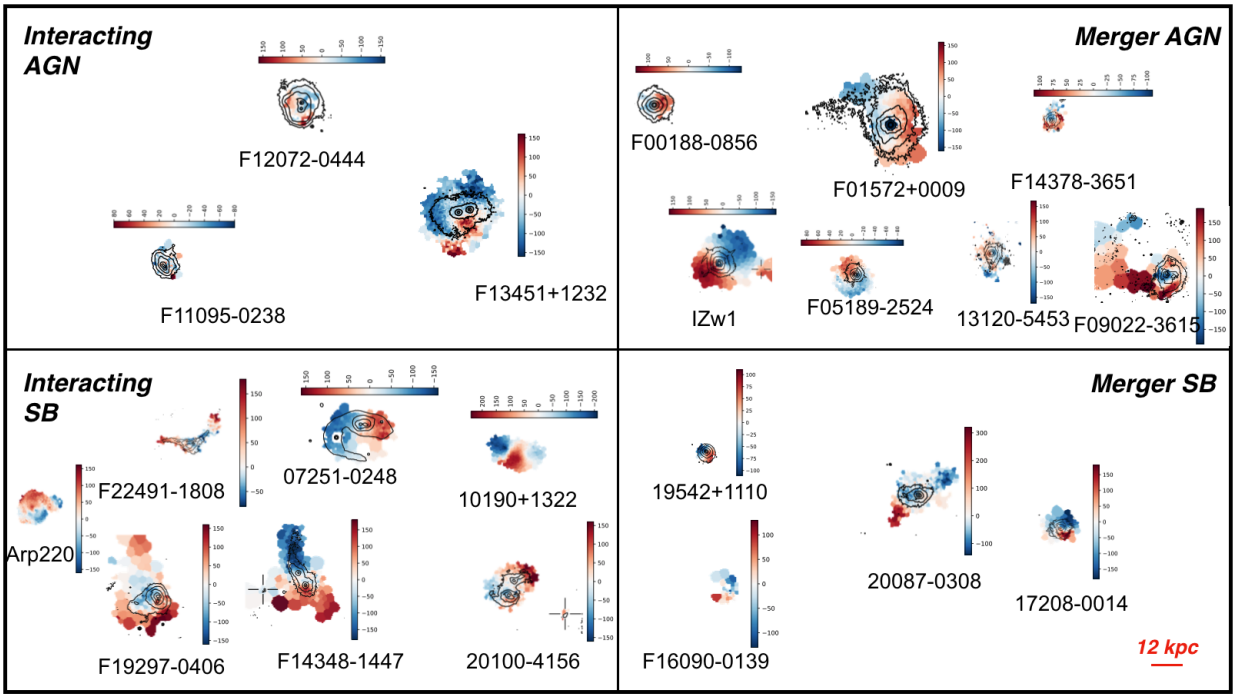

Fig. 5. MUSE stellar velocity maps for all 21 ULIRGs of the PUMA sample, taken from the images shown in Appendix C. The galaxies are displayed in a simplified version of the $\alpha_{AGN}-$ IC plane shown in Fig. 1, with the same physical scale; North is up.

The third group contains three ULIRGs, mainly characterised by large-scale streaming motions along the axes connecting their nuclei (F14348-1447 and F22491-1808), or along the strong and extended tails (20087-0308). F14348-1447 and F22491-1808 are interacting, while 20087-0308 is classified as a merger system.

Finally, the last group contains seven systems, mainly characterised by non-ordered stellar motions: 09022-3615, F11095-0238, F12072-0444, F13451+1232, F16090-0139, F19297-0406 and 20100-4156. Of them, two have a merger classification (09022-3615 and F16090-0139), while the remaining are interacting.

Two sources deserve a special mention: 09022-3615 and F19297-0406. HST/F814W and HST/F225W images of 09022-3615 show two main regions of intense SF in the central part of the system, with a few bright compact ($\lesssim 0.1''$, i.e. 150 pc) clumps at the position of the two peaks in the MUSE continuum image (Fig. C.22). These findings could suggest the presence of

Table 3. Morphological and kinematic classification

IRAS ID	overall stellar kinematics	main morphological features	N_{comp}	IC
(1)	(2)	(3)	(4)	(5)
F00188-0856	ordered motions	1 nucleus	1	M
IZw1	ordered motions	1 nucleus, spiral arms, [OIII] clumps at kpc-scales	1	M
F01572+0009	ordered motions	1 nucleus, tails, extended Hα	1	M
F05189-2524	ordered motions	1 nucleus, several tails, extended Hα	0	M
07251-0248	ordered motions	2 nuclei, ring-like shape, Hα clumps at kpc-scales	0	I
09022-3615	non-ordered motions	1 nucleus, tail, Hα clumps at kpc-scales	0	M
10190+1322	ordered motions	2 nuclei and overlapping disks, Hα clumps at kpc-scales	2	I
F11095-0238	non-ordered motions	2 nuclei, tails, extended Hα at kpc-scales	0	I
F12072-0444	non-ordered motions	2 nuclei, tails, diffuse Hα at kpc-scales	2	I
13120-5453	ordered motions	1 nucleus, extended structures and tails	0	M
F13451+1232	non-ordered motions	2 nuclei, tails, Hα clumps at kpc-scales	0	I
F14348-1447	large-scale streaming motions	2 nuclei, Hα clumps at kpc-scales	1	I
F14378-3651	ordered motions	1 nucleus, tails, and extended Hα shell	1	M
Arp220	ordered motions	2 nuclei, streaming motions, Hα shells	0	I
F16090-0139	non-ordered motions*	1 nucleus, plume, Hα bubble	0	M
17208−0014	ordered motions	1 nucleus, complex structures and kpc-scale tails	0	M
F19297-0406	non-ordered motions	1 nucleus, tails	0	I
19542+1110	ordered motions	1 nucleus, Hα clumps at kpc-scales	1	M
20087-0308	large-scale streaming motions	1 nucleus, tails, Hα clumps at kpc-scales	0	M
20100-4156	non-ordered motions	2 nuclei, tail	1	I
F22491-1808	large-scale streaming motions	2 nuclei, tails, diffuse Hα	0	I

Note.
Column (1): IRAS identification code.
Column (2): simplified classification for the stellar motions from the pPXF analysis.
Column (3): main morphological features.
Column (4): number of companions in the MUSE FOV; see Table A.1 for details.
Column (5): IC classification.

two SB regions, separated by ∼ 1.5 kpc and with a stellar velocity offset of ∼ 60 km/s. On the contrary, its nucleus, located at ∼ 0.5″ south from the southern SB based on ALMA data (Pereira-Santaella et al., in prep.), is extremely obscured and not associated with strong optical emission. F19297-0406 was originally classified as a merger (e.g. Kim et al. 2013); the inspection of near-IR HST (Fig. C.67) and ALMA (Pereira-Santaella et al., in prep.) allowed the identification of two nuclei, separated by ∼ 1.1 kpc. This source is therefore classified here as interacting (i.e. IIIb). For all remaining sources in our MUSE sample, instead, we confirm the morphological classification already reported in the literature.

The separation in the four sub-samples highlights that merging systems are more likely associated with ordered disk-like motions (8/11, i.e. F00188-0856, IZw1, F01572+0009, F05189-2524, 13120-5453, F14378-3651, 17208-0014, 19542+1110), while interacting systems are generally associated with non-ordered or streaming motions (7/10, i.e. F11095-0238, F12072-0444, F13451+1232, F14348-1447, F19297-0406, 20100-4156 and F22491-1808; see also e.g. Bellocchi et al. 2016 for similar results). Therefore, the morphological class (i.e. interacting/merger) is in general consistent with the stellar kinematic classification (i.e. dominant non-ordered/ ordered motions); we note however that even when rotation patterns are observed, tidal streams are also present, indicating that dynamical relaxation times depend on galactocentric distances: Indeed, kinematic disturbances from interactions are expected to fade within a few rotation cycles (e.g. Dale et al. 2001; Kronberger et al. 2007) and therefore, after the coalescence phase, the most external structures require longer times to follow the rotation pattern preserving irregular tidal induced velocities.

Indications of ordered motions in merger remnants were already reported in the literature: for instance, Barrera-Ballersteros et al. (2015) traced the stellar kinematics in CALIFA merging galaxies, and found that ∼ 90% of merger remnants exhibit disk-like motions (see their Figs. B.3 and B.4); moreover, K-band observations reported by Rothberg & Joseph (2004) revealed that most of the mergers in their sample show disky isophotals. Numerical simulations suggest that the amount of stellar disks that survives or re-forms after an interaction is a strong function of the stellar mass ratio and gas content of the interacting galaxies: For instance, gas-rich mergers can yield disk-dominated remnants, while for modest gas fractions the remnants are likely to resemble spheroidal-like galaxies (e.g. Hopkins et al. 2009a,b; Naab & Ostriker 2017).

We finally note that the Hα flux and stellar velocity maps in the simplified α_{AGN}−IC diagram (Fig 4) do not show clear trends, but are overall consistent with the Sanders et al. (1988) evolutionary scenario. In particular, more compact and dynamically relaxed systems are more likely to be found in the merger-AGN class, while interacting galaxies more likely present extended structures with several extra nuclear clumps and knots of SF.

6. ISM nuclear properties: Outflows and ionization conditions

In this section, we report the general ISM properties of the ULIRG nuclear regions obtained analysing MUSE data. In particular, we revise the optical classification of the nuclear spectra, and infer the possible presence of atomic outflows, taking advantage of the unprecedented quality of MUSE data. This information is required to understand if the PUMA sample, selected to characterise multi-phase outflows, actually host gas flows potentially due to SB and AGN winds.

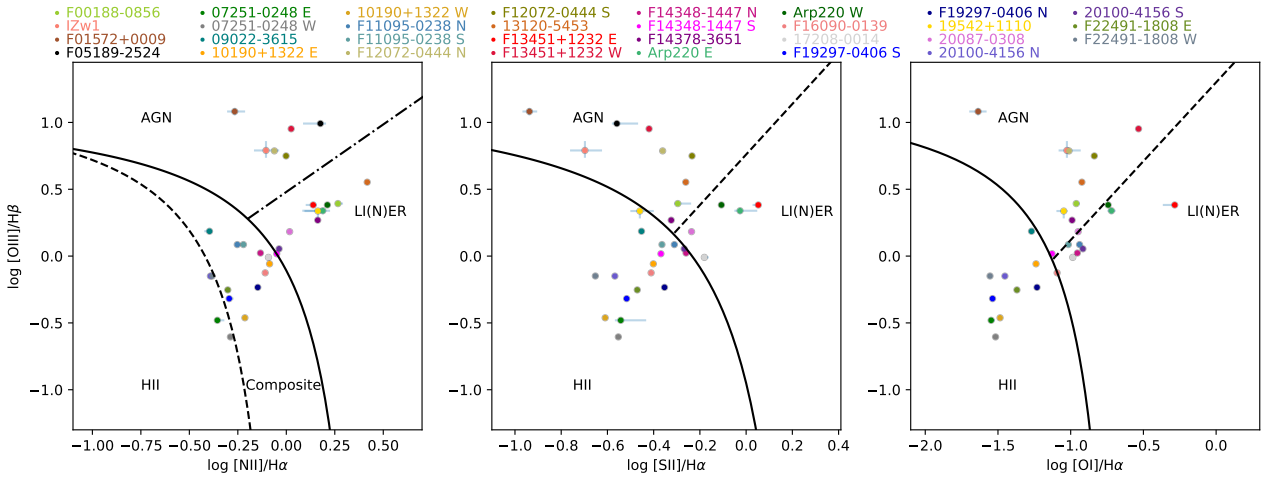

Fig. 6. Standard diagnostic BPT diagrams showing our flux ratio measurements obtained from the ULIRG nuclear spectra. Each nucleus is identified with a distinct color, as labeled. Black curves separate HII-, composite-, AGN- and LI(N)ER-like line ratios, as labeled in the three panels (see text for details).

Thirty-one nuclear spectra are extracted from circular apertures centred at the position of the ULIRGs nuclei, with $r < 0.4''$ (i.e. considering our average spatial resolution). As a first step, we used pPXF to model the stellar contribution (Sect. 5) and, after subtracting it, we used our own suite of python scripts to fit simultaneously all ISM prominent features. In particular, we modelled all emission lines with a combination of Gaussian profiles, to account for the presence of both narrow and BLR features in type 1 AGN or, more in general, of asymmetric profiles with broad wings, possibly tracing perturbed kinematics and outflows. NaID absorption is instead fitted with a model parameterised in the optical depth space, as already described in Perna et al. (2020). In the next section, we describe the modelling prescription for the ISM features of all but IZw1 and F01572 nuclei, the two Sy 1 nuclei, whose prescription is presented in Appendix B.

6.1. ISM features modelling

We modelled with Gaussian profiles the Hβ and Hα lines, the HeIλ5876, the [O III]$\lambda\lambda$4959,5007, [N II]$\lambda\lambda$6548,83, [S II]$\lambda\lambda$6716,31 and [O I]$\lambda\lambda$6300, 64 doublets. We constrained the wavelength separation between emission lines in accordance with atomic physics; moreover, we fixed the FWHM to be the same for all the emission lines. Finally, the relative flux of the two [N II] and [O III] components was fixed to 2.99, the relative flux of the two [O I] lines was fixed to 3.13, and the [S II] flux ratio was required to be within the range $0.44 < f(\lambda6716)/f(\lambda6731) < 1.42$ (Osterbrock & Ferland 2006).

To account for potential asymmetric line profiles, we performed each spectral fit four times at maximum, with one to four kinematic components (i.e. Gaussian sets, each centred at a given velocity and with a given FWHM). The final number of kinematic components used to model the spectra was derived on the basis of the Bayesian information criterion (BIC, Schwarz 1978; see e.g. Perna et al. 2019).

We simultaneously modelled the contribution of NaID resonant lines. When sodium emission is detected, Gaussian profiles are used, requiring a Na ID doublet line ratio between the optically thick ($f(H)/f(K) = 1$) and thin ($f(H)/f(K) = 2$) limits (e.g. Rupke & Veilleux 2015), where H and K indicate the sodium transitions at 5891 and 5896 Å. The NaID absorption contribution is instead fitted with a model parameterised in the optical depth space, following Sato et al. (2009):

$$I(\lambda) = I_{em}(\lambda) \times f_{ABS}(\lambda)$$
$$= I_{em}(\lambda) \times (1 - C_f \times [1 - exp(-\tau_0 e^{-(\lambda-\lambda_K)^2/(\lambda_K b/c)^2} - 2\tau_0 e^{-(\lambda-\lambda_H)^2/(\lambda_H b/c)^2})]), \quad (1)$$

where H and K indicate the two sodium transitions, C_f is the covering factor, τ_0 is the optical depth at the line centre λ_K, b is the Doppler parameter ($b = FWHM/[2\sqrt{ln(2)}]$) and c is the light velocity. The term $I_{em}(\lambda)$ in Eq. 1 represents the intrinsic (unabsorbed) intensity, defined as $I_* + I_{HeI}$, where I_* is the best-fit model obtained from pPXF analysis and I_{HeI} is the helium line intensity (Baron et al. 2020). When more than one kinematic component is required to fit NaID absorption features, we assumed the case of partially overlapping atoms on the line of sight (LOS), so that the total sodium profile can be reproduced by multiple components and $I(\lambda) = I_{em}(\lambda) \times \Pi_{i=1}^{n} f_{ABS}^{i}(\lambda)$, where $f_{ABS}^{i}(\lambda)$ is the i-th component (as given in Eq. 1) used to model the sodium features (see also Sect. 3.1 in Rupke et al. 2002). We stress here that the kinematics of a given Na ID component (either in absorption or emission) are tied to those of a corresponding Gaussian set used to model the ISM emission lines.

Best-fit models for individual nuclear regions in our ULIRGs sample are reported in Appendix C. These fit results are used to investigate the dominant ionisation mechanism(s) for the emitting gas, and to derive the incidence of neutral and ionised outflows.

6.2. BPT diagnostics

Figure 6 shows the BPT diagrams with the results from our spectroscopic analysis. All line ratios are derived by integrating the line flux over the entire fitted profiles (i.e. considering all kinematic components used to model the lines). For simplicity, hereinafter the [O III]λ5007/Hβ versus [N II]λ6583/Hα (left panel), the [O III]λ5007/Hβ versus [S II]$\lambda\lambda$6716,31/Hα (centre) and [O III]λ5007/Hβ versus [O II]λ6300/Hα (right) will be labeled as [NII]-, [SII]- and [OI]-BPT diagrams, respectively. In the figure, each coloured dot identify a unique nuclear spectrum, as labeled in the top.

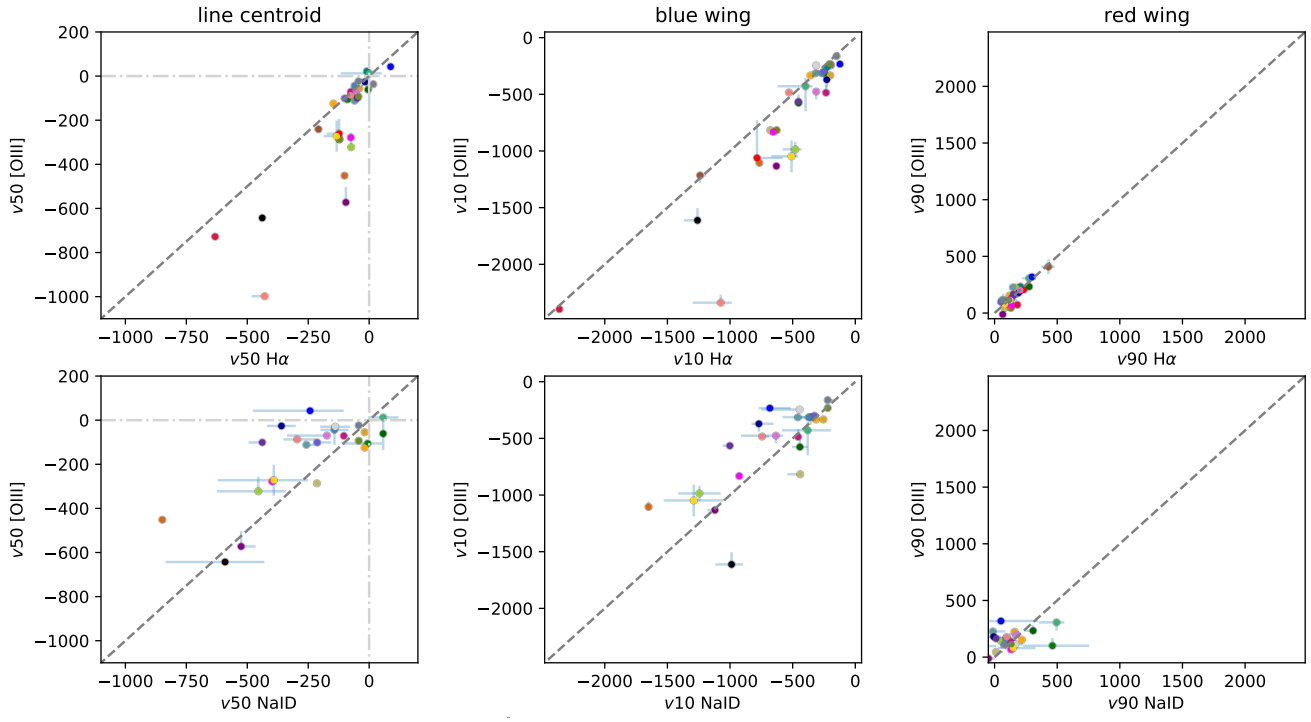

Fig. 7. Velocity-velocity diagram (VVD) used to compare the non-parametric velocities of [OIII], Hα and NaID gas, for the 31 nuclei reported in Table 4. Each nucleus is identified with a distinct colour (see labels in Fig. 6). In the *left column*, we show the central velocities of [OIII] versus Hα (top), and of [OIII] versus NaID (bottom); horizontal and vertical dot-dashed lines mark the zero-velocity positions, while the dashed line display the 1:1 relation. In the *central column*, we show the $v10$ velocities, associated with the blue wings of [OIII] and Hα (top), and of [OIII] and NaID (bottom); the dashed line indicates the 1:1 relation. In the *right column*, we show the $v90$ velocities, associated with the red wings of [OIII] and Hα (top), and of [OIII] and NaID (bottom); the dashed line indicates the 1:1 relation.

The curves drawn in the [NII]-BPT diagram correspond to theoretical boundary for extreme SBs (Kewley et al. 2001) and the empirical relation (Kauffman et al. 2003) used to separate purely SF galaxies from composite AGN-SF galaxies and AGN-/LI(N)ER-dominated systems (e.g. Kewley et al. 2006; Belfiore et al. 2016); the dot-dashed line is from Cid Fernandes et al. (2010), and is used to separate LI(N)ERs and AGN. The curves in the [SII]- and [OI]-BPT diagrams correspond to the optical classification scheme of Kewley et al. (2006, 2013), and are used also in this case to separate SF galaxies from AGN and LI(N)ER systems, as labeled in the figures.

For the sources for which at least two BPT diagnostics indicate the same region, we constrain the dominant ionisation mechanism responsible of the lines emission: 11/31 nuclei are associated with SF, 9/31 with AGN and 6/31 with LI(N)ER ionisation. For the remaining 5 spectra, the BPT diagnostics provide inconsistent results, i.e. the three diagnostics indicate three different ionisation mechanisms.

Our flux ratio measurements are distributed over all the different regions of the BPT diagrams, and the inferred classification is overall consistent with that reported in the literature (Table 1), although the latter were obtained from long-slit (spatially integrated) spectra. Our optical classification is also generally consistent with the α_{AGN} values reported in Table 1. The only exception, in this case, might be represented by 09022-3615, for which we observe SF-like line ratios, although the $\alpha_{AGN} = 0.54$ derived with mid-IR diagnostics; our results are instead consistent with the small (near-IR based) AGN fraction inferred by Nardini et al. (2010, see Table 1). These findings could suggest the presence of an extremely obscured AGN in this system (see also Sect. 5.3). We also note that 11/17 nuclei with $\alpha_{AGN} < 0.32$ have LI(N)ER-like ratios, possibly indicating the presence of shocks induced by SB-driven outflows or gravitational interactions[3].

6.3. Multi-phase outflow incidence

Almost all nuclear spectra show asymmetric and broad line profiles, possibly indicating strongly perturbed gas kinematics in both neutral (NaID) and ionised (e.g. [OIII], Hα) atomic components. To characterise the overall kinematic properties of the ISM gas in a homogeneous way (i.e. to avoid any dependence on the number of distinct kinematic components used to model the line features in individual spectra), we used the non-parametric velocities $v10$, $v50$ and $v90$, defined as the 10th-, 50th- and 90th-percentile velocities of the fitted line profiles, respectively, and the linewidth $w80$, i.e. the difference between the 85th- and 15th-percentile velocities (see e.g. Harrison et al. 2014). All velocities are derived with respect to the systemic velocity, as inferred from the stellar velocities measured from pPXF (see Sec. 5). [OIII] and Hα line features are used as tracers for the ionised gas kinematics; instead, ISM neutral atomic gas kinematics are traced by the NaID absorption component, detected in almost all nuclear spectra and showing the broadest profiles if compared with the NaID emission component (detected only in a few targets).

Figure 7 (first column) shows the velocity-velocity diagrams (VVD) comparing the central velocities ($v50$) of [OIII] and Hα,

[3] In many local galaxies, the LI(N)ER emission is associated with gas ionised by the hard radiation field of evolved (post-AGB) stars, with Hα equivalent widths < 3, as discussed e.g. by Belfiore et al. (2016). However, this does not apply to our ULIRGs nuclear regions.

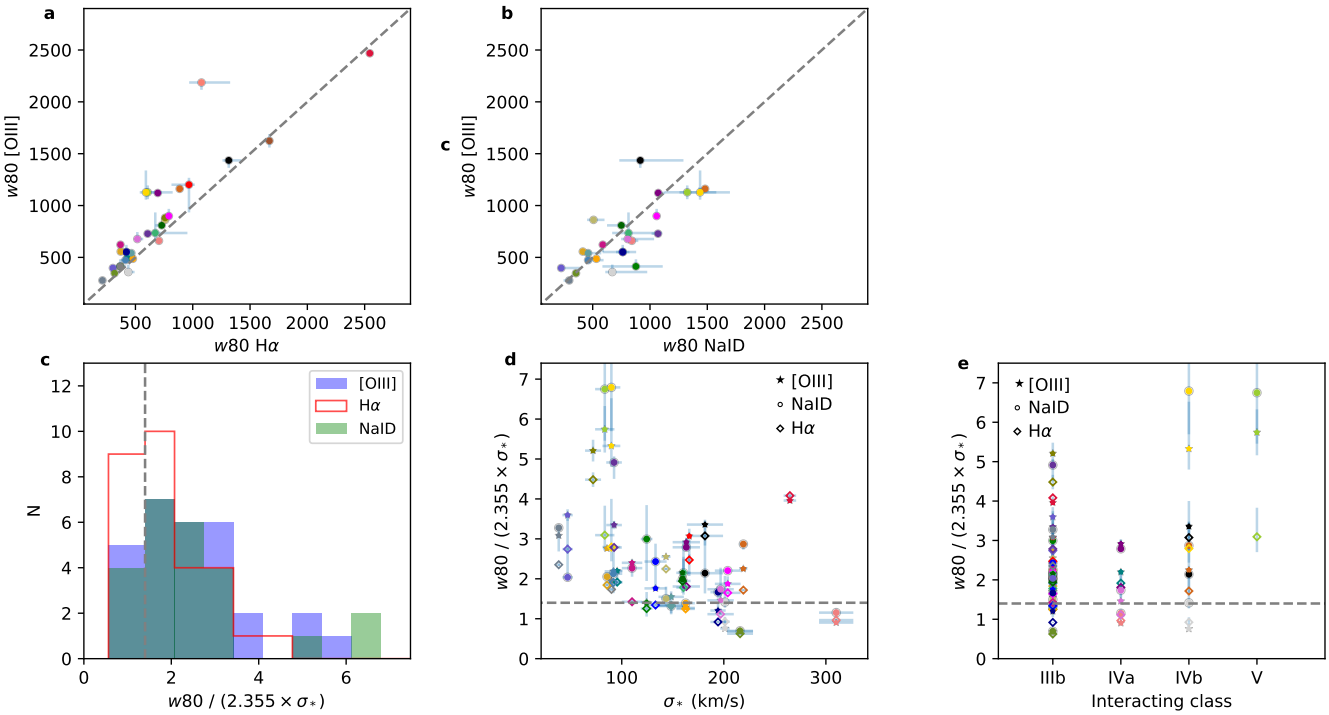

Fig. 8. *Panels a and b*: $w80$ velocity-velocity diagram (VVD) for [OIII] versus Hα (*a*), and [OIII] versus NaID (*b*). Each nucleus is identified with a distinct (see labels in Fig. 6). Dashed lines display the 1:1 relation. *Panel c*: Distributions of $\eta = w80/(2.355 \times \sigma_*)$ for the three kinematic tracers, as labeled in the legend; the dashed vertical line marks the position $\eta = 1.4$ (see text). *Panel d*: [OIII] (star symbols), Hα (diamonds) and NaID (circles) η measurements as a function of σ_*. All velocity dispersion and $w80$ measurements are not corrected for instrumental broadening; this would affect the only two σ_* measurements close to the MUSE spectral resolution ($\approx$ 50 km/s), associated with the 20100-4156 N and F22491-1808 W nuclei, further increasing their η values. *Panel e*: **[OIII] (star symbols), Hα (diamonds) and NaID (circles) η measurements as a function of the IC.**

in the top panel, and of [OIII] and NaID, in the bottom panel. Almost all line centroids are blueshifted with respect to the systemic, indicating the presence of significant contribution from approaching emitting ([OIII] and Hα) and absorbing (NaID) material. This is confirmed by the fact that, generally, the line profiles show very prominent blue wings, and faint and less extended red wings, as also shown in the central and right columns of Fig. 7, presenting $v10$ and $v90$ VVD respectively.

In general, [OIII] shows more extreme velocities, when compared to those of Hα (see also e.g. Bae & Woo al. 2014, Venturi et al. 2018, and Cicone et al. 2016 for similar results). The NaID velocities, in turn, appear slightly higher than those of the [OIII], although the former are associated with higher uncertainties (due to the fit degeneracy[4]): $\langle v10$ [OIII] / $v10$ Hα $\rangle$ = 1.27 and $\langle v10$ NaID / $v10$ [OIII] $\rangle$ = 1.16.

In Fig. 8 (panels *a* and *b*) we show the $w80$ VVD. Also in this case, we observe that, in general, NaID $w80$ are slightly higher than [OIII] $w80$, which, in turn, are higher than Hα linewidths: $\langle w80$ [OIII] / $w80$ Hα $\rangle$ = 1.15 and $\langle w80$ NaID / $w80$ [OIII]$\rangle$ = 1.10. In order to discriminate between gravitational and outflow processes possibly responsible of the velocity shifts and the extreme $v10$ and $w80$ in the [OIII], Hα and NaID lines, we compare their linewidths with the stellar velocity dispersion at the position of the nuclei. Following Woo et al. (2016), we assume that a non-gravitational component dominates over the gravitational one when $\eta = w80/(2.355 \times \sigma_*) > 1.4$, with the stellar velocity dispersion σ_* tracing the gravitational motions. This is a conservative criterion, as originally proposed for type 2 AGN and applied here to ULIRG nuclear spectra: In fact, σ_* may be enhanced by motions associated to the merging process in ULIRGs.

In Fig. 8, panel *c*, we report the histograms of the η measurements, as obtained for the three kinematic tracers; in panel *d*, instead, we show σ_* as a function of η, for Hα, [OIII] and NaID features. From the latter two tracers, we derived $\eta < 1.4$ for only three nuclei: 10190+1322 E, F16090-0139 and F22491-1808 E. The Hα distribution shows instead nine nuclei with $\eta < 1.4$, again indicating that the Balmer line can be less affected by non-gravitational motions. For each tracer and nucleus, we indicate in Table 4 the dominance of gravitational or non-gravitational motions, according to the chosen criterion.

We note that the η criterion can be applied for all nuclei for which *(i)* σ_* can be derived from pPXF analysis, and *(ii)* the specific kinematic tracer for ionised and neutral gas is detected. [OIII] and Hα lines are detected in all spectra, but no stellar features are present in the IZw1 and F01572+0009 nuclear spectra; therefore, ionised gas η measurements are derived for all but these two Sy 1 nuclei. On the contrary, NaID absorption is not detected in 7/31 nuclear spectra: the two Sy 1 targets, IZw1 and F01572+0009, show strong continuum and very broad line emission from the HeI at the position of the two NaID transitions; moreover, although NaID emission is detected, the strong BLR component prevents a robust analysis of a possible neutral outflow traced by the NaID emission. The F13451+1332 W spectrum does not show sodium absorption (Fig. C.49), although a faint (C_f = 0.11) and broad (b = 400 km/s) NaID

[4] The higher uncertainties in NaID velocities are due to the fit degeneracy. In particular, they could originate from a blending between the HeI (in emission) and the NaID features, when strong sodium absorption is detected at very high negative velocities (e.g. F05189-2524, F14378-3651). Alternatively, it can originate from the modelling of NaID P Cygni profiles (F05189-2524, F11095-0238 NE).

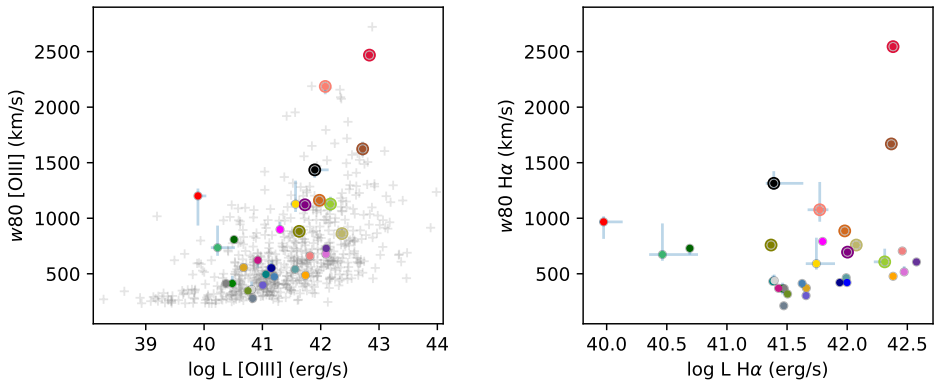

Fig. 9. *Left*: [OIII] non-parametric velocity $w80$ as a function of $L_{[OIII]}$, for the ULIRGs nuclei presented in this work (colour-coded as in Fig. 6), and the X-ray/SDSS AGN (grey crosses) from Perna et al. (2017a). Larger symbols identify the ULIRG nuclei with AGN ionisation (see Table 4). *Right*: Hα non-parametric velocity $w80$ as a function of $L_{H\alpha}$, for the ULIRG nuclei presented in this work.

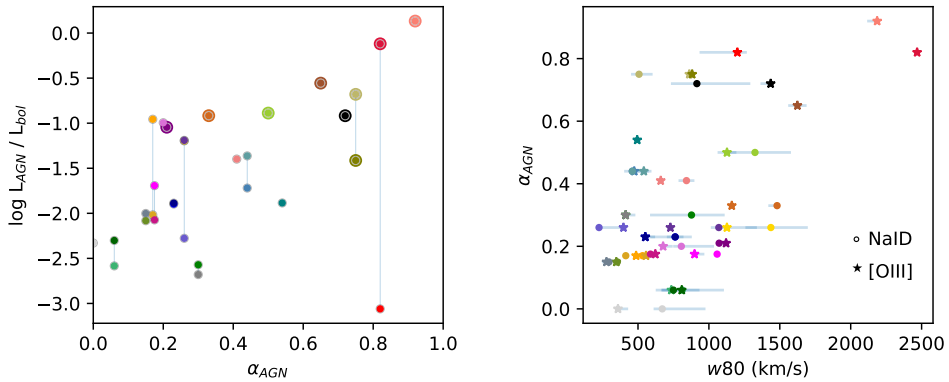

Fig. 10. *Left*: (mid-IR based) AGN fraction α_{AGN} as a function of the ratio L_{AGN}/L_{bol}, with $L_{AGN} = 3 \times 10^3\ L_{[OIII]}$ and $L_{bol} = 1.15\times\ L_{IR}$. The nuclei of binary systems are connected with a vertical line; larger symbols refer to the sources with dominant AGN ionisation, according to our BPT diagnostics. *Right*: [OIII] and NaID non-parametric velocity $w80$ as a function of the AGN fraction α_{AGN}, defined on the basis of mid-IR diagnostics (Sect. 1). Each nucleus is identified with a distinct colour, as in Fig. 6.

profile in absorption has been reported in Rupke et al. (2005c); the NaID emission component, used in our analysis to model the observed spectrum might not be as reliable as pPXF best-fit results are not robust (no strong stellar absorbing features are detected over the entire wavelength range covered with MUSE). Finally, for the remaining four spectra (07251-0248 W, F12072-0444 S, F13451+1232 E, and 09022-3615), the stellar NaID contribution is responsible for the total absorption, according to our pPXF analysis results. As a consequence, we can infer the presence/absence of dominant non-gravitational motions in absorbing neutral gas for 24 nuclei.

Among the sources with $\eta < 1.4$ from both [OIII] and NaID kinematics (i.e. 10190+1322 E, F16090-0139 and F22491-1808 E), we note that in at least one sources, F16090-0139, the stellar velocity dispersion might be overestimated (because of the low S/N), while the ISM features are extremely broad (e.g. NaID $w80 \approx 840$ km/s; see Fig. C.62). Indeed, this nucleus presents the highest σ_* among our sample (see Fig. 8, panel *d*). Hence, the F16090-0139 nucleus is reasonably associated with an outflow. We also note that the two Sy 1 nuclei display extremely broad features, likely associated with outflows. Taking into account these arguments, we conclude that non-gravitational motions dominate the neutral (ionised) gas kinematics in 20/24 (28/31) nuclei.

Finally, Fig. 8, panel *e*, shows the η measurements as a function of the IC of each target. No clear trend is observed for the three gas kinematic tracers (i.e. NaID, Hα and [OIII], with Spearman's coefficients of ≈ 0.1). Despite the poor statistics, this finding suggests that nuclear winds are ubiquitous during the pre- and post-coalescence phases of major mergers.

The presence of a dominant non-gravitational component in almost all ULIRGs nuclei, together with the prevalent prominent blue wings in [OIII] and NaID, with $v10$ of several 100s km/s, indicate the presence of strong multi-phase outflows driven by either AGN or SB nuclear activity.

6.4. AGN- and SB-driven outflows

In Sect. 5.3, we reported a good consistency between the morphological and stellar kinematic classifications, with merging systems more likely associated with ordered disk-like motions (in 8/11 of our ULIRGs) and interacting systems with non-ordered or streaming motions (in 7/10 ULIRGs). The ubiquitous presence of atomic outflows (Sect. 6.3) suggests that nuclear winds are not related to a specific phase, or to more/less dynamically-relaxed systems, but are actually common in all final stages of the merger process (as already reported in the literature; see e.g. Sect. 10.5 in Perna et al. 2020). In this section, we therefore investigate the possible connection between AGN/SB activity and the atomic outflow velocities.

Figure 9 (left) shows the distribution of the [OIII] $w80$ measurements against the [OIII] luminosity. In the same figure (right), we also report the Hα $w80$ versus $L_{H\alpha}$. Both [OIII]

Table 4. ISM nuclear properties

IRAS ID (other)	optical class	BPTs	dominant motions from η criterion			max $w80$ (km/s)
			Hα	[OIII]	NaID	
(1)	(2)	(3)	(4)	(5)	(6)	(7)
F00188−0856	AGN	(L,A,A)	non-grav	non-grav	non-grav	1325^{+255}_{-195} (NaID)
IZw1	AGN	(A,A,A)	-	-	-	2190^{+10}_{-70} ([OIII])
F01572+0009	AGN	(A,A,A)	-	-	-	1670^{+10}_{-60} ([OIII])
F05189−2524	AGN	(A,A,A)	non-grav	non-grav	non-grav	1860^{+130}_{-10} ([OIII])
07251−0248 E	SB	(S,S,S)	grav	non-grav	non-grav	880^{+230}_{-200} (NaID)
07251−0248 W	SB	(S,S,S)	non-grav	non-grav	-	410 ± 5 ([OIII])
09022−3615	SB	(C,S,S)	non-grav	non-grav	-	495 ± 5 ([OIII])
10190+1322 E	SB	(C,S,S)	grav	grav	grav	530^{+5}_{-20} (NaID)
10190+1322 W	SB	(C,S,S)	non-grav	non-grav	non-grav	555^{+5}_{-5} ([OIII])
F11095−0238 NE	?	(C,S,L)	non-grav	non-grav	non-grav	610^{+10}_{-70} ([OIII])
F11095−0238 SW	?	(C,S,L)	grav	non-grav	grav	540 ± 5 ([OIII])
F12072−0444 N	AGN	(A,A,A)	non-grav	non-grav	non-grav	860 ± 5 ([OIII])
F12072−0444 S	AGN	(A,A,A)	non-grav	non-grav	-	880 ± 5 ([OIII])
13120−5453	AGN	(L,A,A)	non-grav	non-grav	non-grav	1480^{+5}_{-60} (NaID)
F13451+1232 E	LI(N)ER	(L,L,L)	non-grav	non-grav	-	1200^{+70}_{-270} ([OIII])
F13451+1232 W (4C 12.50)	AGN	(A,A,A)	non-grav	non-grav	-	2545 ± 5 (Hα)
F14348−1447 NE	?	(C,S,L)	non-grav	non-grav	non-grav	620^{+10}_{-70} ([OIII])
F14348−1447 SW	?	(L,S,A)	non-grav	non-grav	non-grav	1060 ± 5 (NaID)
F14378−3651	AGN	(L,A,A)	non-grav	non-grav	non-grav	1120 ± 5 ([OIII])
Arp220 E	LI(N)ER	(L,L,L)	non-grav	non-grav	non-grav	810^{+300}_{-140} (NaID)
Arp220 W	LI(N)ER	(L,L,L)	non-grav	non-grav	non-grav	810 ± 5 ([OIII])
F16090−0139	SB	(C,S,S)	grav*	grav*	grav*	840^{+60}_{-55} (NaID)
17208−0014	LI(N)ER	(C,L,L)	grav	grav	non-grav	435^{+55}_{-5} (NaID)
F19297−0406 S	SB	(C,S,S)	grav	non-grav	non-grav	760^{+110}_{-180} (NaID)
F19297−0406 N	SB	(C,S,S)	grav	grav	non-grav	630^{+10}_{-55} (NaID)
19542+1110	?	(L,S,A)	non-grav	non-grav	non-grav	1440^{+260}_{-180} (NaID)
20087−0308	LI(N)ER	(L,L,L)	grav	non-grav	non-grav	800^{+230}_{-50} (NaID)
20100−4156 N	SB	(S,S,S)	non-grav	non-grav	non-grav	400 ± 5 ([OIII])
20100−4156 S	LI(N)ER	(L,S,L)	non-grav	non-grav	non-grav	560^{+400}_{-380} (NaID)
F22491−1808 E	SB	(C,S,S)	grav	grav	grav	355 ± 5 (NaiD)
F22491−1808 W	SB	(S,S,S)	non-grav	non-grav	non-grav	295^{+10}_{-50} (NaID)

Notes.
Column (1): IRAS identification code (alternative name).
Column (2): optical classification obtained from the three BPT diagrams shown in Fig. 6. The classification is defined only in case two or three diagnostic diagrams indicate the same ionisation mechanism; if the three diagnostics indicate three different mechanisms, then a '?' is placed in this column.
Column (3): ionisation class from the [NII]-, [SII]- and [OI]-BPT diagostics, respectively (S: HII, C: composite, A: AGN, L: LI(N)ER line ratios).
Columns (4-6): dominant motions from $\eta = w80/(2.355 \times \sigma_*)$, considering the Hα, [OIII] and NaID linewidths; see Sect. 6.4 for details.
Column (7): maximum $w80$ measured among the Hα and [OIII] emission lines as well as the NaID absorption features.
*: the stellar velocity dispersion in the F16090 nucleus is probably overestimated (σ_* = 310 km/s), because of the low S/N.

and Hα luminosities have been corrected for extinction, considering the measured Balmer decrement and a Cardelli et al. (1989) extinction law. The [OIII] measurements show a positive trend with increasing luminosity (with a Spearman's coefficient of 0.6), while the Hα do not show any significant correlation; we also note that our ULIRGs cover similar region in the [OIII] diagram as the X-ray/SDSS AGNs analysed in Perna et al. (2017a), reported in our figure with grey '+' symbols. This could suggest that *(i)* the AGN activity, traced by $L_{[OIII]}$, is responsible for the outflows in the ULIRG nuclei, or that *(ii)* AGN and SB-driven winds are hardly distinguishable in this diagram.

To test these two scenarios, we studied the correlation between two different estimates for the AGN fraction: (i) α_{AGN}, the AGN contribution to the L_{bol} according to mid-IR fluxes (Sect. 1), and (ii) L_{AGN}/L_{bol}, the ratio between the [OIII]-based AGN luminosity (inferred assuming a bolometric correction of 3×10^3; Heckman et al. 2004), and the bolometric luminosity L_{bol}, given by $1.15 \times L_{IR}$ (Veilleux et al. 2009). A positive correlation between these quantities is expected in the case [OIII] traces the AGN power. In Fig. 10 (left), we report α_{AGN} as a function of L_{AGN}/L_{bol}. A significant correlation (with a Spearman's coefficient of 0.6) is found, once we exclude the most deviating measurement, namely the red dot associated with F13451+1232 E (whose AGN fraction is reasonably overestimated; see below). Therefore, this finding is in principle consistent with the hypothesis that the AGN activity is responsible of the outflows we observe in almost all ULIRG nuclei.

However, there are a number of caveats concerning the relation in Fig. 10, left. Both L_{bol} and α_{AGN} are based on spatially integrated IR emission measurements, and refer to the entire ULIRG systems. We can reasonably assume that most of such IR emission is coming from the nuclei (e.g. Lutz et al. 1999, Pereira-Santaella et al., in prep.), and that all quantities in the figure are related to the same spatial regions, at least for the targets with a single nucleus. For the binary systems, we used the same L_{IR} and α_{AGN} for both nuclei (these systems are con-

nected with vertical lines in the figure). This is a reasonable assumption, as the [OIII] luminosities associated with the two nuclei of individual systems are comparable, within a factor of a few. The only exception is represented by F13451+1232, with $L_{[OIII]} = 6.8 \times 10^{42}$ erg/s (W) and 7.8×10^{39} erg/s (E). The western nucleus, associated with AGN activity (Fig. 6), harbors the powerful radio source 4C 12.50 (Lister et al. 2003), and might be responsible of the majority of IR emission. If so, the only deviating point in Fig. 10 (left), associated with F13451+1232 E, should have a much smaller α_{AGN}. However, a detailed investigation is required to confirm all assumptions so far mentioned. Moreover, BPT diagnostics revealed that AGN dominates over SB and LI(N)ER ionisation mechanisms only in 9 nuclei (large symbols in Fig. 10, left); in the remaining nuclei, therefore, the [OIII] luminosity is not a good tracer for the AGN power. All these arguments weaken the significance of the trend reported in Fig. 10, left.

We also considered the correlation between the NaID and [OIII] linewidths and α_{AGN}, as broader line profiles are generally reported in the literature for AGN-driven outflows (e.g. Cazzoli et al. 2016; Kakkad et al. 2020). These measurements are reported in Fig. 10, right, and do not show a clear trend (Spearman's correlation: 0.4). We therefore conclude that, although a significant contribution of [OIII] might be due to AGN, a combination of SB- and AGN-driven winds might be responsible of the observed atomic outflows. More detailed analysis about the outflow nature will be however presented in future papers, together with detailed spatially resolved properties of neutral and ionised outflows (e.g. Perna et al. 2020).

We finally note that most of the nuclei with neutral outflows have relatively low AGN fractions; instead, at $\alpha_{AGN} > 0.5$, NaID outflows are present in only one nucleus, F05189-2524 (out of 8, see Fig. 10, right), confirming the difficulties in observing neutral outflows in systems with strong AGN (e.g. Perna et al. 2017a; Bae & Woo 2018; Nedelchev et al. 2019). A detailed spatially resolved analysis will be however required to exclude the presence of neutral outflows in the more external regions of these powerful AGN (e.g. Rupke et al. 2017; Perna et al., in prep.).

7. Conclusions

The "Physics of ULIRGs with MUSE and ALMA" (PUMA) project is a survey of 25 nearby ULIRGs observed with MUSE and ALMA. This is a representative sample covering the entire ULIRG luminosity range, and including a combination of systems with AGN and SB nuclear activity in (advanced) interacting and merging stages. This project represents the first such study intended to characterize the multi-phase structure of the ISM in local ULIRGs at sub-kpc resolutions. This paper is the first in a series which will explore the prevalence of ionised, neutral and molecular outflows as a function of the galaxy and BH properties, and the nature and the (feedback) effects of such outflows on the galaxy evolution.

In this work, we presented the first data products obtained analysing the MUSE data of the 21 ULIRGs so far observed. We described the stellar kinematics derived with pPXF analysis, and the properties of stellar and ionised gas emission. Our first results can be summarised as follows.

- Colour composites, ionised gas and stellar continuum emission images show a great richness in spatial details at different spatial scales. These images reveal the presence of recent galaxy interactions and strong (dust enshrouded) nuclear activity, in line with their ULIRG nature (see e.g. Fig. 2).
- Stellar kinematics revealed that merging systems are more likely associated with ordered disk-like motions (8/11), while binary (interacting) systems are dominated by non-ordered and streaming motions (7/10; see e.g. Fig. 5);
- The sources with stellar rotational patterns are more likely found in compact mergers hosting AGN (6/11); on the other hand, more extended structures with non-ordered motions are found in interacting systems, showing several extra nuclear SF clumps and strong tidal tails (Figs. 4 and 5);
- All ULIRGs show distinct velocity structures detached from the the inner pattern, due to the presence of tidal tails. This also applies to the post-coalescence mergers with clear inner rotational patterns, and confirms that the external structures require longer times to reach a dynamically relaxed configuration.

In the second part of the paper, we analysed the 31 nuclear spectra extracted from the positions of the ULIRG nuclei, deriving the physical and kinematic properties of the nuclear ISM. Our first results can be summarised as follows.

- We used BPT diagnostics to constrain the dominant ionisation mechanism responsible of the optical emission lines: 11/31 nuclei are associated with SF, 9/31 with AGN and 6/31 with LI(N)ER ionisation. Overall, the inferred classification is consistent with that reported in the literature (Table 1), although the latter were obtained with long-slit spectra. Our classification is also consistent with the archival α_{AGN} estimates, obtained from mid-IR diagnostics. For the remaining 5 nuclei, the three BPT diagnostics indicated three different ionisation mechanisms, possibly indicating a more complex mixture between SB, AGN and shocks-induced ionisation due to the presence of nuclear winds (see Table 4).
- Almost all nuclear spectra show asymmetric and broad line profiles in both neutral (NaID) and ionised (e.g. [OIII]) transitions. Nuclear ISM features display velocity dispersions > 0.15 dex higher than σ_* in $\sim$ 85% of the nuclear spectra. Following Woo et al. (2016), we considered these enhancements with respect to σ_* as an indication of the presence of strong non-gravitational motions in the ISM component. This, together with the extreme $v10$ velocities associated with [OIII] and NaID lines (Fig. 7), suggests the ubiquitous presence of powerful nuclear winds in our sample.
- Most of the nuclei with neutral outflows have relatively low AGN fractions; instead, at $\alpha_{AGN} > 0.5$, NaID outflows are present in one nucleus (out of 8, see Fig. 10, left), confirming the difficulties in observing neutral outflows in systems with strong AGN.

While in the this paper we have presented and described the general properties of the sample and the MUSE data, more detailed studies also involving ALMA data will be presented in future papers.

Acknowledgements. The authors thanks Elena Valenti for her support when preparing the observations. MP is supported by the Programa Atracción de Talento de la Comunidad de Madrid via grant 2018-T2/TIC-11715. MP, SA, CTC and LC acknowledge support from the Spanish Ministerio de Economía y Competitividad through the grant ESP2017-83197-P, and PID2019-106280GB-I00. MPS acknowledges support from the Comunidad de Madrid through the Atracción de Talento Investigador Grant 2018-T1/TIC-11035 and PID2019-105423GA-I00 (MCIU/AEI/FEDER,UE). EB acknowledges support from Comunidad de Madrid through the Attracción de Talento grant 2017-T1/TIC-5213. SC acknowledge financial support from the State Agency for Research of the Spanish MCIU through the "Center of Excellence Severo Ochoa" award to the Instituto de Astrofísica de Andalucía (SEV-2017-0709). ACG acknowledges support from the Spanish Ministerio de Economía y Competitividad through the grant BES-2016-078214.

References

Alcorn, L.Y., Tran K.-V., Glazebrook K. et al., 2018, ApJ, 858, 47
Arribas S., Colina L., Alonso-Herrero A., et al. 2012, A&A, 541, 20
Arribas S., Colina L., Monreal-Ibero A. et al. 2008, A&A, 479, 687
Arribas S., Colina L., Bellocchi E. et al. 2014, A&A, 568, 14A
Bacon, R., Accardo, M., Adjali, L., et al. 2010, in Society of Photo-Optical Instrumentation Engineers (SPIE) Conference Series, Vol. 7735, Society of Photo-Optical Instrumentation Engineers (SPIE) Conference Series, 773508
Bae H.J. & Woo J.H., 2014, ApJ, 795, 30
Bae H. & Woo J., 2018, ApJ, 853, 185
Baldwin J.A., Phillips M.M. & Terlevich R. 1981, PASP, 93, 5B
Baron D., Netzer N., Davies R.I., Prochaska J.X., 2020, arXiv:2004.04749
Barrera-Ballersteros J.K., García-Lorenzo, Falcón-Barroso J., et al., 2015, A&A, 582, 21
Bedregal A.G., Colina L., Alonso-Herrero A., Arribas S., 2009, ApJ, 698, 1852
Belfiore F., Maiolino R., Maraston C. et al. 2016, MNRAS, 461, 3111B
Belfiore F., Westfall K.B., Schaefer A., et al., 2019, ApJ, 158, 160
Bellocchi E., Arribas S., Colina L., Miralles-Caballero, D., 2013, A&A, 557, 59
Bellocchi E., Arribas S., Colina L., 2016, A&A, 591, 85
Bischetti M., Maiolino R., Carniani S. et al. 2019, A&A, 630, 59
Bothwell M.S., Smail I., Chapman S.C., et al., 2013, MNRAS, 429, 3047
Brusa M., Bongiorno A., Cresci G., et al., 2015, MNRAS, 446, 2394B
Calzetti D., Armus L., Bohlin R.C. et al., 2000, ApJ, 533, 682
Cappellari M., Copin Y., 2003, MNRAS, 342, 345C
Cappellari M. & Emsellem E. 2004, PASP, 116, 138C
Cappellari M. 2017, MNRAS, 466, 798
Cardelli, J. A., Clayton, G. C., & Mathis, J. S. 1989, ApJ, 345, 245
Carniani, S., Marconi, A., Maiolino, R., et al., 2016, A&A, 591, 28
Casey, Caitlin M.; Narayanan, Desika; Cooray, Asantha, 2014, PhR, 541, 45
Cazzoli S., Arribas S., Maiolino R., Colina L., 2016, A&A, 590, A125
Ceverino D., Klessen R.S., Glover S.C.O., et al. 2018, MNRAS, 480, 4842
Cicone C., Maiolino R., Sturm E., et al. 2014, A&A, 562, 21
Cicone C., Maiolino R., Marconi A., 2016, A&A, 588, 41
Cid Fernandes R., Stasińska G., Schlickmann M. S. et al., 2010, MNRAS, 403, 1036
Colina, L., Arribas, S., Borne K.D., 1999, ApJ, 527, 13
Colina, L.; Pereira-Santaella, M.; Alonso-Herrero, A. et al., 2012, ApJ, 749, 116
Condon, J. J., Anderson, M. L., & Helou, G. 1991, ApJ, 376, 95
Cresci G., Mainieri V., Brusa M., et al., 2015, ApJ, 799, 81C
Curti M., Cresci G., Mannucci F. et al. 2017, MNRAS, 465, 1384C
D'Agostino J.J., Kewley L.J., Groves B.A., et al., 2019, MNRAS, 487, 4153
Davé R., Anglés-Alcázar D., Narayanan D. et al., 2019, MNRAS, 486, 2827
Dale, D.A.; Giovanelli, R.; Haynes, M. P. et al., 2001, AJ, 121, 1886
Davies R.L., Dopita M.A., Kewley L., et al., 2016, ApJ, 824, 50
de Amorin A.L., García-Benito R., Cid Fernandes R., et al., 2017, MNRAS, 471, 3727
Dekel, A., Birnboim, Y., Engel, G., 2009, Nature, 457, 451
Dekel A., Sarkar K.C., Fangzhou J. et al., 2019, MNRAS, 488, 4753
Dey A., Schlegel D.J., Lang D., et al. 2018, AJ, 157, 168
Díaz A.I., Pagel B.E.J., Wilson I.R.G. 1985, MNRAS, 212, 737
Díaz, A. I., Castellanos, M., Terlevich, E., Luisa García-Vargas, M. 2000, MNRAS, 318, 462
Di Matteo T., Springel V., Hernquist L., 2005, Nature, 433, 604
Dong X. et al., 2008, MNRAS, 383,581
Duc, P.-A., Mirabel, I. F., & Maza, J. 1997, A&AS, 124, 533
Duras F., Bongiorno A., Ricci F., et al., 2020, A&A, arXiv:2001.09984
Eisenhardt P. R. M. et al., 2012, ApJ, 755, 173
Emonts B.H.C., Carilli C., Narayanan D., et al., 2018, ASPC, 517, 587
Evans A.S., Sanders D.B., Cutri R.M., et al., 1998, ApJ, 506, 205
Falcón-Barroso J., Lyubenova M, van de Ven G., et al., 2017, A&A, 597, 48
Feruglio C., Maiolino R., Piconcelli E. et al. 2010, A&A, 518, 155F
Fiore F., Feruglio C., Shankar F. et al., 2017 A&A, 601, 143
Fluetsch A., Maiolino R., Carniani S., et al., 2019, MNRAS, 483, 4586
Fluetsch A., Maiolino R., Carniani S., et al., 2020, arXiv:2006.13232
Föerster-Schreiber N.M., Renzini A., Mancini C., et al., 2018, ApJS, 238, 21
Gadotti D.A., Sánchez-Blázquez P., Falcón-Barroso J., et al., 2019, MNRAS, 482, 506
Gaia Collaboration, 2018, A&A, 616, 1G
García-Marín M., Colina L., Arribas S., 2009a, A&A, 505, 1319
García-Marín M., Colina L., Arribas S., 2009b, A&A, 505, 1017
Genzel R., Lutz D., Sturm E., et al., 1998, ApJ, 498, 2, 579
Genzel R., Föerster-Schreiber N.M., Rosario D., et al., 2014, ApJ, 796, 7
Grimes, J. P., Heckman, T., Strickland, D., & Ptak, A. 2005, ApJ, 628, 187
Groves B. A., Dopita M. A., Sutherland R. S., 2004, ApJS, 153, 9
Harrison C.M., Alexander D. M., Mullaney J. R., Swinbank A. M., 2014, MNRAS, 441, 3306
Harshan A., Gupta A., Tran K.V., et al., 2020, ApJ, arXiv:2002.08353
Heckman, T. M. 1980, A&A, 87, 152
Heckman, T. M., Armus, L., & Miley, G. K. 1987, AJ, 93, 276
Heckman, T. M., Armus, L., & Miley, G. K. 1990, ApJS, 74, 833
Heckman T.M., Kauffmann G., Brinchmann J. et al., 2004, ApJ, 613, 109H
Hibbard J.E., Vacca W.D. & Yun M.S., AJ, 119, 1130
Hinkle J.T., Veilleux S., & Rupke D.S.N., ApJ, 881, 31
Ho I.T., Kewley L.J., Dopita M.A. et al. 2014, MNRAS444, 3894
Hopkins P. F., Hernquist L., Cox T. J., Keres D., 2008, ApJS, 175, 356
Hopkins, P. F., Cox, T. J., Younger, J. D., & Hernquist, L. 2009a, ApJ, 691, 1168
Hopkins, P. F., Somerville, R. S., Cox, T. J., et al. 2009b, MNRAS, 397, 802
Hopkins P. F., Quataert E., Murray, N. 2012, MNRAS, 421, 3522
Hopkins P. F., Torrey P., Faucher-Giguere C., et al. 2016, MNRAS, 458, 816
Hung, C.-L.; Sanders, D. B.; Casey, C.M. et al., 2013, ApJ, 791, 63
Husemann B., Scharwächter J., Davis T.A. et al., 2019, A&A, 627, 53
Husser T., Kamann S., Dreizler S., et al., 2016, A&A, 588, 148
Iwasawa K., Sanders D.B., Evans A.S, et al., 2005, MNRAS, 357, 565
Iwasawa, K., Sanders, D. B., Teng, S. H., et al. 2011, A&A, 529, A106
Kakkad D., Mainieri V., Vietri G., et al., 2020, A&A, 642, 147
Kartaltepe J.S., Dickinson M., Alexander D.M. et al. 2012, ApJ, 575, 23
Kauffman G., Heckman T.M., Tremonti C., et al, 2003, MNRAS, 346, 1055
Kauffmann, G., et al., 2003b, MNRAS, 341, 33
Kaviraj, S.; Rowlands, K.; Alpaslan, M. et al., 2013, MNRAS, 435, 1463
Kennicutt R.C., 1998, ARA&A, 36, 189K
Kennicutt R.C., Evans N.J., 2012, ARA&A, 50, 513K
Kewley L.J., Dopita M.A., Sutherland R.S., et al., 2001, ApJ, 556, 121
Kewley L.J., Dopita M.A., 2002, ApJS, 142, 35
Kewley L. J., Groves B., Kauffmann G., Heckman T., 2006, MNRAS, 372, 961
Kewley L.J., Maier C., Yabe K., et al., 2013, ApJ, 774, L10
Kim, D.-C., & Sanders, D. B. 1998, ApJS, 119, 41
Kim, D.-C., Evans, A. S., Vavilkin, T., et al. 2013, ApJ, 768, 102
King A., & Pounds K. 2015, ARA&A, 53, 115
Kormendy J. & Ho L.C., 2013, ARAA, 51, 511
Kreckel K., Groves B., Schinnerer E., et al., 2013, ApJ, 771, 62
Kronberger, T.; Kapferer, W.; Schindler, S.; Ziegler, B. L., 2007, A&A, 473, 761
Lister M. L., Kellermann K. I., Vermeulen R. C., 2003, ApJ, 584, 135
Lutz, D.; Veilleux, S.; Genzel, R., 1999, ApJ, 517, 13
Madau P., Dickinson M., 2014, ARA&A, 52, 415
Magnelli, B., Popesso, P., Berta, S., et al. 2013, A&A, 553, A132
Maiolino R., Gallerani S., Neri R., et al., 2012, MNRAS,425, L66
Maiolino R. & Mannucci F., 2019, A&ARv, 27, 3
Martin C.L., 2005, ApJ, 621, 227
Medling, Anne M.; U, Vivian; Guedes, Javiera et al., 2014, ApJ, 784, 70
Mingozzi M., Cresci G., Venturi G., et al. 2019, A&A, 622, 146
Naab, Thorsten; Ostriker, Jeremiah P., 2017, ARA&A, 55, 59N
Nagao, T., Marconi, A., & Maiolino, R. 2006, A&A, 447, 157
Nardini, E., Risaliti, G., Watabe, Y., et al., 2010, MNRAS, 405, 2505
Nedelchev, B., Sarzi, M., Kaviraj, S., 2019, MNRAS, 486, 1608
Ocvirk, P.; Pichon, C.; Teyssier, R., 2008, MNRAS, 390, 1326
Osterbrock D.E. & Ferland G.J., 2006, Astrophysics of Gaseous Nebulae and Active Galactic Nuclei. University Science Books
Pereira-Santaella M., Colina L., García-Burillo S. et al., 2018, A&A, 616, 171
Pérez-González, P. G.; Rieke, George H.; Egami, Eiichi et al., 2005, ApJ, 630, 82P
Perna M., Lanzuisi G., Brusa M., Mignoli M., Cresci G., 2017, A&A, 603A, 99P
Perna M., Cresci G., Brusa M., et al., 2019, A&A, 623, 171
Perna M., Arribas S., Catalan-Torrecilla C., et al., 2020, A&A, arXiv:2009.03353
Petric, A. O.; Ho, L. C.; Flagey, N. J. M.; Scoville, N. Z., 2015, ApJS, 219, 22
Pillepich A., Springel V., Nelson D., et al., 2018, MNRAS, 473, 4077
Rich J.A., Kewley L.J. & Dopita M.A., 2011, ApJ, 734, 87
Rich J.A., Kewley L.J. & Dopita M.A., 2015, ApJS, 221, 28
Rodríguez Zaurín, J., Tadhunter, C. N., Rose, M., & Holt, J. 2013, MNRAS, 432, 138
Rothberg, B., & Joseph R. D., 2004, AJ, 128, 2098
Rupke, D. S., Veilleux, S., & Sanders, D. B. 2002, ApJ, 570, 588
Rupke D.S., Veilleux S. & Sanders D.B., 2005a, ApJS, 160, 87R
Rupke D.S., Veilleux S. & Sanders D.B., 2005b, ApJS, 160, 115R
Rupke D.S., Veilleux S. & Sanders D.B., 2005c, ApJ, 632, 751
Rupke, D. S. N., & Veilleux, S. 2013, ApJ, 775, 15R
Rupke, D. S. N., & Veilleux, S. 2013, ApJ, 768, 75R
Rupke, D. S. N., & Veilleux, S. 2015, ApJ, 801, 126
Rupke D.S.N., Gultekin K., Veilleux S. 2017, ApJ, 850, 40
Sanders D.B., Soifer B.T., Elias J.H., et al., 1988, ApJ, 325, 74S
Sanders D. B., Mazzarella J.M., Kim D.C. et al., 2003, AJ, 126, 1607
Sánchez Almeida J., Elmegreen B.G., Muñoz-Tuñón C. and Elmegreen D.M., 2014, A&ARv, 22, 71
Sato T., Martin C. L., Noeske K. G., et al., 2009, ApJ, 696, 214
Schaye J., Dalla Vecchia C., Booth C.M. et al., 2010, MNRAS, 402, 1536
J. Scharwächter, A. Eckart, S. Pfalzner, et al., 2007, A&A, 469, 913
Schwarz G., 1978, Ann. Stat., 6, 461
Smits D.P., 1996, MNRAS, 278, 683
Silk J., 2013, ApJ, 772, 112S
Soto, K. T.; Lilly, S. J.; Bacon, R. et al., 2016, MNRAS, 458, 3210
Spoon H.W.W., Farrah D., Lebouteilleur V. et al. 2013, ApJ, 775, 127
Somerville R.S. and Davé R., 2015, ARA&A, 53, 51S

Sturm E. et al., 2011, ApJ, 733, L16
Valdes F., Gupta R., Rose J.A., et al., 2004, ApJS, 152, 251
Varenius E., Conway J.E., Batejat F., et al., 2019, A&A, 623, 173
Veilleux S., Osterbrock D.E., 1987, ApJS, 63, 295V
Veilleux, S., Kim, D.-C., & Sanders, D. B. 2002, ApJS, 143, 315
Veilleux S., Cecil G., Bland-Hawthorn J., 2005, ARAA, 43, 769
Veilleux, S., Rupke, D. S. N., Kim, D.-C., et al. 2009, ApJS, 182, 628
Veilleux S., Meléndez M., Sturm E. et al. 2013, ApJ, 776,27V
Veilleux S., Bolatto A., Tombesi F., et al., 2017, ApJ, 843, 18V
Veilleux S., Maiolino R., Bolatto A.D., Aalto S., 2020, A&ARv, 28, 2
Venturi G., Nardini E., Marconi A. et al. 2018, A&A, 619, 74
Véron-Cetty, M. -P.; Joly, M.; Véron, P., 2004, A&A, 417, 515
Villar Martín M., Perna M., Humphrey A., et al., 2020, A&A, 634, 116
Westmoquette M.S., Clements D.L., Bendo G.J. & Khan S.A. MNRAS, 424, 416W
Wisnioski, E., Mendel, J. T., Föerster-Schreiber N.M. et al., 2018, ApJ, 855, 97
Woo J.H., Bae H.J., Son D. & Karouzos M., 2016, ApJ, 817, 108W
Yuan F.T., Argudo-Fernández M., Shen S. et al.2018, A&A, 613, 13
Yun M.S., Reddy N.A., Condon J.J., 2001, ApJ, 554, 803

Appendix A: Spectroscopic redshifts

Table A.1 display all spectroscopic redshifts we derived modelling the stellar continuum and line features of nuclear spectra, as well as of ULIRG nearby companions detected in the MUSE data cubes. Coordinates, velocity offsets and projected distances from the bright nucleus of each ULIRG are also reported.

Appendix B: Seyfert 1 fit analysis

For the two Sy 1 nuclear spectra, we proceed in two steps. First, we modelled the continuum with a power-law, and the iron emission components with the observational templates of Véron-Cetty et al. (2004). This initial fit was performed considering the wavelength ranges 4050 – 7100Å (for F01572+0009) and 4450 – 7100Å (for Izw1), but masking all other prominent emission lines, namely the BLR Balmer and He lines, as well as the NLR forbidden [OIII], [NII], [SII], [OI] features. We therefore obtained a template for the continuum and iron emission, to be used in the second step.

Then, we modelled all remaining emission lines with a combination of Gaussian profiles, as well as broken power law functions (e.g. Cresci et al. 2015) for the BLR emission components, together with the continuum and iron components (for which we obtained good initial estimates for the fit parameters from the previous step). This analysis is very similar to the one presented in Sect. 6, apart from the following aspects. Additional emission lines are detected and included in the fit of Sy 1 spectra: the Balmer Hγ and Hδ, the Si II$\lambda\lambda$6347,6371, the He II at 4685Å and He I lines at 4387, 4713, 4921, 5875, 6678 and 7065Å. To model the Balmer emission lines, we used two parameters for the Hα and Hβ amplitudes, and derived the Hα /Hβ flux ratio to measure the dust extinction, using the Cardelli et al. (1989) extinction law and assuming a Case B recombination as well as $T_e = 10^4$ K. This dust correction is then used to infer the fluxes of Hγ and Hδ, considering the Case B recombination flux ratios H$\gamma/H\beta$ = 0.468 and H$\delta/H\beta$ = 0.260. Similarly, we consider the standard He I theoretical intensity ratios from Smits (1996) to constrain the fluxes of all He I transitions: In particular, we assumed low-density plasma conditions (with $T_e = 10^4$ K and $N_e = 10^3$ cm^{-3}) for the NLR component, and high-density conditions (with $T_e = 10^4$ K and $N_e = 10^6$ cm^{-3}) for the BLR. Therefore, we used a unique parameter for the HeIλ4471 flux amplitude, and the theoretical intensity ratios to infer the fluxes of the remaining transitions, correcting for the dust extinction (from the Balmer decrement). For the BLR components, we assumed that all Balmer and helium lines have the same broken power-law indices (e.g. Nagao et al. 2006) and kinematics. BLR emission components have been used for all permitted transitions (see e.g. Véron-Cetty et al. 2004).

Appendix C: Individual ULIRGs

Figures C.1-C.89 display the three-colour composites, stellar and emission line maps, as well as the nuclear spectra for each ULIRG presented in this paper.

Table A.1. ULIRGs nuclei and companions (pPXF spectroscopic) redshifts and positions.

source name	RA ($^h:{}^m:{}^s$)	DEC ($^\circ:{}':{}''$)	z	ΔV (km/s)	Projected distance ($''$/kpc)
(1)	(2)	(3)	(4)	(5)	(6)
F00188-0856	0:21:26.52	−8:39:25.92	0.1284 ± 0.0001	-	-
F00188-0856: c	0:21:25.43	−8:39:18.46	0.1219 ± 0.0001	−60 ± 25	18.0/41.6
IZw1	0:53:34.93	+12:41:35.94	0.0611 ± 0.0001	-	-
IZw1: c	0:53:33.88	+12:41:33.63	0.0613 ± 0.0002	+60 ± 25	15.5/18.4
F01572+0009	1:59:50.25	+0:23:40.87	0.1632 ± 0.0001	-	-
F01572+0009: c	1:59:48.76	+0:23:43.49	0.1623 ± 0.0001	−244 ± 10	21.7/61.3
F05189-2524	5:21:01.40	−25:21:45.30	0.0428 ± 0.0001	-	-
07251-0248 E	7:27:37.61	−2:54:54.25	0.0879 ± 0.0001	-	-
07251-0248 W	7:27:37.54	−2:54:54.39	0.0881 ± 0.0001	55 ± 10	1.1/1.8
09022-3615	9:04:12.71	−36:27:01.93	0.0596 ± 0.0001	-	-
10190+1322 W	10:21:42.49	+13:06:53.83	0.0767 ± 0.0001	-	-
10190+1322 E	10:21:42.75	+13:06:55.61	0.0758 ± 0.0001	−264 ± 10	4.9/7.2
10190+1322: c_{SE}	10:21:43.83	+13:06:47.54	0.0760 ± 0.0001	−187 ± 11	20.6/30.1
10190+1322: c_{NW}	10:21:41.88	+13:07:06.36	0.0771 ± 0.0001	120 ± 11	15.8/23.1
F11095-0238 NE	11:12:03.38	−2:54:22.94	0.1064 ± 0.0001	-	-
F11095-0238 SW	11:12:03.36	−2:54:23.30	0.1065 ± 0.0002	+30 ± 18	0.6/1.1
F12072-0444 N	12:09:45.12	−5:01:13.31	0.1288 ± 0.0001	-	-
F12072-0444 S	12:09:45.13	−5:01:14.23	0.1288 ± 0.0001	−7 ± 10	1.0/2.3
F12072-0444: c_1	12:09:44.81	−5:00:54.78	0.1302 ± 0.0006	360 ± 30	19.1/44.2
F12072-0444: c_2	12:09:44.82	−5:00:52.33	0.1302 ± 0.0006	360 ± 30	21.6/49.94
13120-5453	13:15:06.32	−55:09:22.82	0.0310 ± 0.0001	-	-
F13451+1232 W	13:47:33.36	+12:17:24.24	0.1218 ± 0.0002	-	-
F13451+1232 E	13:47:33.49	+12:17:23.76	0.1218 ± 0.0002	−5 ± 10	2.0/4.3
F14348-1447 SW	14:37:38.28	−15:00:24.24	0.0824 ± 0.0002	-	-
F14348-1447 NE	14:37:38.40	−15:00:21.29	0.0822 ± 0.0002	−49 ± 30	3.4/5.3
F14348-1447: c	14:37:38.95	−15:00:25.47	0.0823 ± 0.0001	−22 ± 8	10.3/16.1
F14378-3651: n	14:40:58.89	−37:04:32.08	0.0682 ± 0.0001	-	-
F14378-3651: c	14:41:01.15	−37:04:43.94	0.0684 ± 0.0001	48 ± 7	29.7/38.9
F15327+2340 (Arp220): n_W	15:34:57.24	+23:30:11.70	0.0181 ± 0.0001	-	-
F15327+2340 (Arp220): n_E	15:34:57.30	+23:30:11.90	0.0182 ± 0.0001	30 ± 9	1/0.37
F16090-0139: n	16:11:40.42	−1:47:06.56	0.1337 ± 0.0002	-	-
17208-0014: n	17:23:21.94	−00:17:00.96	0.0430 ± 0.0001	-	-
F19297-0406 S	19:32:22.30	−4:00:01.80	0.0854 ± 0.0001	-	-
F19297-0406 N	19:32:22.31	−4:00:01.03	0.0853 ± 0.0001	−25 ± 9	0.7/1.1
19542+1110	19:54:35.78	11:19:05.03	0.0624 ± 0.0002	-	-
19542+1110: c	19:54:34.91	11:19:20.94	0.0628 ± 0.0001	40 ± 15	20.5/24.8
20087-0308	20:11:23.87	−2:59:50.71	0.1052 ± 0.0001	-	-
20100-4156 SE	20:13:29.56	−41:47:35.21	0.1297 ± 0.0002	-	-
20100-4156 NW	20:13:29.48	−41:47:32.58	0.1297 ± 0.0001	−6 ± 10	2.8/6.5
20100-4156 c	20:13:28.63	−41:47:38.39	0.1300 ± 0.0001	90 ± 8	10.5/24.3
F22491-1808 W	22:51:49.24	−17:52:23.66	0.0776 ± 0.0001	-	-
F22491-1808 E	22:51:49.35	−17:52:24.12	0.0777 ± 0.0002	+35 ± 9	1.8/2.7

Note. Column (1): target name; (2) and (3): coordinates (RA and DEC); (4): spectroscopic redshift from pPXF, at the position of the stellar continuum peak. (5): velocity with respect to the ULIRG systemic. (6): projected distance from the ULIRG (brightest) nucleus.

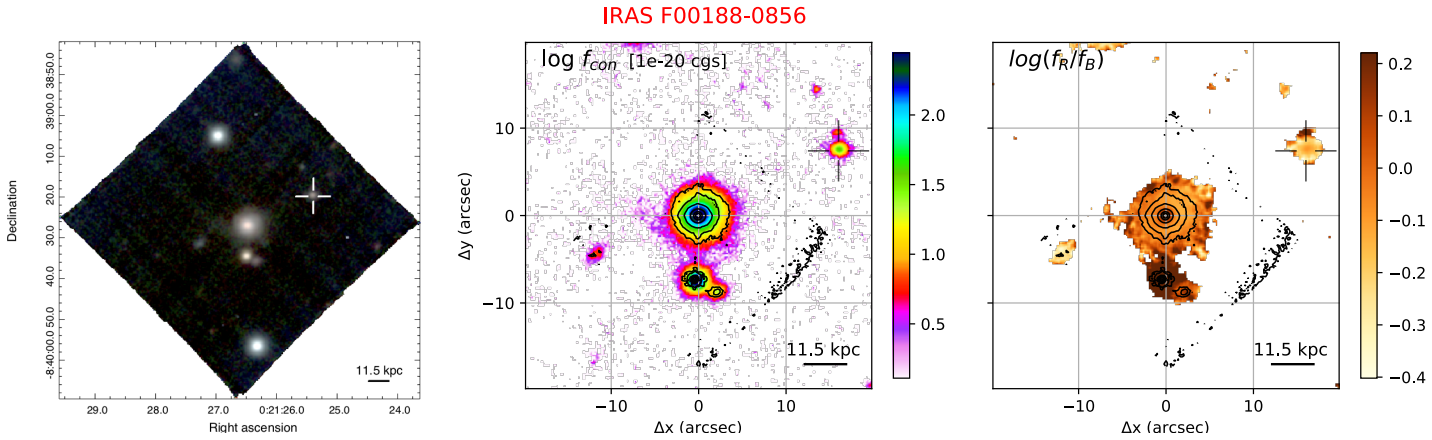

Fig. C.1. IRAS F00188-0856 images from MUSE observations with TOT = 0.68 hr. *Left*: colour composite optical image, showing [OIII] (green, from the wavelength range 4990 – 5015Å rest-frame), Hα (red, 6555 – 6574Å) and stellar continuum (blue, 4400 – 4500Å). *Centre*: red (7390 – 7530Å) continuum image, with contours from HST/F160W. *Right*: continuum colour map obtained from MUSE, by dividing the red continuum image (in the central panel) by a blue image obtained collapsing the stellar emission in the range 4400 – 4500Å; contours from HST/F160W. In all panels, we display the IRAS F00188-0856 companion with a cross marker.

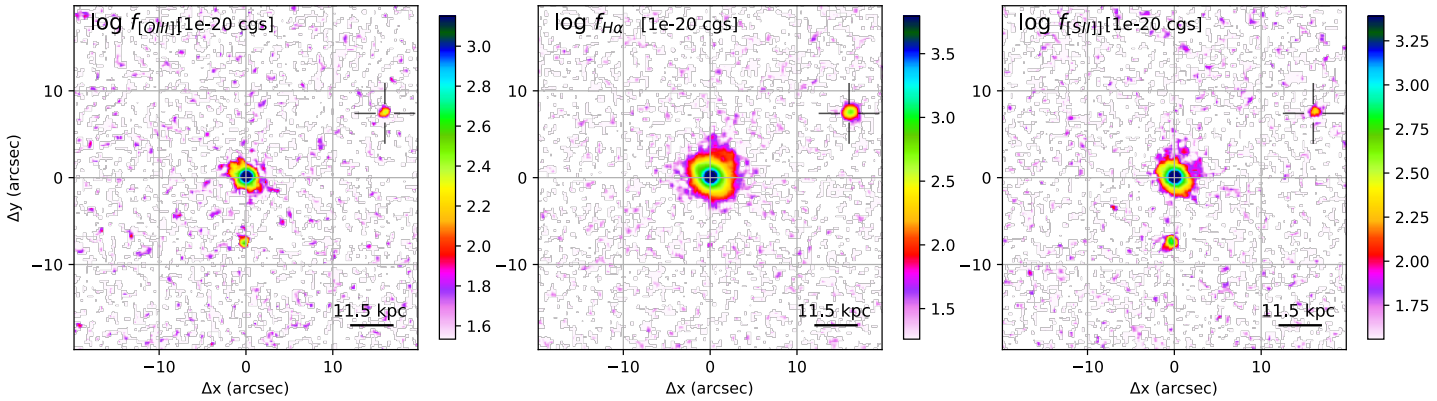

Fig. C.2. IRAS F00188-0856 emission lines images from MUSE observations. [OIII] (left, from the wavelength range 4990 – 5015Å rest-frame), Hα (centre, 6555 – 6574Å) and [SII] (right, 6702 – 6742Å) images have been obtained subtracting continuum emission using the adjacent regions at shorter and longer wavelengths with respect to the emission line systemics. In all panels, we display the position of companion galaxy with a cross marker.

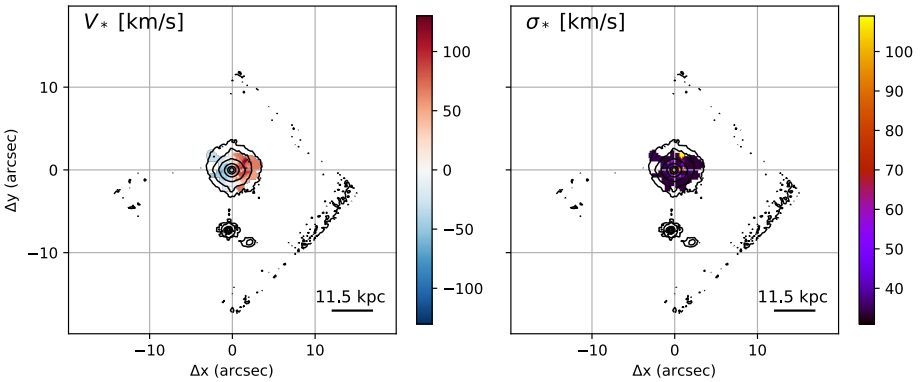

Fig. C.3. IRAS F00188-0856 stellar kinematic maps from pPXF analysis, with contours from HST/F160W. The left panel shows the stellar velocity V_*, while the right one displays the velocity dispersion σ_*.

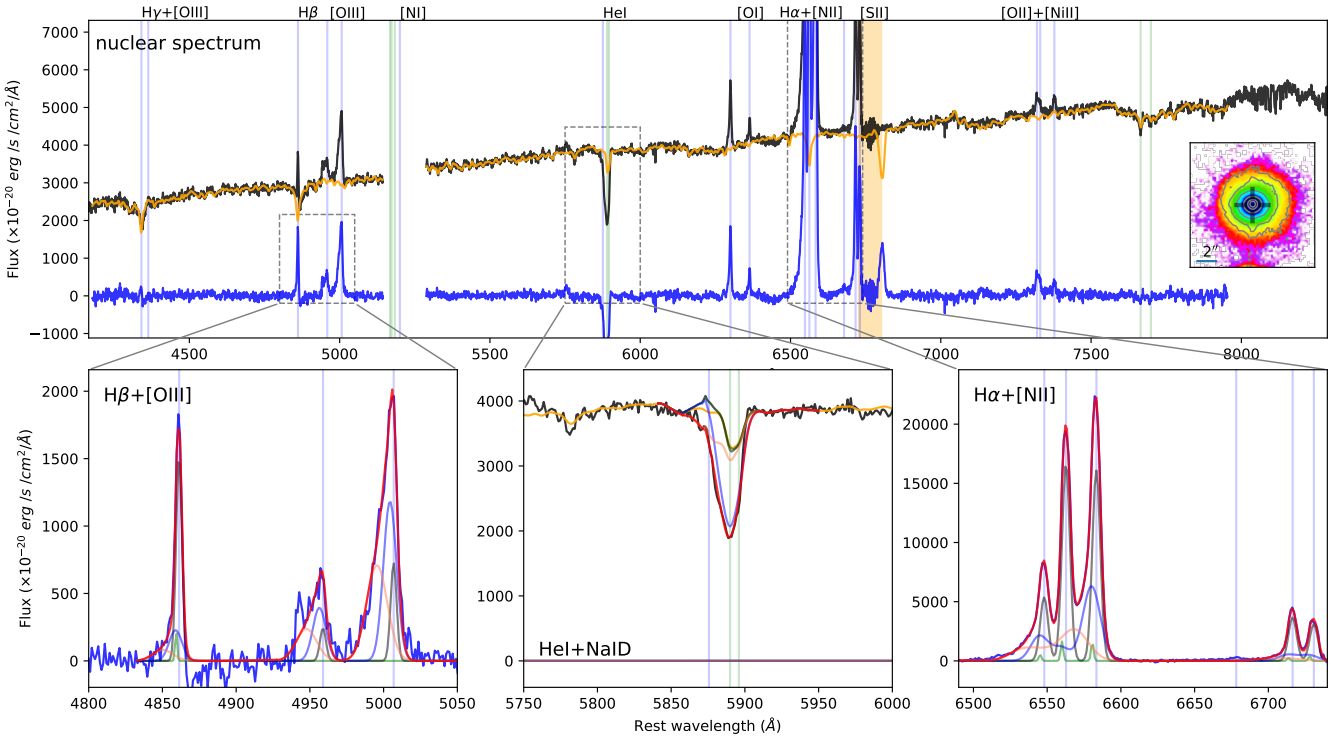

Fig. C.4. *Top panel*: IRAS F00188-0856 nuclear spectrum (black curve), extracted from a circular aperture with $r < 0.4''$. The corresponding pPXF best-fit model profile is shown in orange. The continuum-subtracted spectrum (blue curve) is obtained subtracting the best-fit pPXF model from the original spectrum. The vertical blue lines mark the wavelengths of the emission lines detected in the spectrum; the vertical green lines mark the position of stellar absorption systems (i.e. from left to right: MgI triplet, NaID and KI doublets). The region excluded from the pPXF fit and corresponding to the most intense sky line residuals are highlighted as orange shaded areas; the portions of the spectra around 5300 Å are missing, because of a filter blocking the laser contamination. The inset in the top panel shows the red stellar continuum emission map in the vicinity of the nuclear regions, with HST/F160W contours as in Fig. C.1; the nuclear position is shown with a black marker. *Bottom insets*: Multi-component best-fit analysis results for the main emission (Hβ and [OIII], left; Hα, [NII] and [SII], right) and absorption (NaID, centre) line features. NaID multi-component best-fit curves are superimposed on the observed spectrum (black curve); emission components are not required to reproduce the total profile of NaID.

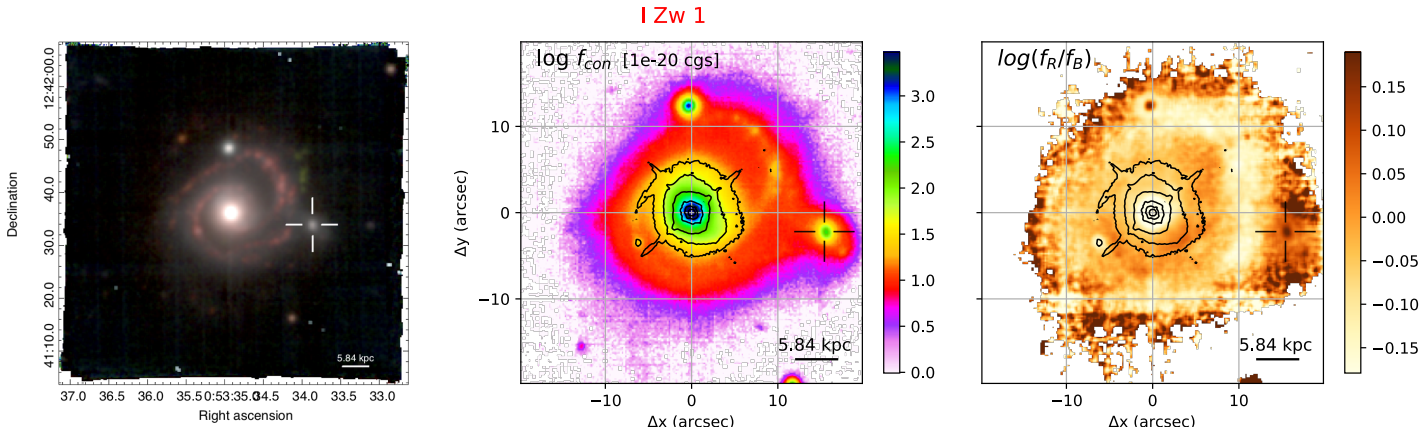

Fig. C.5. IZw1 images from MUSE observations with TOT = 2.72 hr. *Left*: colour composite optical image, showing [OIII] (green, from the wavelength range 4959 – 5018Å rest-frame), Hα (red, 6552 – 6570Å) and stellar continuum (blue, 4570 – 4670Å). *Centre*: red (8010 – 8110Å) continuum image from MUSE , with contours from HST/F160W. *Right*: continuum colour map obtained from MUSE, by dividing the red continuum image (central panel) by a blue image obtained collapsing the stellar emission in the range 4570 – 4670Å; contours from HST/F160W. In all panels, we display the IZw1 companion galaxy with a cross marker.

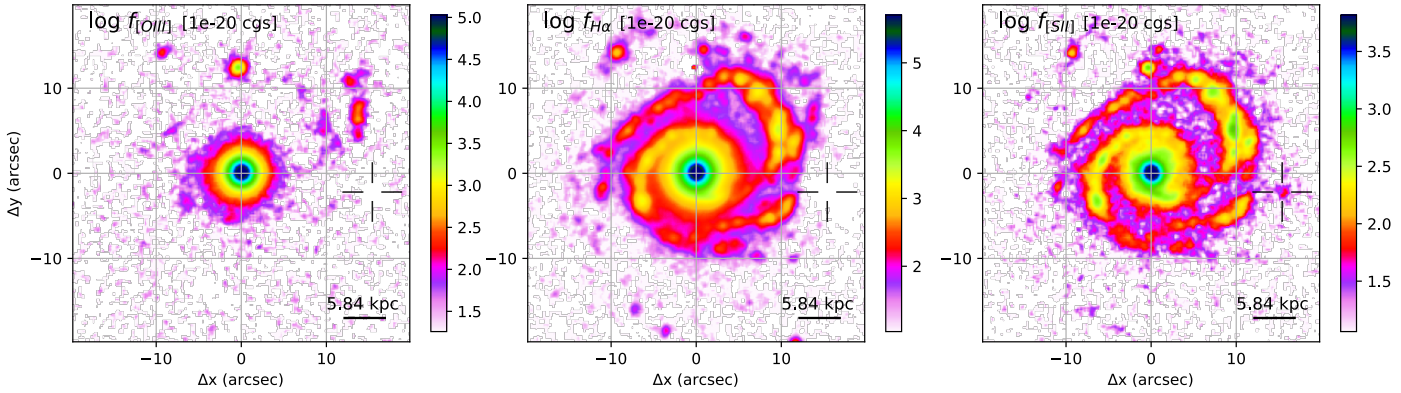

Fig. C.6. IZw1 emission lines images from MUSE observations. [OIII] (left, from the wavelength range 4985 – 5018Å rest-frame), Hα (centre, 6552 – 6570Å) and [SII] (right, 6710 – 6741Å) images have been obtained subtracting continuum emission using the adjacent regions at shorter and longer wavelengths with respect to the emission line systemics. In all panels, we display the position of the non-emission line companion galaxy of IZw1 with cross markers.

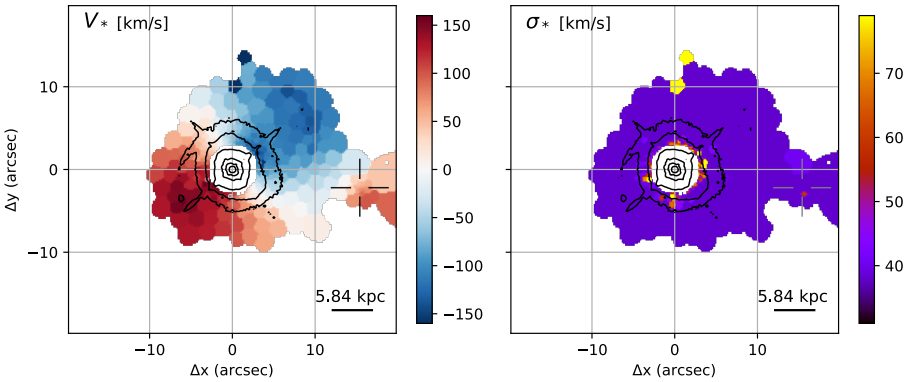

Fig. C.7. *Left*: IZw1 stellar kinematic maps from pPXF analysis, with contours from HST/F160W. The left panel shows the stellar velocity V_*, while the right one represents the velocity dispersion σ_*. The central pixels have been masked, because of the presence of strong AGN continuum and BLR emission, which prevents the detection of stellar continuum and absorption features.

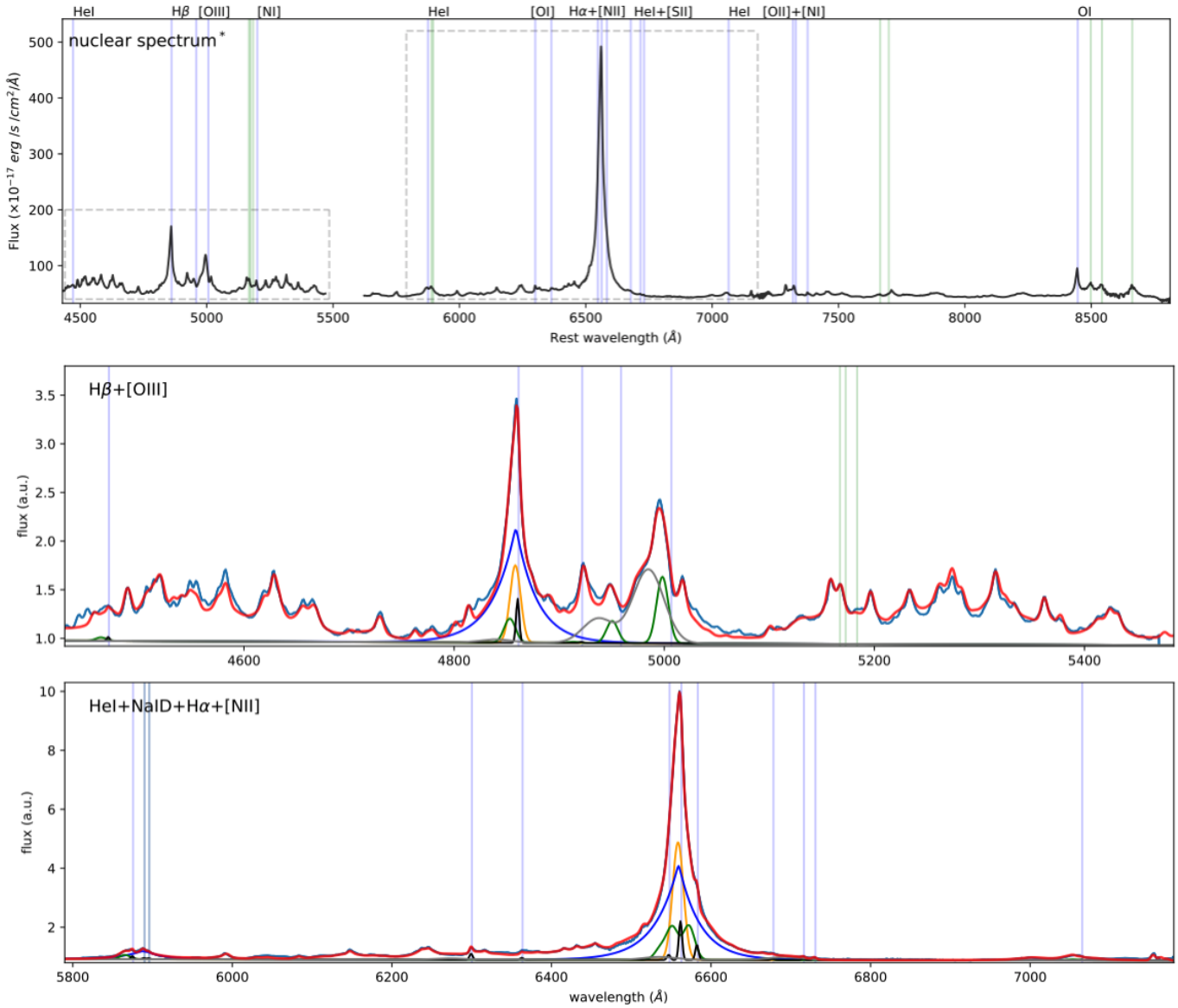

Fig. C.8. *Top*: IZw1 nuclear spectrum (black curve), extracted from a circular aperture $r < 0.4''$ but excluding the central pixel (where Hα is saturated). The blue vertical lines mark the wavelengths of the emission lines detected in the spectrum; the green lines mark the position of stellar absorption systems (i.e. from left to right: MgI triplet, NaID and KI doublets, CaII triplet). The latter transitions in absorption are not detected, because of the strong AGN continuum and emission lines. The portions of the spectra around 5500 Å are missing, because of a filter blocking the laser contamination; the portions in the two boxes are reported in the central and bottom panels, with the best-fit curves. *Centre*: normalized nuclear spectrum in the vicinity of the Hβ+[OIII] complex (blue curve), with total best-fit model (red). Individual kinematic components are shown with different colours: black, green and grey Gaussians represent systemic and outflow components; blue and orange curves are used to model the BLR Balmer emission; iron components are not reported. *Bottom*: normalized nuclear spectrum in the vicinity of the HeI+NaID and Hα+NII complexes (blue curve), with superimposed best-fit model (red curve). Different kinematic components required to reproduce the spectrum are shown as in the central panel.

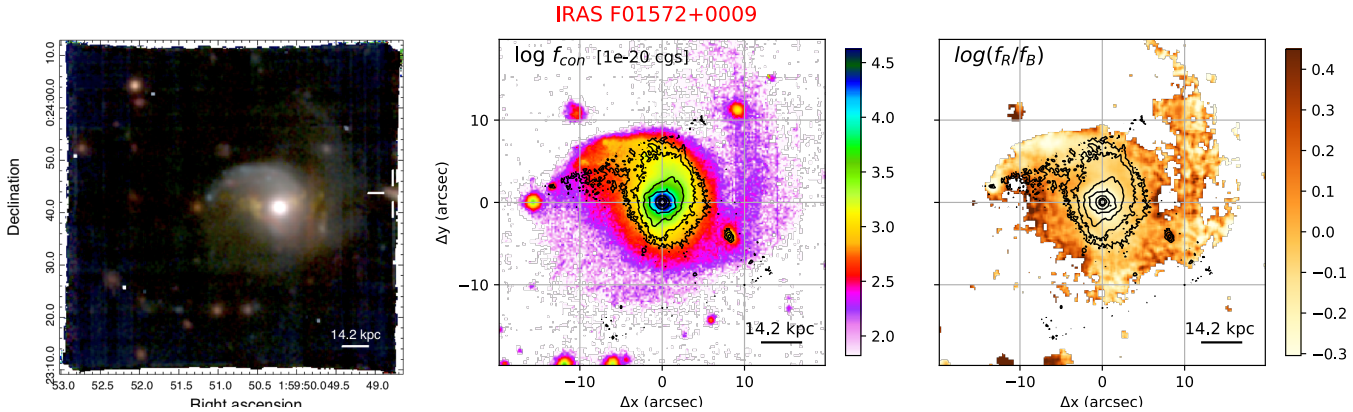

Fig. C.9. IRAS F01572+0009 images from MUSE observations with TOT = 2.04 hr. *Left*: colour composite optical image, showing [OIII] (green, from the wavelength range 4925 – 4970Å rest-frame), Hα (red, 6550 – 6575Å) and continuum (blue, 4150 – 4220Å). *Centre*: red (7330 – 7400Å) continuum image from MUSE, with contours from HST/F160W. *Right*: continuum colour map obtained from MUSE, by dividing the red continuum image (central panel) by a blue image obtained collapsing the stellar emission in the range 4150 – 4220Å; contours from HST/F160W. In the first panel, we display the F01572+0009 companion galaxy with a cross marker.

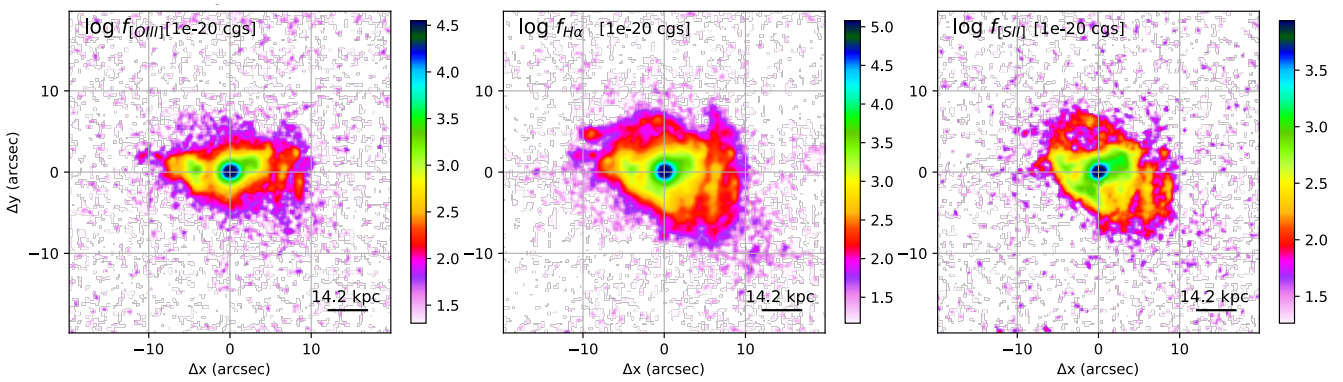

Fig. C.10. IRAS F01572+0009 emission lines images from MUSE observations. [OIII] (left, from the wavelength range 4925 – 4970Å rest-frame), Hα (centre, 6550 – 6575Å) and [SII] (right, 6700 – 6748Å) images have been obtained subtracting continuum emission using the adjacent regions at shorter and longer wavelengths with respect to the emission line systemics.

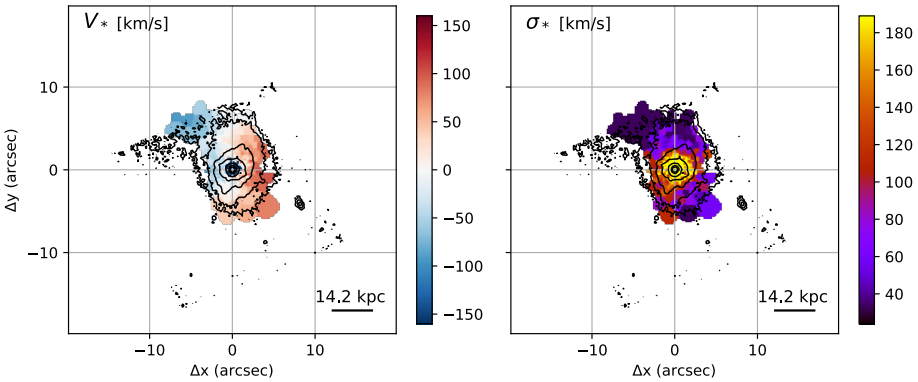

Fig. C.11. *Left*: IRAS F01572+0009 stellar kinematic maps from pPXF analysis, with contours from HST/F160W. The left panel shows the stellar velocity V_*, while the right one represents the velocity dispersion σ_*.

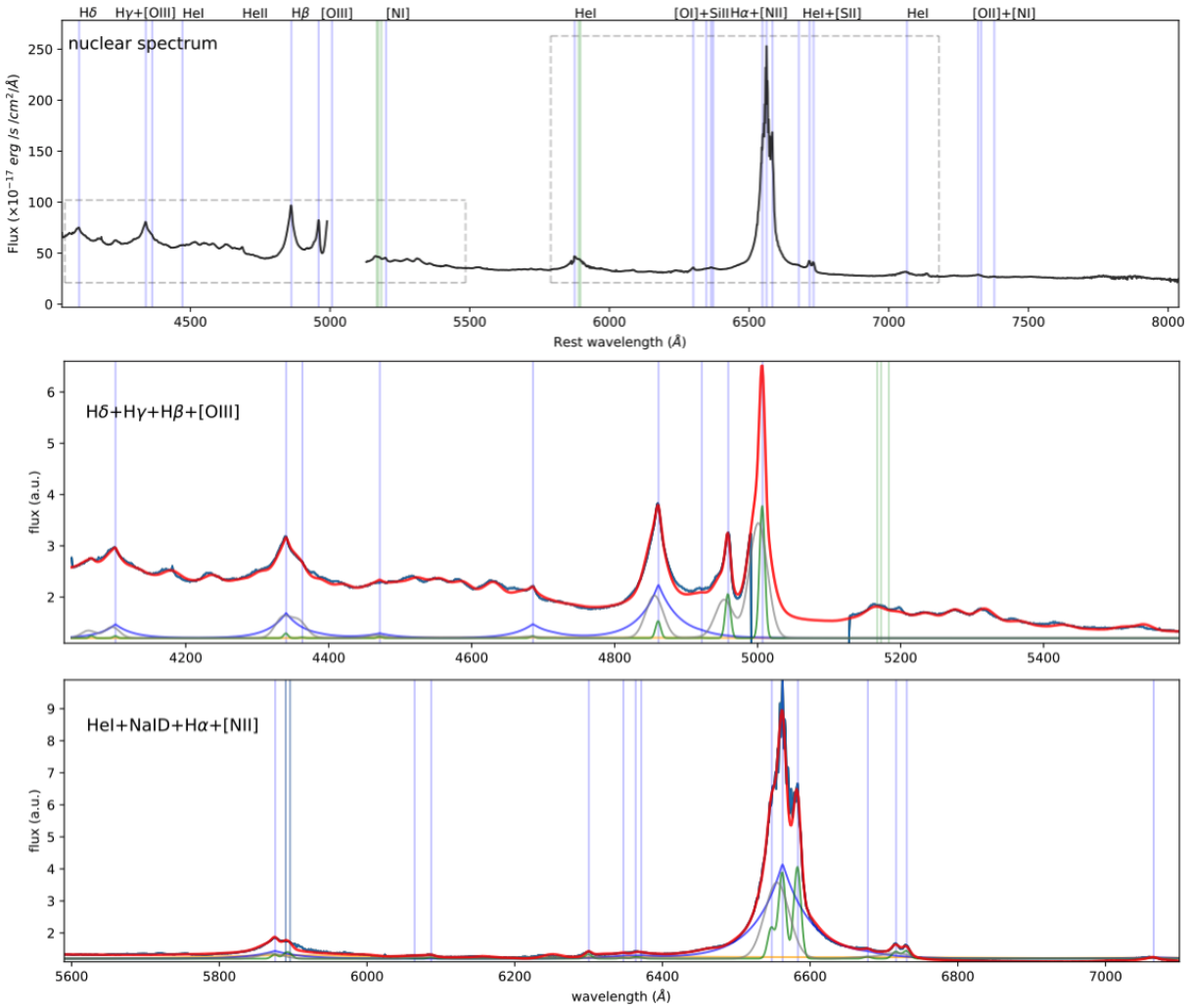

Fig. C.12. *Top*: IRAS F01572+0009 nuclear spectrum (black curve), extracted from a circular aperture $r < 0.4''$. The blue vertical lines mark the wavelengths of the emission lines detected in the spectrum; the green lines mark the position of stellar absorption systems (i.e. from left to right: MgI triplet, and NaID doublets). The latter transitions in absorption are not detected, because of the strong AGN continuum and emission lines. The portions of the spectra around 5050 Å are missing, because of a filter blocking the laser contamination; the portions in the two boxes are reported in the central and bottom panels, with the best-fit curves. *Centre*: normalized nuclear spectrum in the vicinity of the Hβ+[OIII] complex (blue curve), with total best-fit model (red). Individual kinematic components are shown with different colours: green and grey Gaussians represent systemic and outflow components, respectively; blue and orange curves are used to model the BLR Balmer emission; iron components are not reported. [OIII]λ5007 line is mostly within the missing portion of the spectrum; this profile has been reconstructed using the [OIII]λ4959 transition. *Bottom*: normalized nuclear spectrum in the vicinity of the HeI+NaID and Hα+NII complexes (blue curve), with superimposed best-fit model (red curve). Different kinematic components required to reproduce the spectrum are shown as in the central panel.

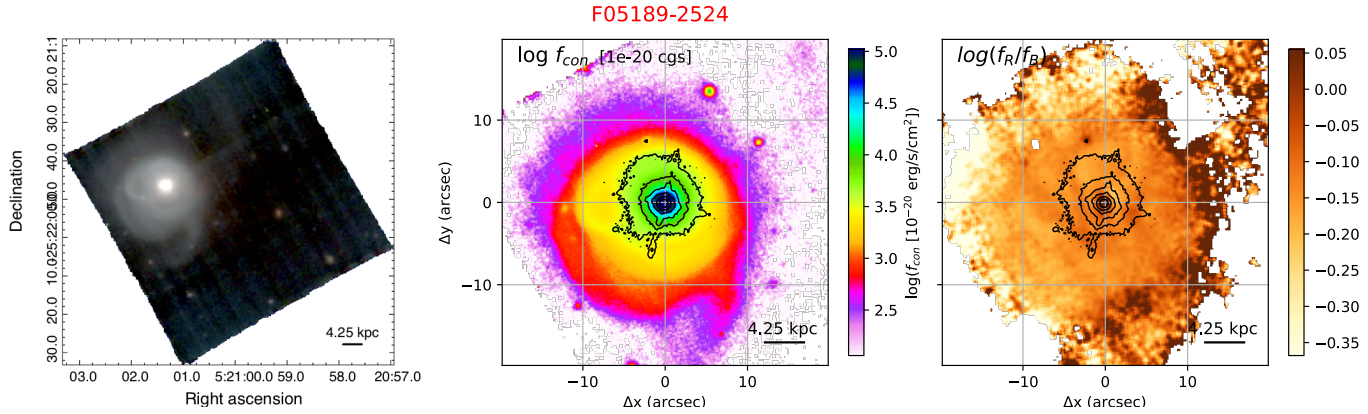

Fig. C.13. IRAS F05189-2524 images from MUSE observations with TOT = 2.04 hr. *Left*: colour composite optical image, showing [OIII] (green, from the wavelength range 4962 – 5022Å rest-frame), Hα (red, 6554 – 6578Å) and continuum (blue, 4530 – 4660Å) emission. *Centre*: red (8025 – 8150Å) continuum image from MUSE, with contours from HST/F160W. *Right*: continuum colour map obtained from MUSE, by dividing the red continuum image (central panel) by a blue image obtained collapsing the emission in the range 4530 – 4660Å; contours from HST/F160W.

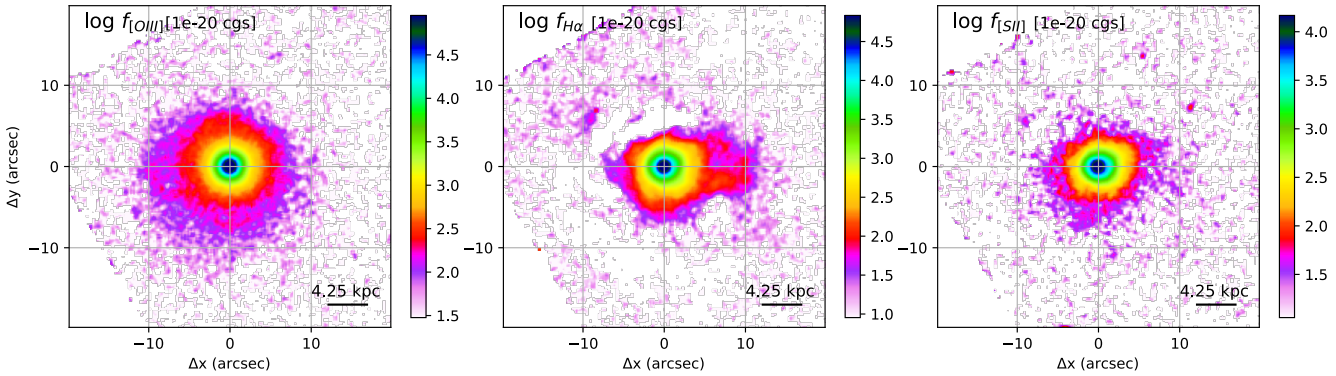

Fig. C.14. IRAS F05189-2524 emission lines images from MUSE observations. [OIII] (left, from the wavelength range 4962 – 5022Å rest-frame), Hα (centre, 6554 – 6578Å) and [SII] (right, 6694 – 6742Å) images have been obtained subtracting continuum emission using the adjacent regions at shorter and longer wavelengths with respect to the emission line systemics.

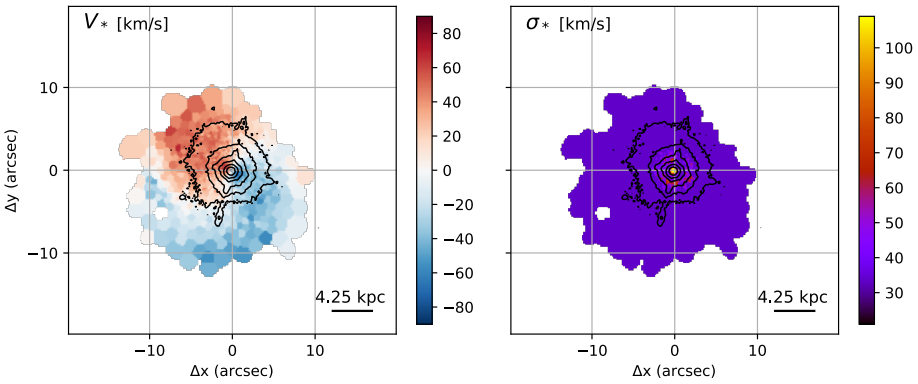

Fig. C.15. *Left*: IRAS F05189-2524 stellar kinematic maps from pPXF analysis, with contours from HST/F160W. The left panel shows the stellar velocity V_*, while the right one represents the velocity dispersion σ_*.

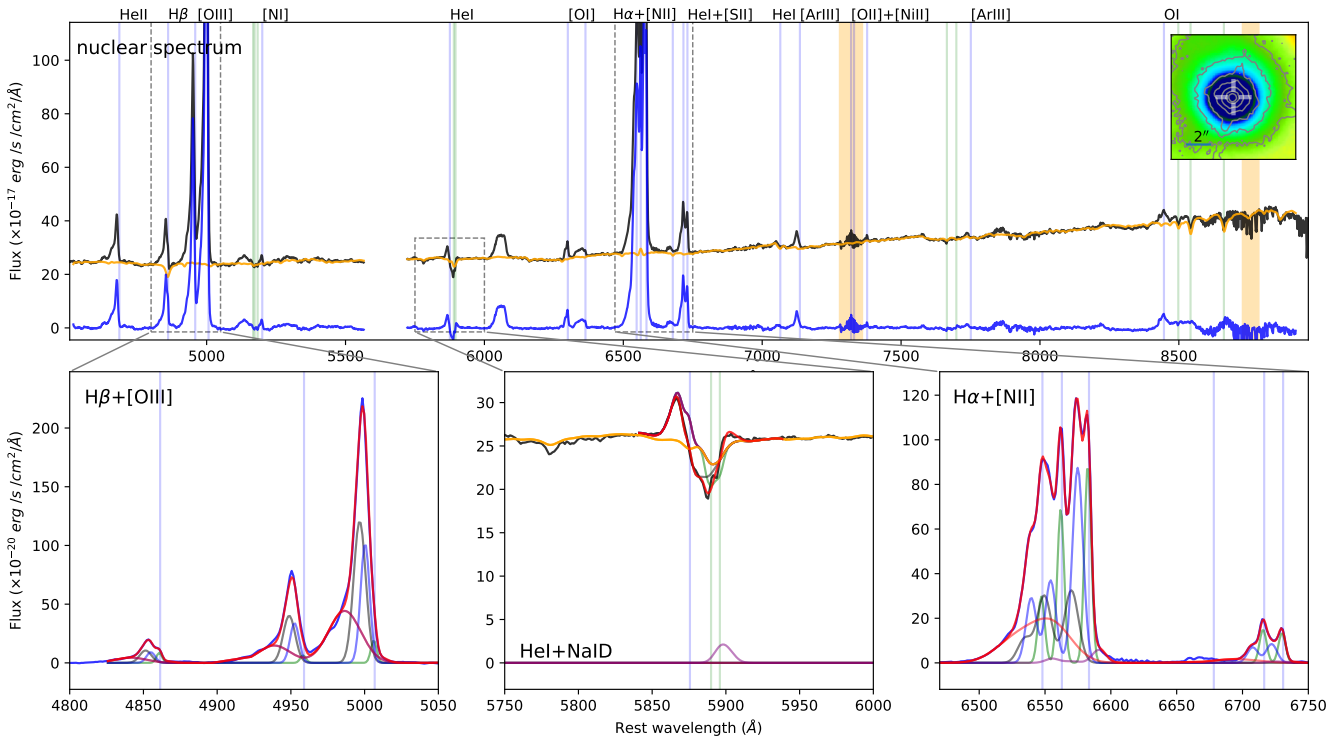

Fig. C.16. *Top panel*: IRAS F05189-2524 nuclear spectrum (black curve), extracted from a circular aperture with $r < 0.4''$. The corresponding pPXF best-fit model profile is shown in orange. The continuum-subtracted spectrum (blue curve) is obtained subtracting the best-fit pPXF model from the original spectrum. The vertical blue lines mark the wavelengths of the emission lines detected in the spectrum; the vertical green lines mark the position of stellar absorption systems (i.e. from left to right: MgI triplet, NaID and KI doublets, CaII triplet). The region excluded from the pPXF fit and corresponding to the most intense sky line residuals are highlighted as orange shaded areas; the portions of the spectra around 5700Å are missing, because of a filter blocking the laser contamination. The inset in the top panel shows the red stellar continuum emission map in the vicinity of the nuclear regions, with HST/F160W contours as in Fig. C.13; the nuclear position is shown with a white marker. *Bottom insets*: Multi-component best-fit analysis results for the main emission (Hβ and [OIII], left; Hα, [NII] and [SII], right) and absorption (NaID, centre) line features. NaID multi-component best-fit curves required to reproduce the cool, neutral absorption are superimposed on the observed spectrum (black curve); emission components are shifted downward for the sake of clarity.

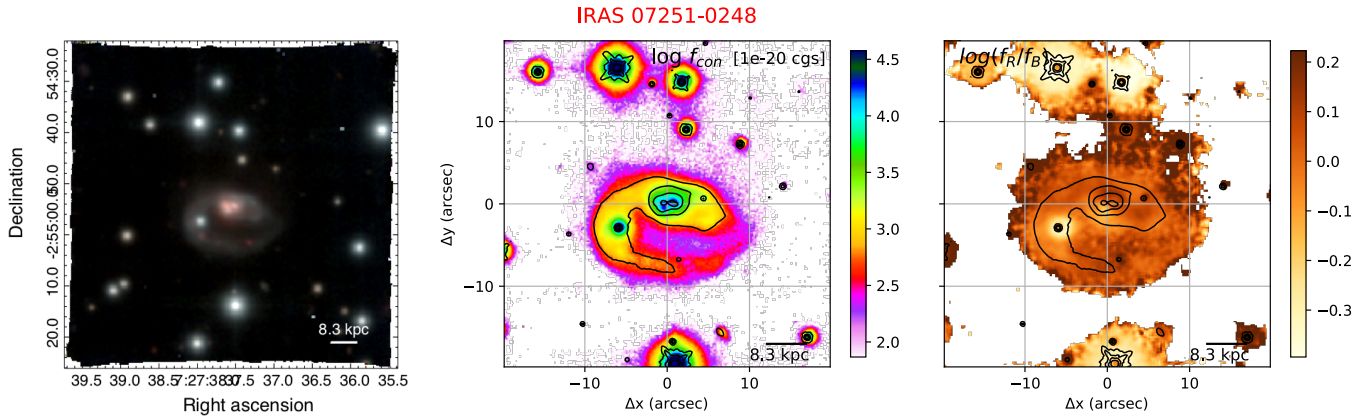

Fig. C.17. IRAS 07251-0248 images from MUSE observations with TOT = 2.55 hr. *Left*: colour composite optical image, showing [OIII] (green, from the wavelength range 4995 – 5020Å rest-frame), Hα (red, 6554 – 6575Å) and stellar continuum (blue, 4430 – 4540Å). *Centre*: red (7440 – 7550Å) continuum image from MUSE, with contours from HST/F160W. *Right*: continuum colour map obtained from MUSE, by dividing the red continuum image (central panel) from a blue image obtained collapsing the stellar emission in the range 4430−4540Å; contours from HST/F160W.

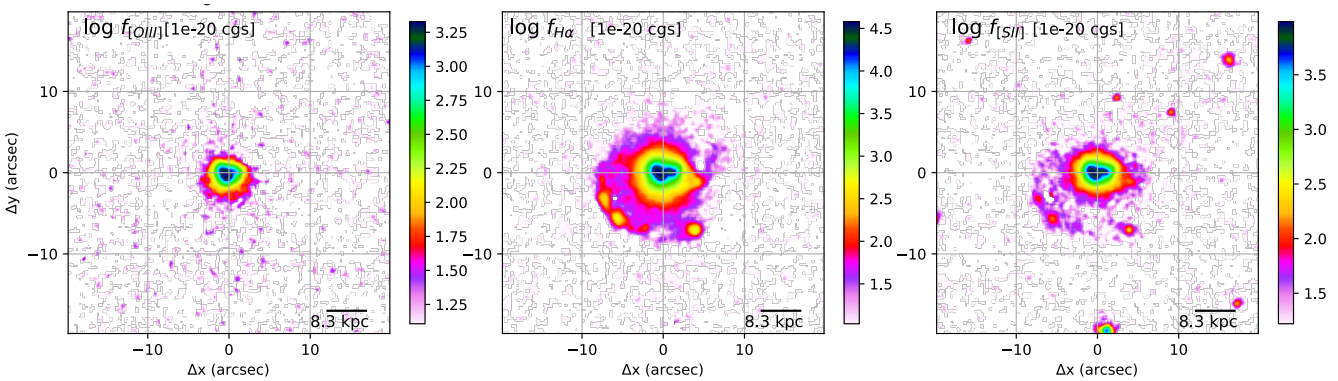

Fig. C.18. IRAS 07251-0248 emission lines images from MUSE observations. [OIII] (left, from the wavelength range 4995 – 5020Å rest-frame), Hα (centre, 6554 – 6575Å) and [SII] (right, 6704 – 6746Å) images have been obtained subtracting continuum emission using the adjacent regions at shorter and longer wavelengths with respect to the emission line systemics.

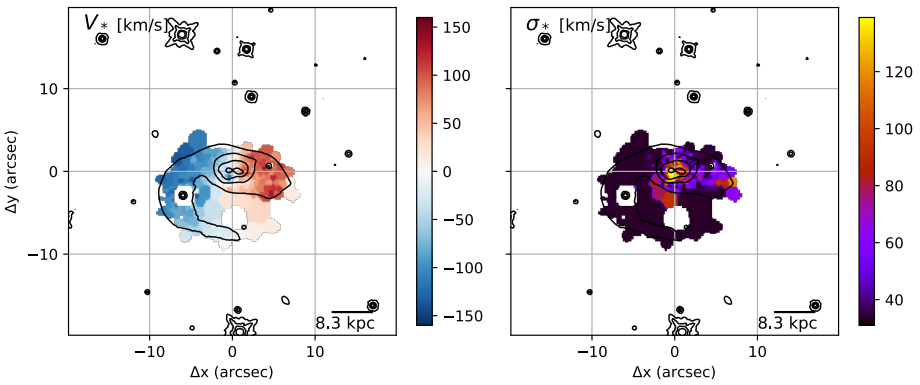

Fig. C.19. IRAS 07251-0248 stellar kinematic maps from pPXF analysis, with contours from HST/F160W. The left panel shows the stellar velocity V_*, while the right one represent the velocity dispersion σ_*.

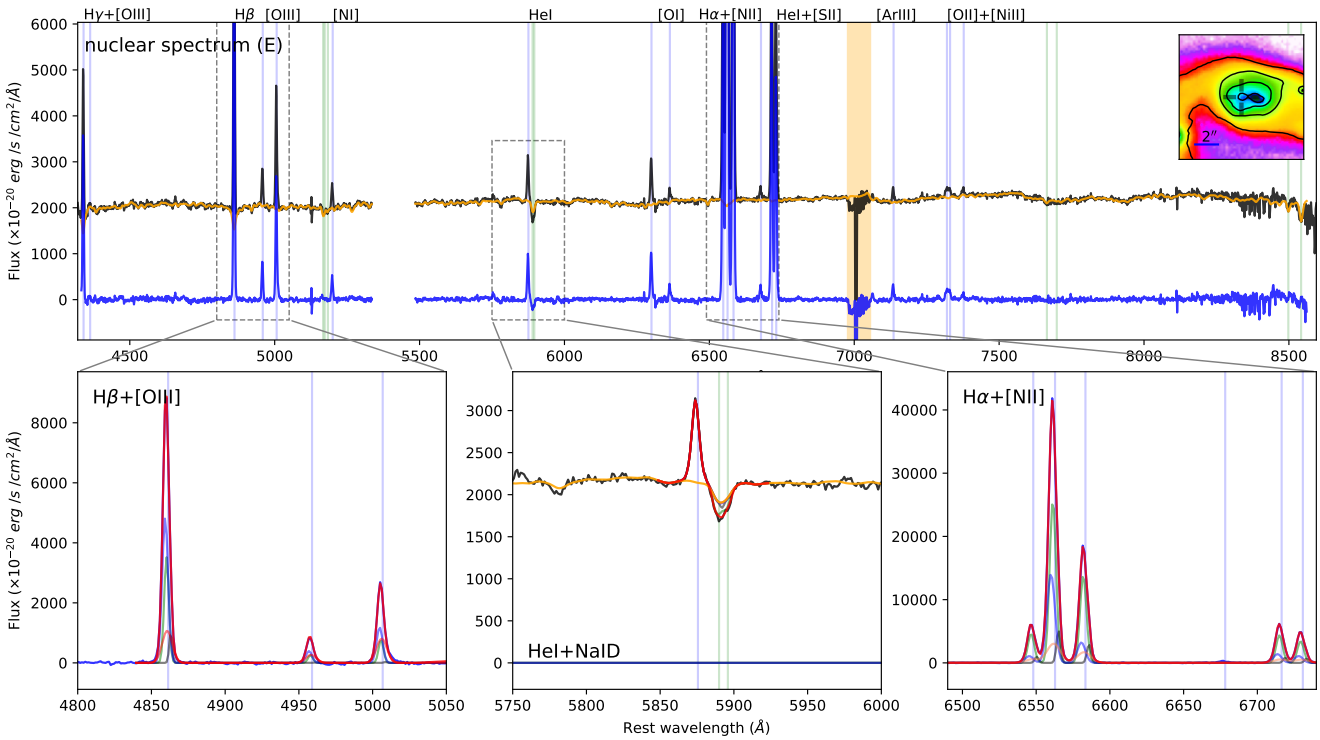

Fig. C.20. IRAS 07251-0248 E nuclear spectrum, extracted from a circular aperture with $r < 0.4''$, with the corresponding pPXF (top panel) and multi-component (bottom insets) best-fit models. See Fig. C.4 for details.

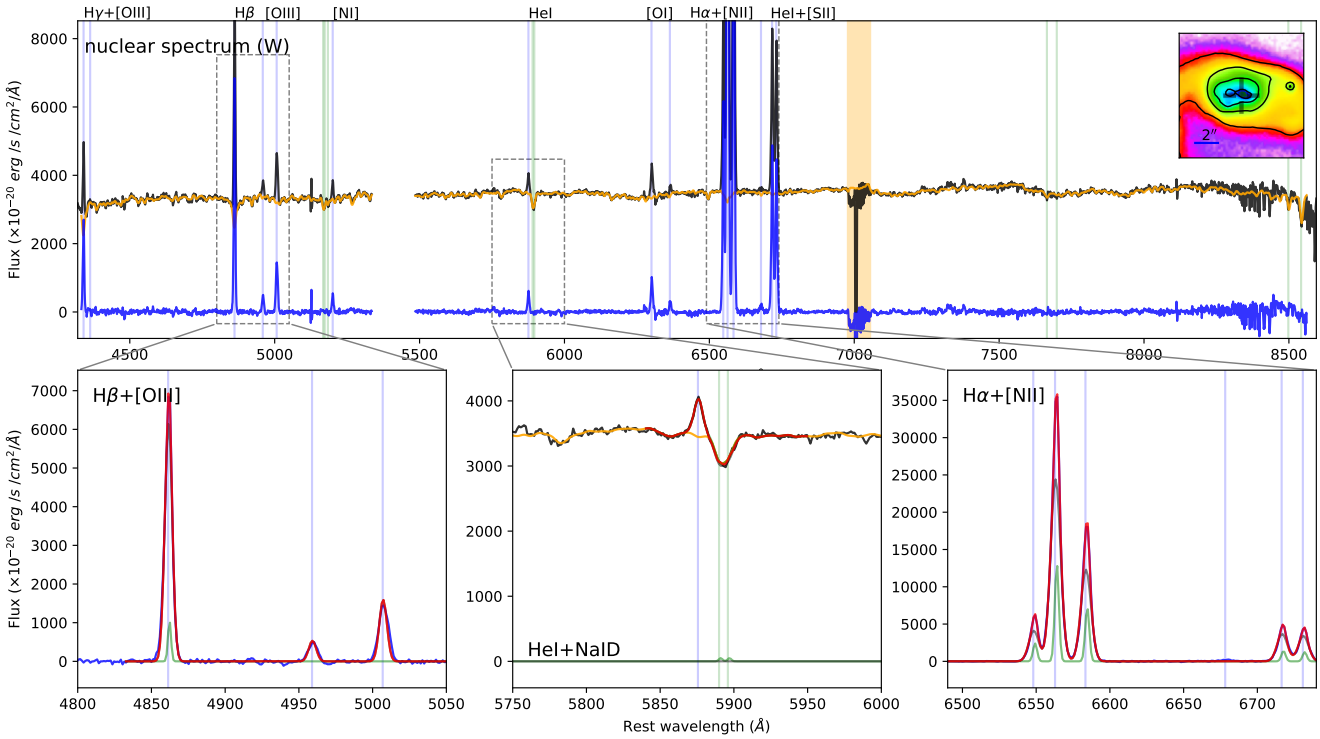

Fig. C.21. IRAS 07251-0248 W nuclear spectrum, extracted from a circular aperture with $r < 0.4''$, with the corresponding pPXF (top panel) and multi-component (bottom insets) best-fit models. See Fig. C.4 for details.

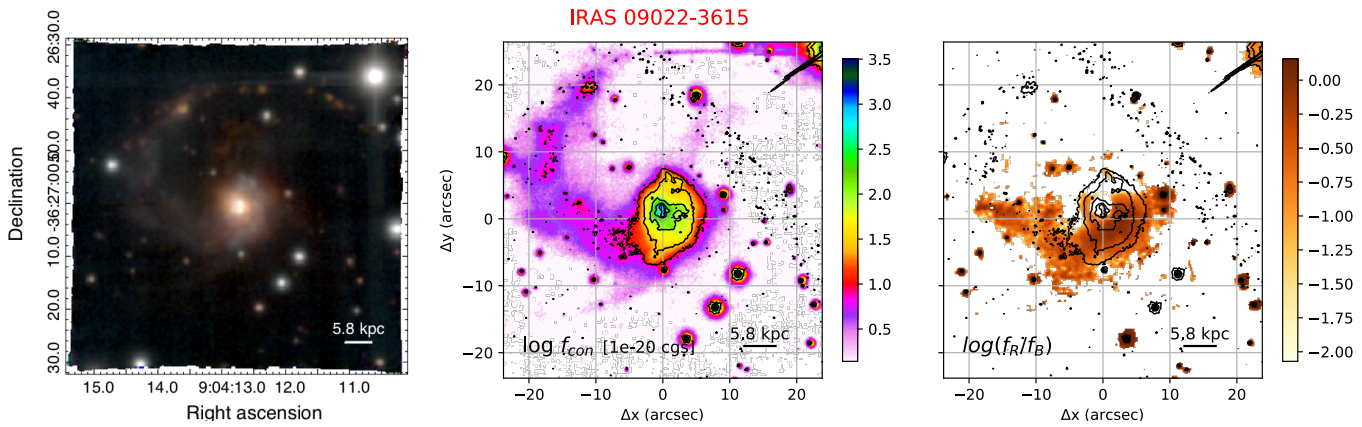

Fig. C.22. IRAS 09022-3615 images from MUSE observations with TOT = 2.04 hr. *Left*: colour composite optical image, showing [OIII] (green, from the wavelength range 4995 – 5020Å rest-frame), Hα (red, 6552 – 6574Å) and stellar continuum (blue, 4550 – 4710Å). *Centre*: red (7600 – 7760Å) stellar continuum image from MUSE , with contours from HST/F814W. *Right*: stellar continuum colour map obtained from MUSE, by dividing the red continuum image (central panel) by a blue image obtained collapsing the stellar emission in the range 4550 – 4710Å; contours from HST/F814W.

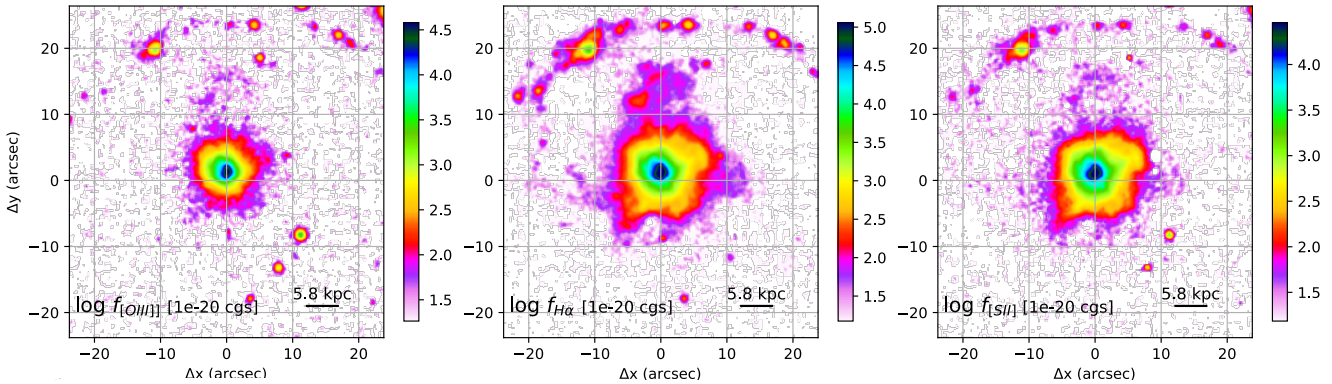

Fig. C.23. IRAS 09022-3615 emission lines images from MUSE observations. [OIII] (left, from the wavelength range 4995 – 5020Å rest-frame), Hα (centre, 6552 – 6574Å) and [SII] (right, 6700 – 6748Å) images have been obtained subtracting continuum emission using the adjacent regions at shorter and longer wavelengths with respect to the emission line systemics.

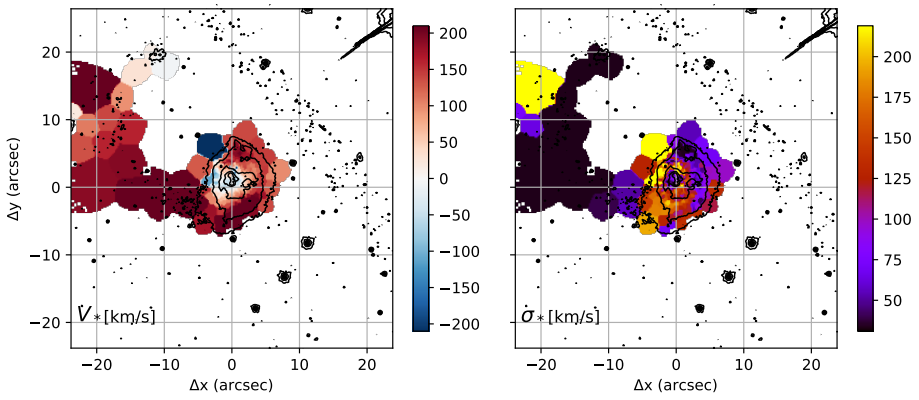

Fig. C.24. IRAS 09022-3615 stellar kinematic maps from pPXF analysis, with contours from HST/F814W. The left panel shows the stellar velocity V_*, while the right one represents the velocity dispersion σ_*.

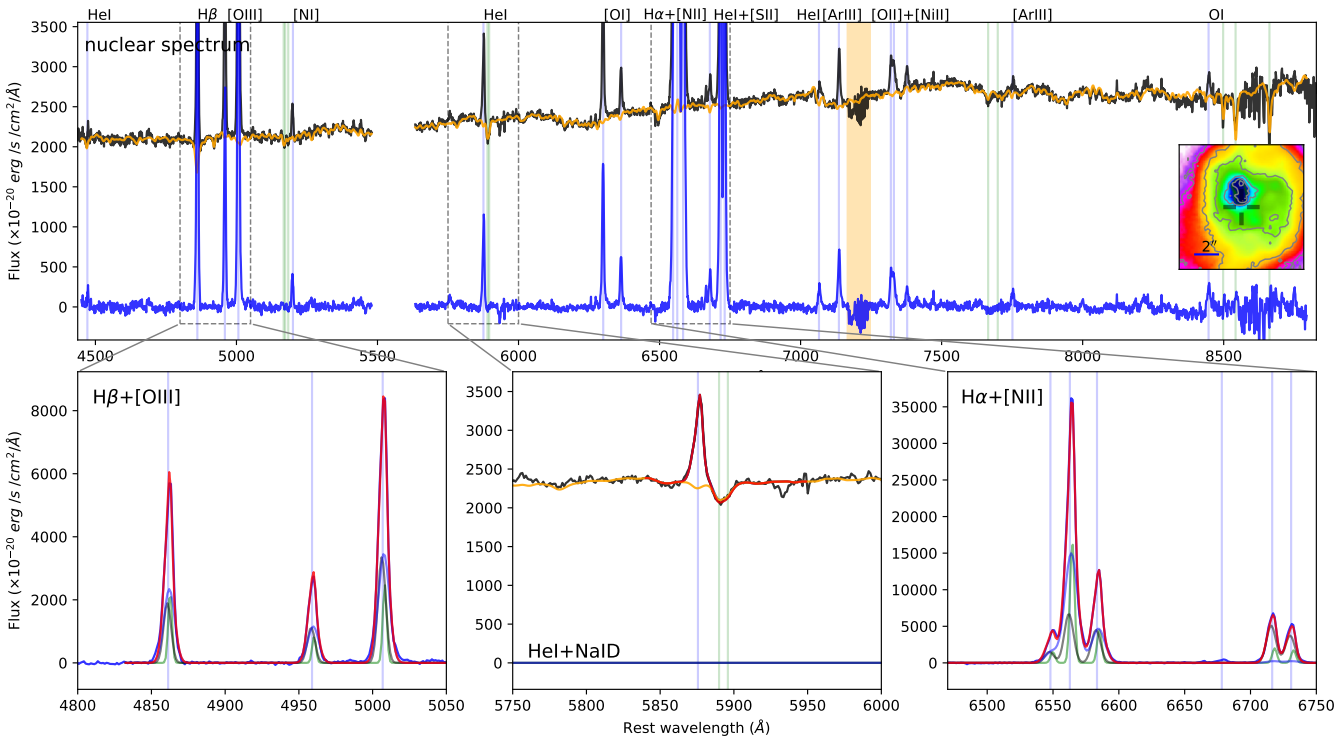

Fig. C.25. IRAS 09022 nuclear spectrum, extracted from a circular aperture with $r < 0.4''$, with the corresponding pPXF (top panel) and multi-component (bottom insets) best-fit models. See Fig. C.4 for details.

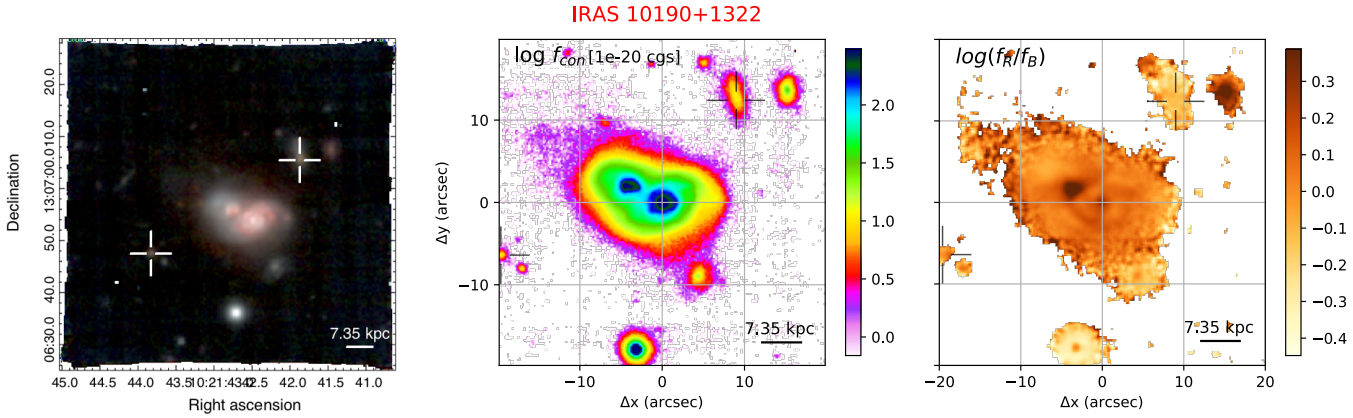

Fig. C.26. IRAS 10190+1322 images from MUSE observations with TOT = 2.04 hr. *Left*: colour composite optical image, showing [OIII] (green, from the wavelength range 4988 – 5022Å rest-frame), Hα (red, 6556 – 6572Å) and stellar continuum (blue, 4460 – 4570Å). *Centre*: red (7440 – 7560Å) stellar continuum image from MUSE , with contours from HST/F160W. *Right*: stellar continuum colour map obtained from MUSE, by dividing the red continuum image (central panel) by a blue image obtained collapsing the stellar emission in the range 4460 – 4570Å. In all panels, we display the two companion galaxies of IRAS 10190+1322 with cross markers.

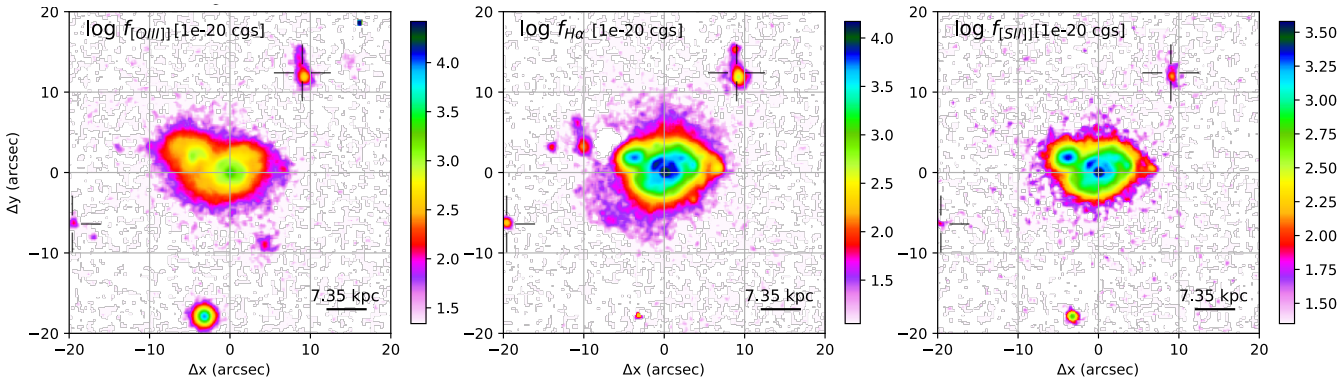

Fig. C.27. IRAS 10190+1322 emission lines images from MUSE observations. [OIII] (left, from the wavelength range 4988 – 5022Å rest-frame), Hα (centre, 6556 – 6572Å) and [SII] (right, 6704 – 6747Å) images have been obtained subtracting continuum emission using the adjacent regions at shorter and longer wavelengths with respect to the emission line systemics.

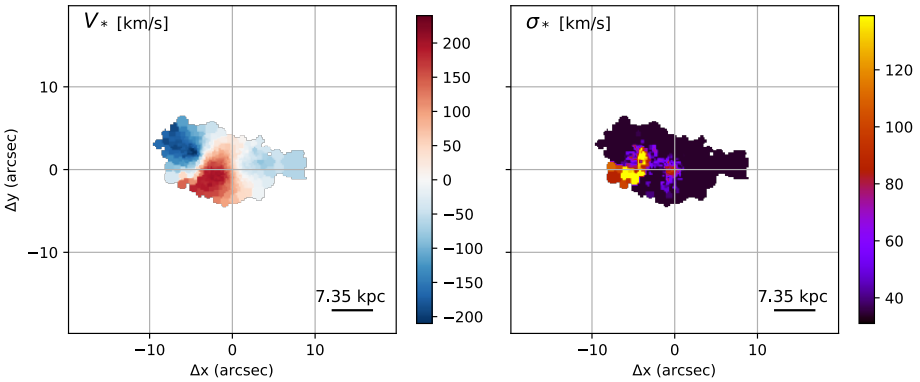

Fig. C.28. IRAS 10190+1322 stellar kinematic maps from pPXF analysis. The left panel shows the stellar velocity V_*, while the right one represents the velocity dispersion σ_*.

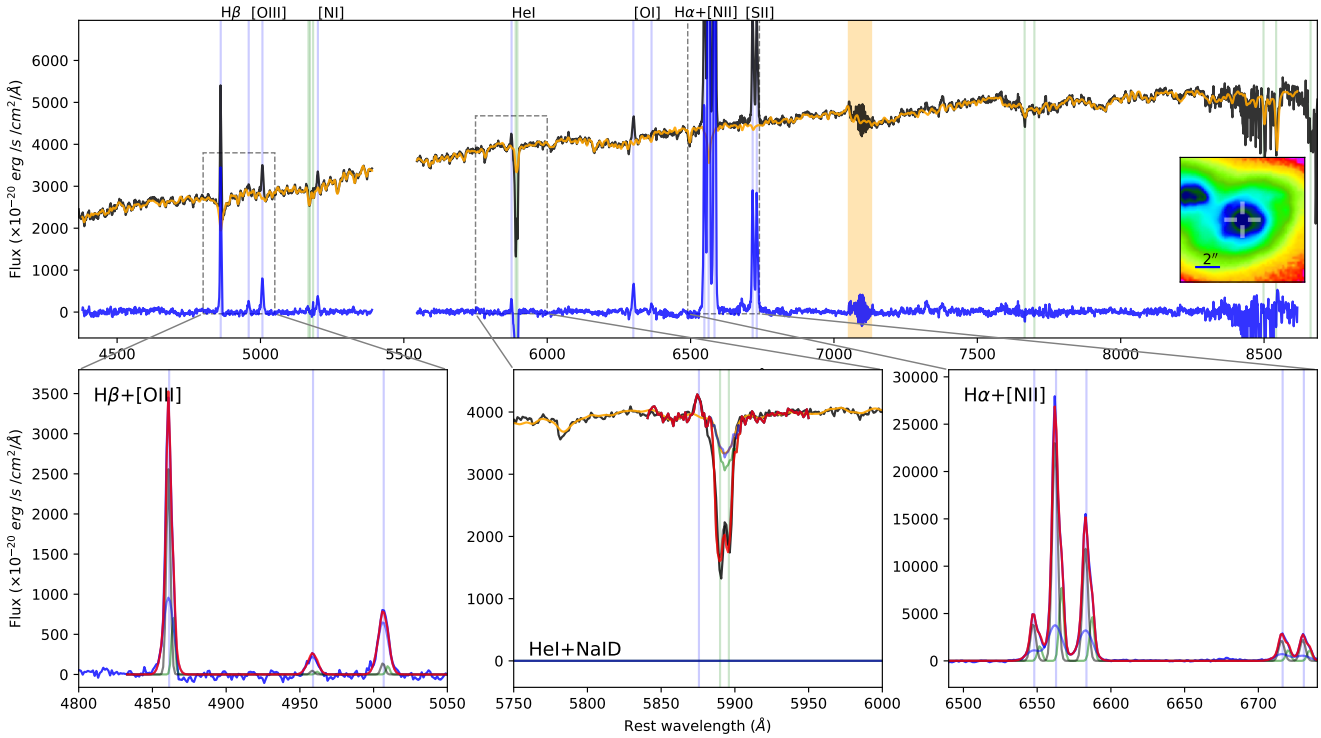

Fig. C.29. IRAS 10190+1322 W nuclear spectrum, extracted from a circular aperture with $r < 0.4''$, with the corresponding pPXF (top panel) and multi-component (bottom insets) best-fit models. See Fig. C.4 for details.

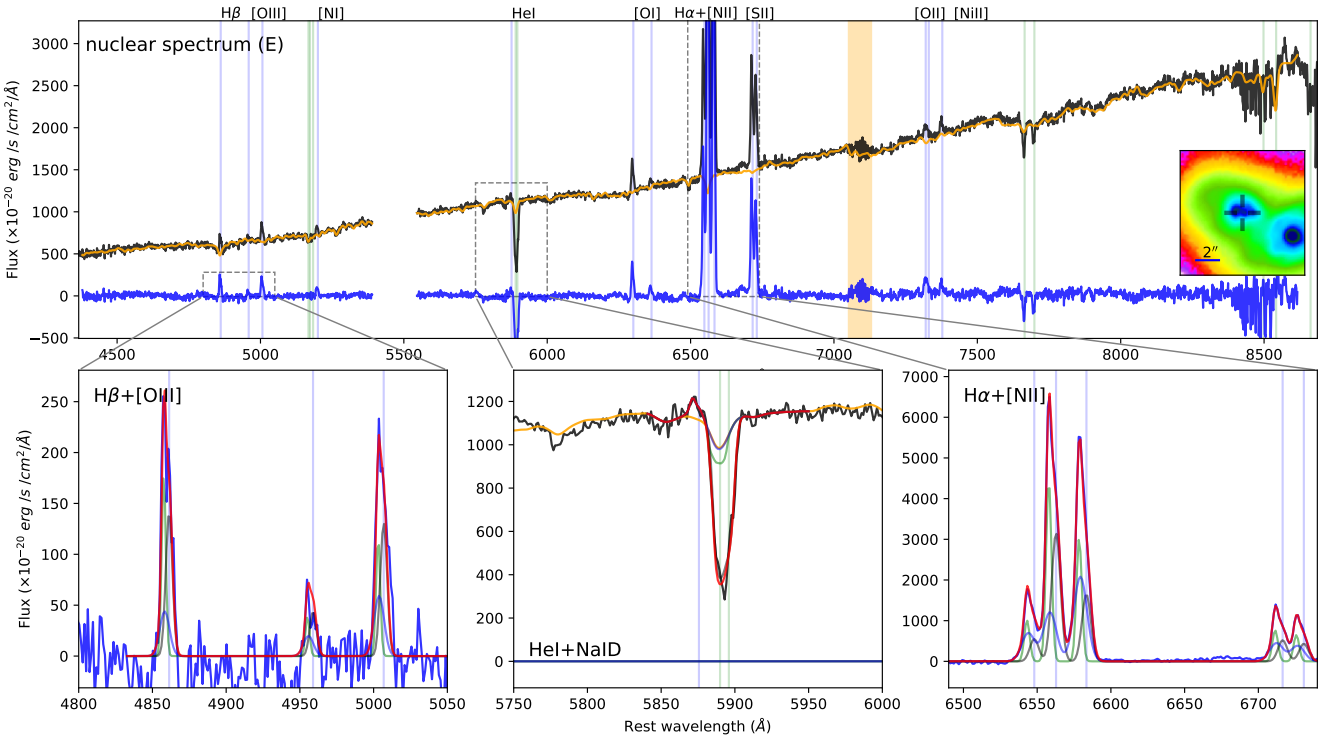

Fig. C.30. IRAS 10190+1322 E nuclear spectrum, extracted from a circular aperture with $r < 0.4''$, with the corresponding pPXF (top panel) and multi-component (bottom insets) best-fit models. See Fig. C.4 for details.

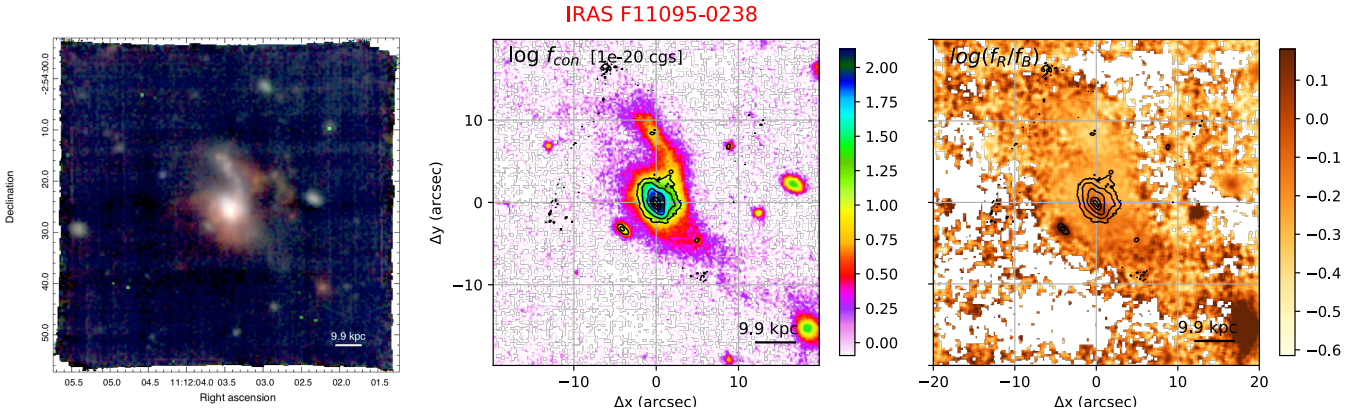

Fig. C.31. IRAS F11095-0238 images from MUSE observations with TOT = 2.72 hr. *Left*: colour composite optical image, showing [OIII] (green, from the wavelength range 4975 – 5032Å rest-frame), Hα (red, 6549 – 6576Å) and continuum (blue, 4410 – 4490Å). *Centre*: red (7690 – 7760Å) continuum image from MUSE, with contours from HST/F160W. *Right*: continuum colour map obtained from MUSE, by dividing the red continuum image (central panel) by a blue image obtained collapsing the stellar emission in the range 4410 – 4490Å; contours from HST/F160W.

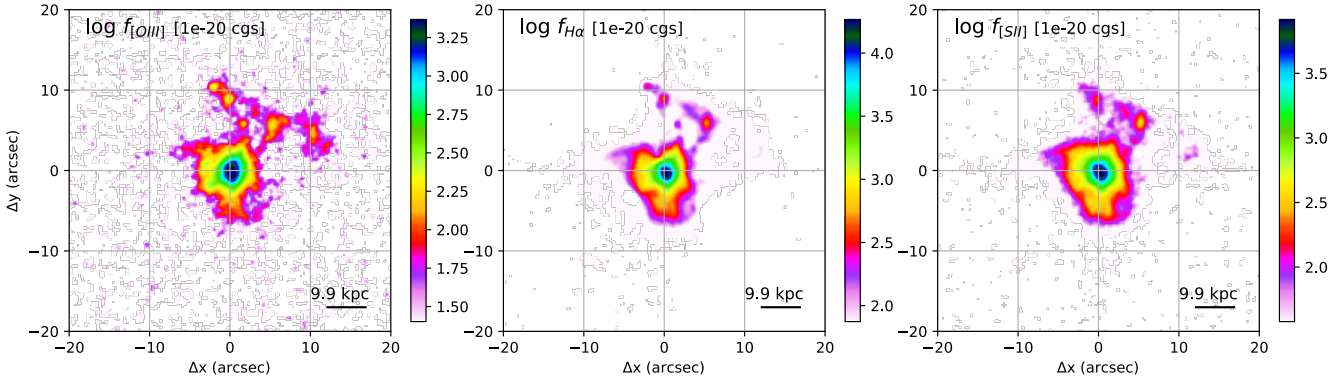

Fig. C.32. IRAS F11095-0238 emission lines images from MUSE observations. [OIII] (left, from the wavelength range 4975 – 5032Å rest-frame), Hα (centre, 6549 – 6576Å) and [SII] (right, 6695 – 6749Å) images have been obtained subtracting continuum emission using the adjacent regions at shorter and longer wavelengths with respect to the emission line systemics.

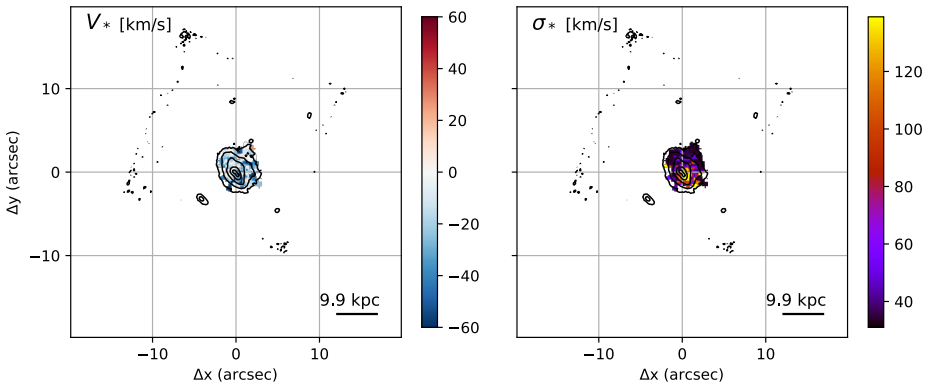

Fig. C.33. IRAS F11095-0238 stellar kinematic maps from pPXF analysis, with contours from HST/F160W. The left panel shows the stellar velocity V_*, while the right one represents the velocity dispersion σ_*.

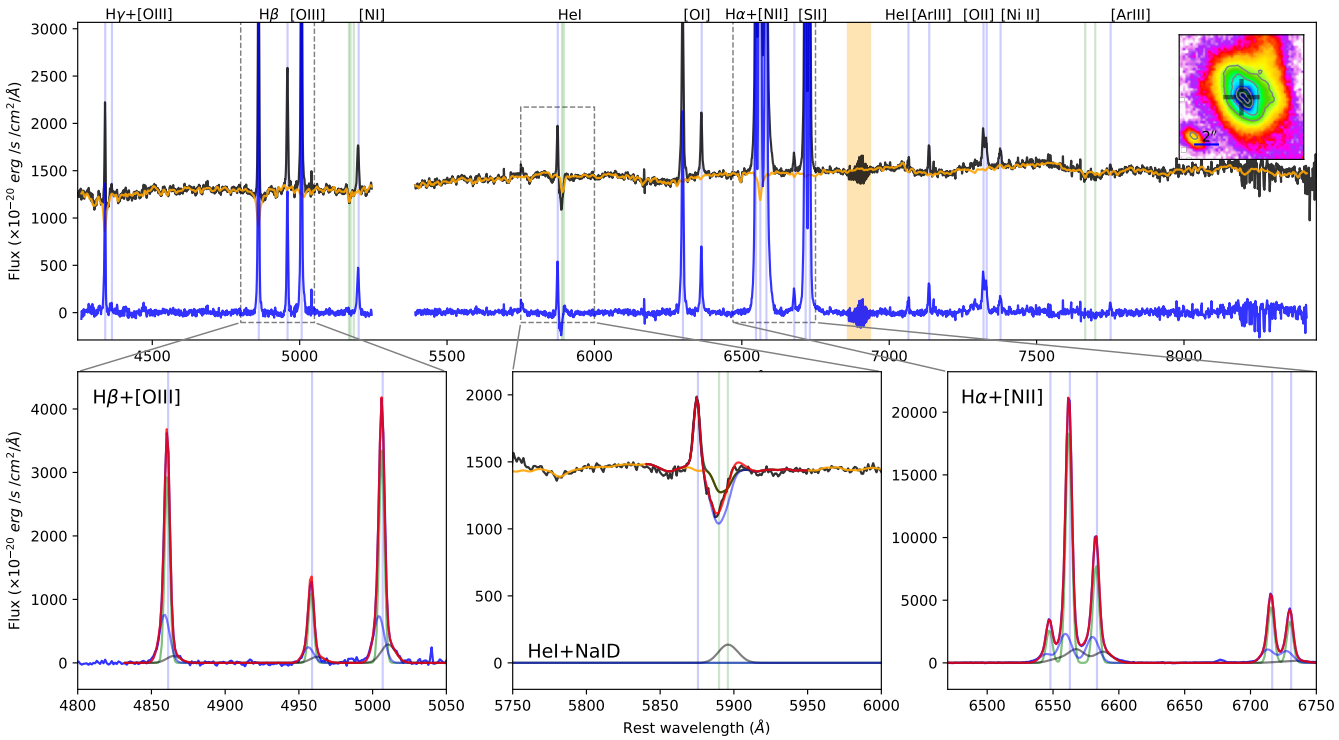

Fig. C.34. IRAS F11095-0238 NE nuclear spectrum, extracted from a circular aperture with $r < 0.4''$, with the corresponding pPXF (top panel) and multi-component (bottom insets) best-fit models. See Fig. C.4 for details.

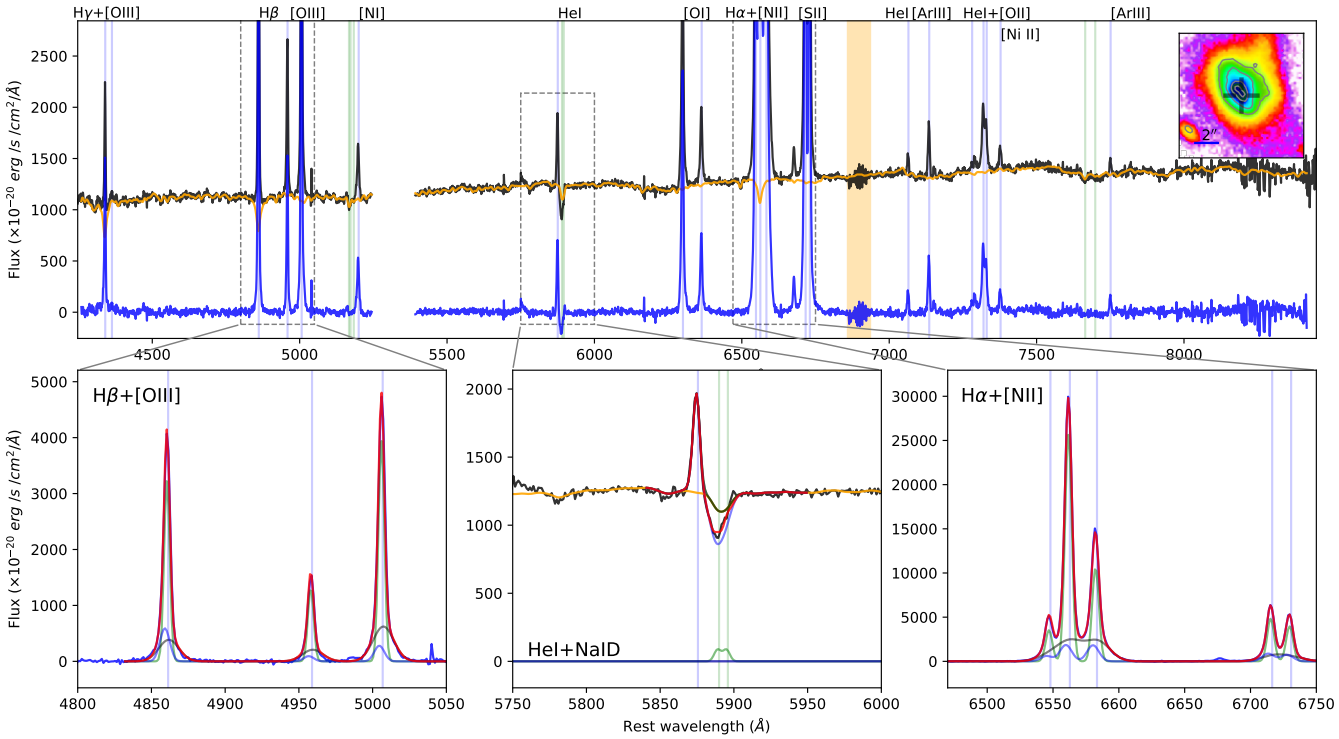

Fig. C.35. IRAS F11095-0238 SW nuclear spectrum, extracted from a circular aperture with $r < 0.4''$, with the corresponding pPXF (top panel) and multi-component (bottom insets) best-fit models. See Fig. C.4 for details.

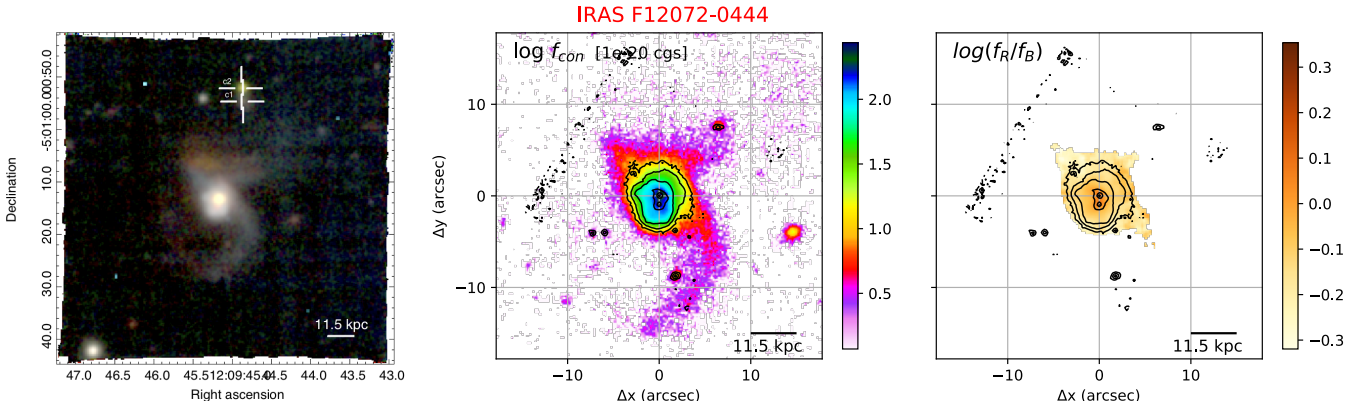

Fig. C.36. IRAS F12072-0444 images from MUSE observations with TOT = 0.68 hr. *Left*: colour composite optical image, showing [OIII] (green, from the wavelength range 4980 – 5020Å rest-frame), Hα (red, 6553 – 6576Å) and continuum (blue, 4550 – 4650Å). *Centre*: red (7540 – 7610Å) continuum image from MUSE, with contours from HST/F160W. *Right*: continuum colour map obtained from MUSE, by dividing the red continuum image (central panel) by a blue image obtained collapsing the stellar emission in the range 4550 – 4650Å; contours from HST/F160W. In the first panel, we display the IRAS F12072-0444 companion galaxies with cross markers.

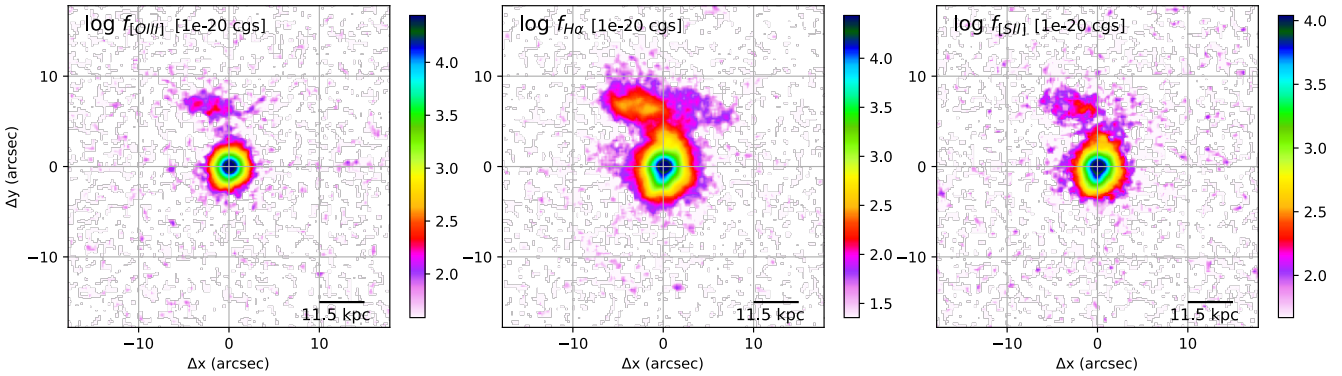

Fig. C.37. IRAS F12072-0444 emission lines images from MUSE observations. [OIII] (left, from the wavelength range 4980 – 5020Å rest-frame), Hα (centre, 6553 – 6576Å) and [SII] (right, 6695 – 6747Å) images have been obtained subtracting continuum emission using the adjacent regions at shorter and longer wavelengths with respect to the emission line systemics.

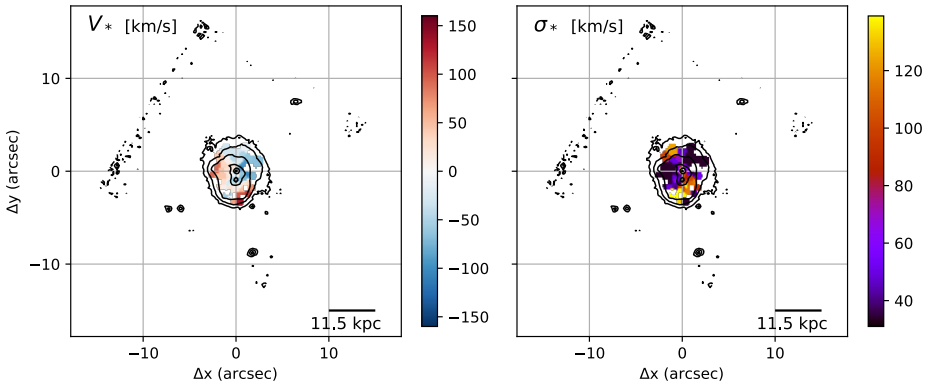

Fig. C.38. IRAS F12072-0444 stellar kinematic maps from pPXF analysis, with contours from HST/F160W. The left panel shows the stellar velocity V_*, while the right one represents the velocity dispersion σ_*.

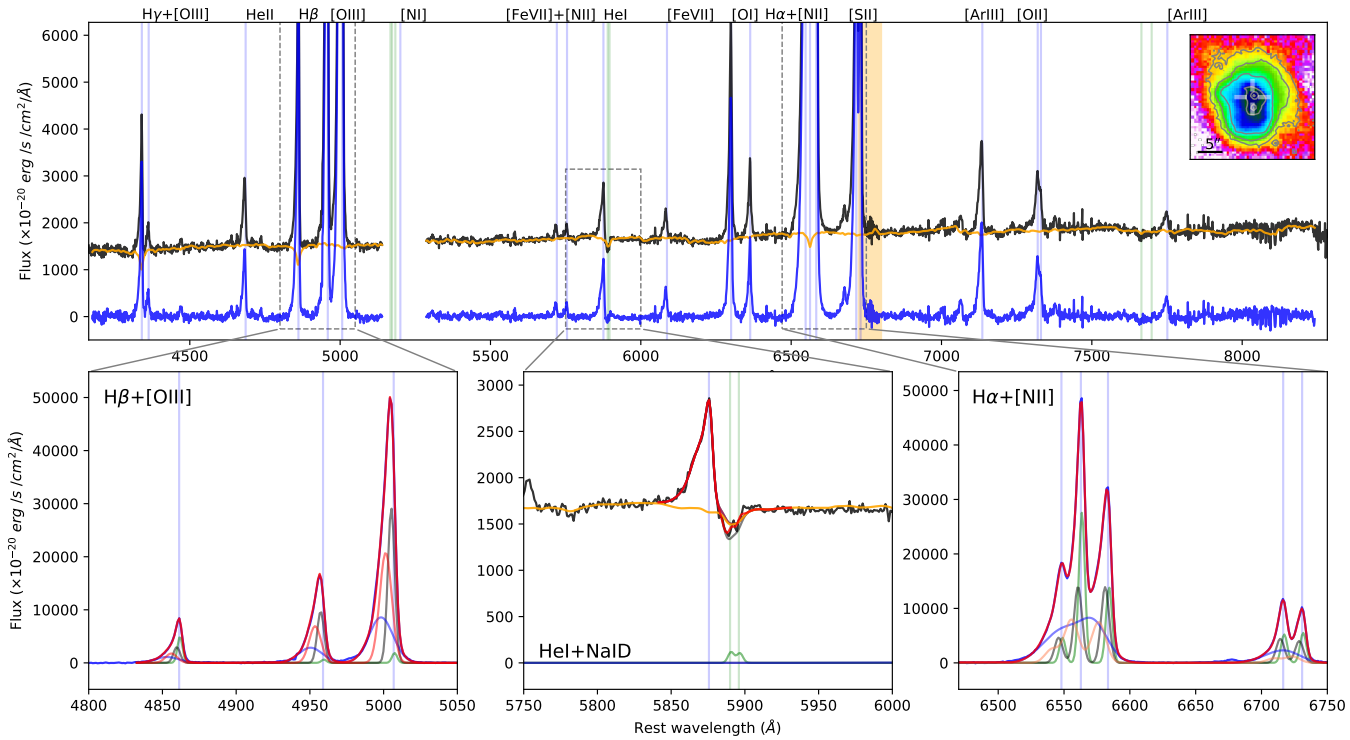

Fig. C.39. IRAS F12072-0444 NE nuclear spectrum, extracted from a circular aperture with $r < 0.4''$, with the corresponding pPXF (top panel) and multi-component (bottom insets) best-fit models. See Fig. C.4 for details.

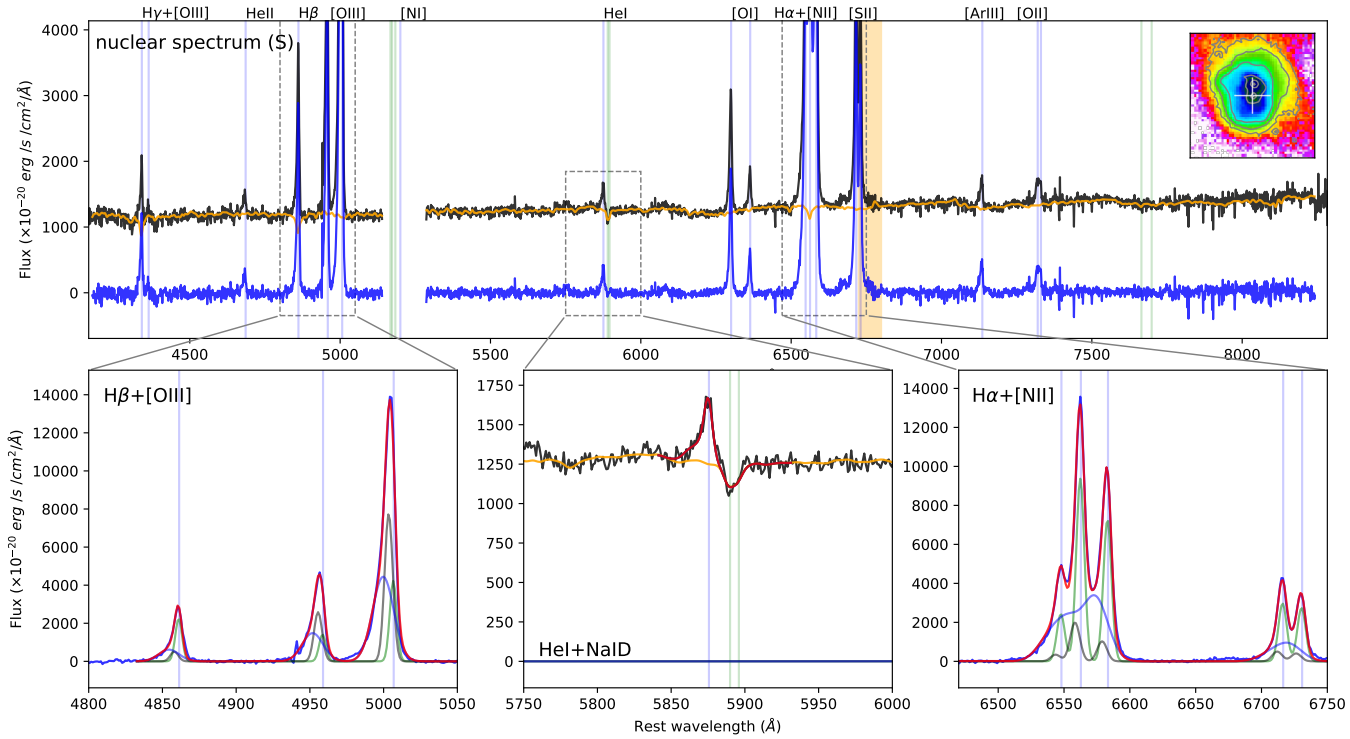

Fig. C.40. IRAS F12072-0444 SW nuclear spectrum, extracted from a circular aperture with $r < 0.4''$, with the corresponding pPXF (top panel) and multi-component (bottom insets) best-fit models. See Fig. C.4 for details.

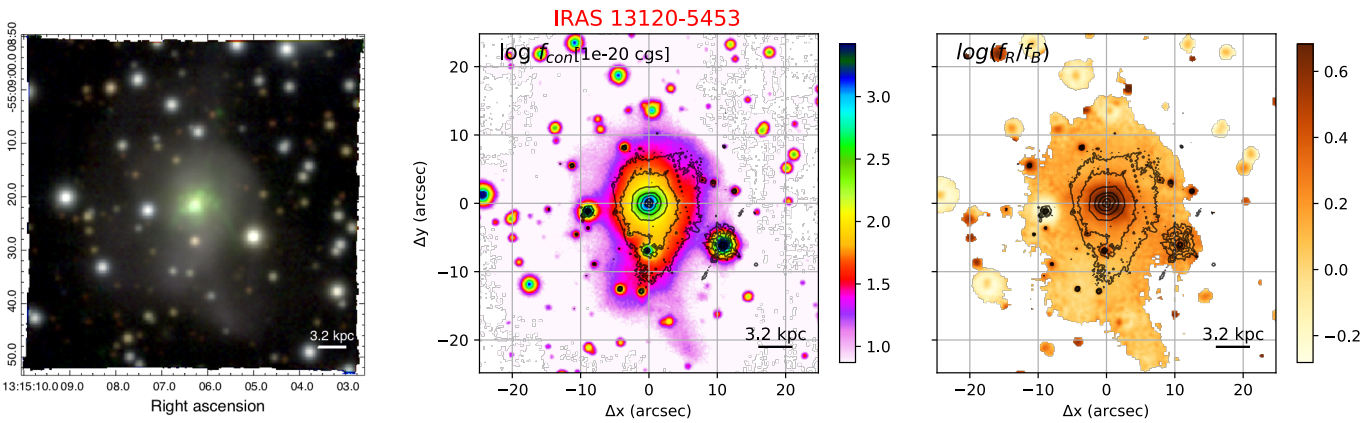

Fig. C.41. IRAS 13120-5453 images from MUSE observations with TOT = 0.52 hr. *Left*: colour composite optical image, showing [OIII] (green, from the wavelength range 4980 – 5014Å rest-frame), Hα (red, 6555 – 6572Å) and continuum (blue, 4600 – 4700Å). *Centre*: red (7500 – 7600Å) continuum image from MUSE , with contours from HST/F160W. *Right*: continuum colour map obtained from MUSE, by dividing the red continuum image (central panel) by a blue image obtained collapsing the stellar emission in the range 4600 – 4700Å; contours from HST/F160W.

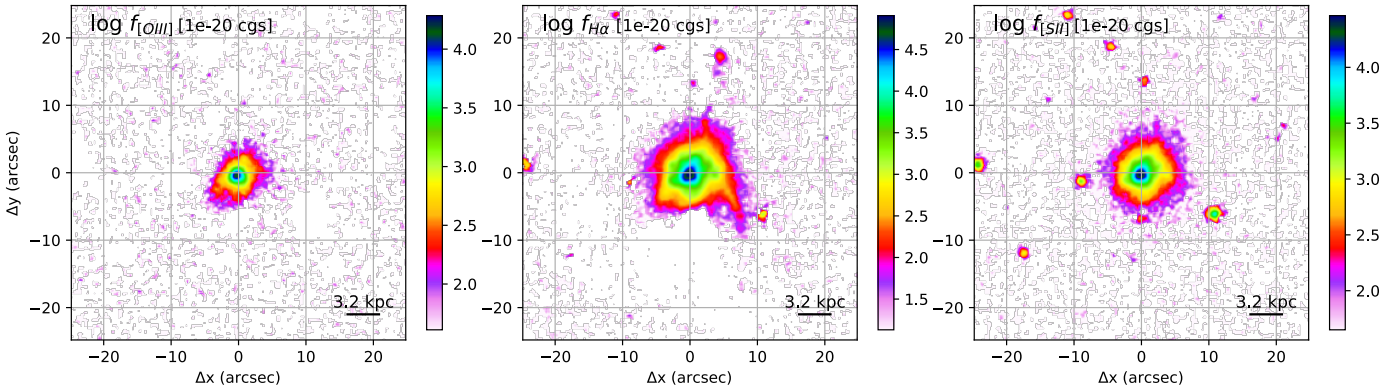

Fig. C.42. IRAS 13120-5453 emission lines images from MUSE observations. [OIII] (left, from the wavelength range 4980 – 5014Å rest-frame), Hα (centre, 6555 – 6572Å) and [SII] (right, 6694 – 6746Å) images have been obtained subtracting continuum emission using the adjacent regions at shorter and longer wavelengths with respect to the emission line systemics. In all panels, we display the position of the companion galaxy with a cross marker.

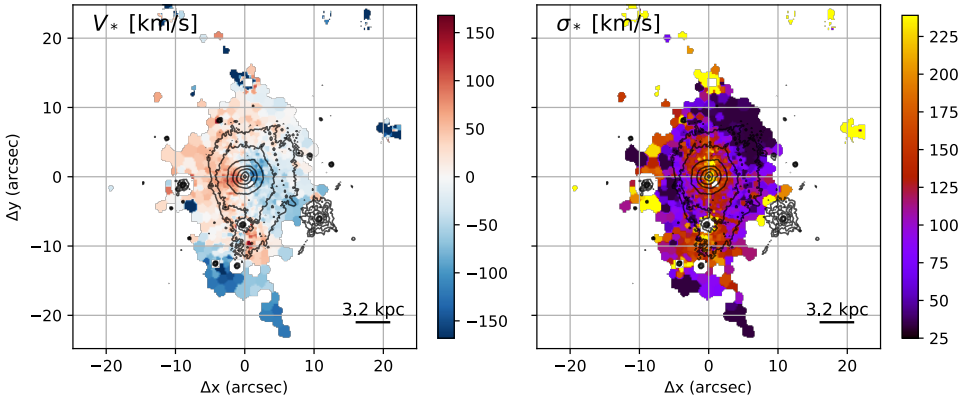

Fig. C.43. IRAS 13120-5453 stellar kinematic maps from pPXF analysis, with contours from HST/F160W. The left panel shows the stellar velocity V_*, while the right one represents the velocity dispersion σ_*. The inner 3.5 kpc may indicate a low amplitude rotational pattern; in the outside regions there are more irregular kinematics.

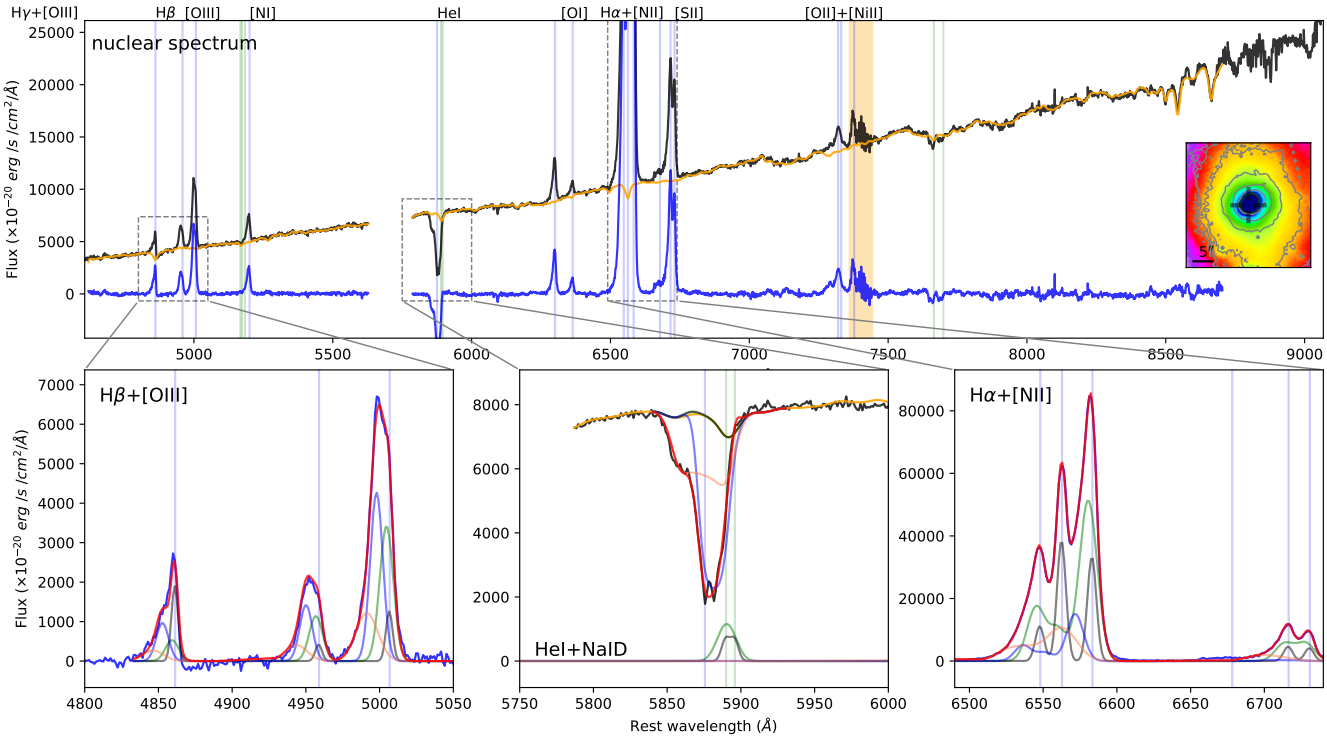

Fig. C.44. IRAS 13120-5453 nuclear spectrum, extracted from a circular aperture with $r < 0.4''$, with the corresponding pPXF (top panel) and multi-component (bottom insets) best-fit models. See Fig. C.4 for details.

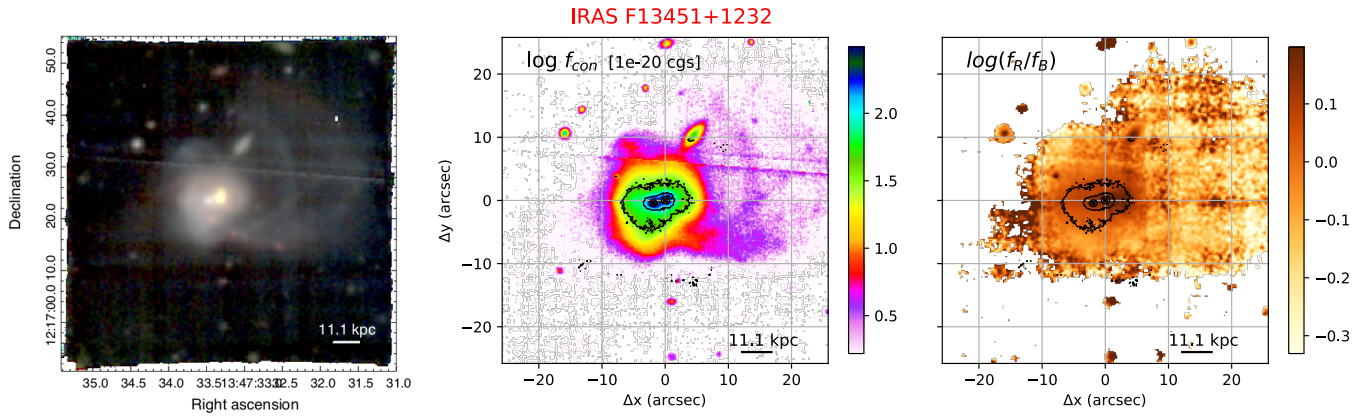

Fig. C.45. IRAS F13451+1232 images from MUSE observations with TOT = 2.04 hr. *Left*: colour composite optical image, showing [OIII] (green, from the wavelength range 4975 – 5047Å rest-frame), Hα (red, 6554 – 6576Å) and stellar continuum (blue, 4410 – 4490Å). *Centre*: red (7590 – 7665Å) continuum image from MUSE, with contours from HST/F160W. *Right*: continuum colour map obtained from MUSE, by dividing the red continuum image (central panel) by a blue image obtained collapsing the stellar emission in the range 4410 – 4490Å; contours from HST/F160W. In all panels, the top part of the ULIRG shows an almost horizontal feature due to the removal of a satellite trail.

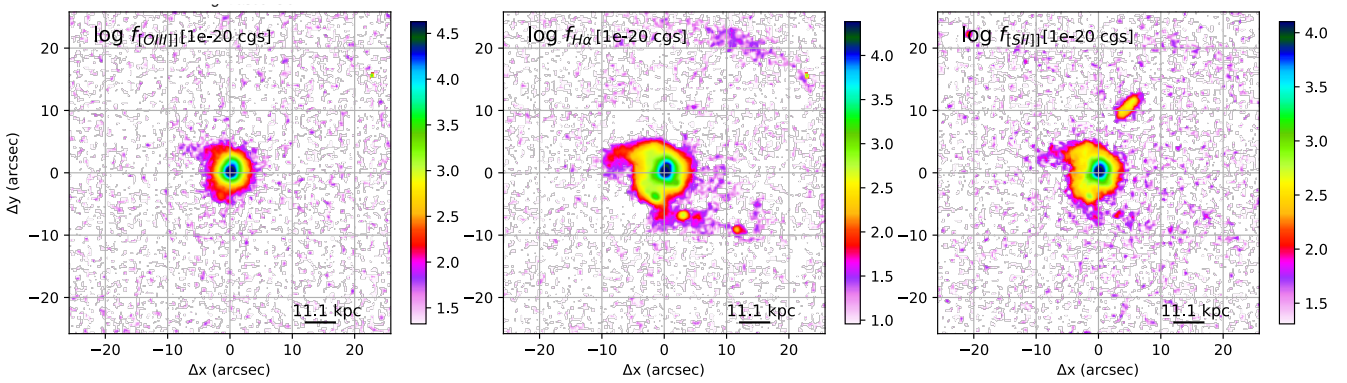

Fig. C.46. IRAS F13451+1232 emission lines images from MUSE observations. [OIII] (left, from the wavelength range 4975 – 5047Å rest-frame), Hα (centre, 6554 – 6576Å) and [SII] (right, 6662 – 6757Å) images have been obtained subtracting continuum emission using the adjacent regions at shorter and longer wavelengths with respect to the emission line systemics.

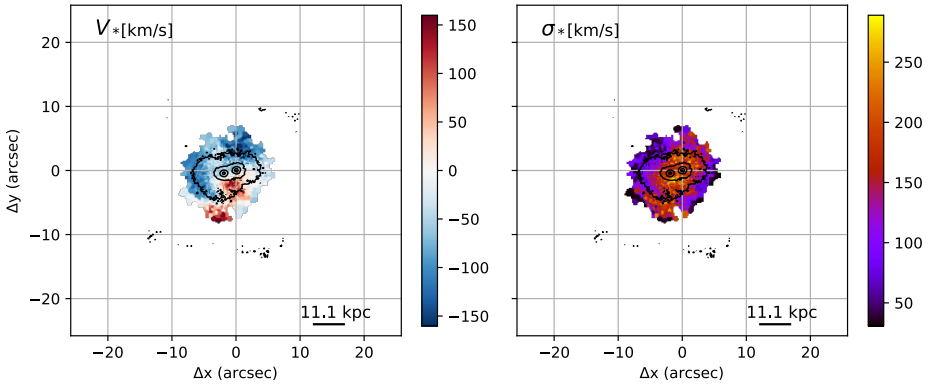

Fig. C.47. IRAS F13451+1232 stellar kinematic maps from pPXF analysis, with contours from HST/F160W. The left panel shows the stellar velocity V_*, while the right one represents the velocity dispersion σ_*.

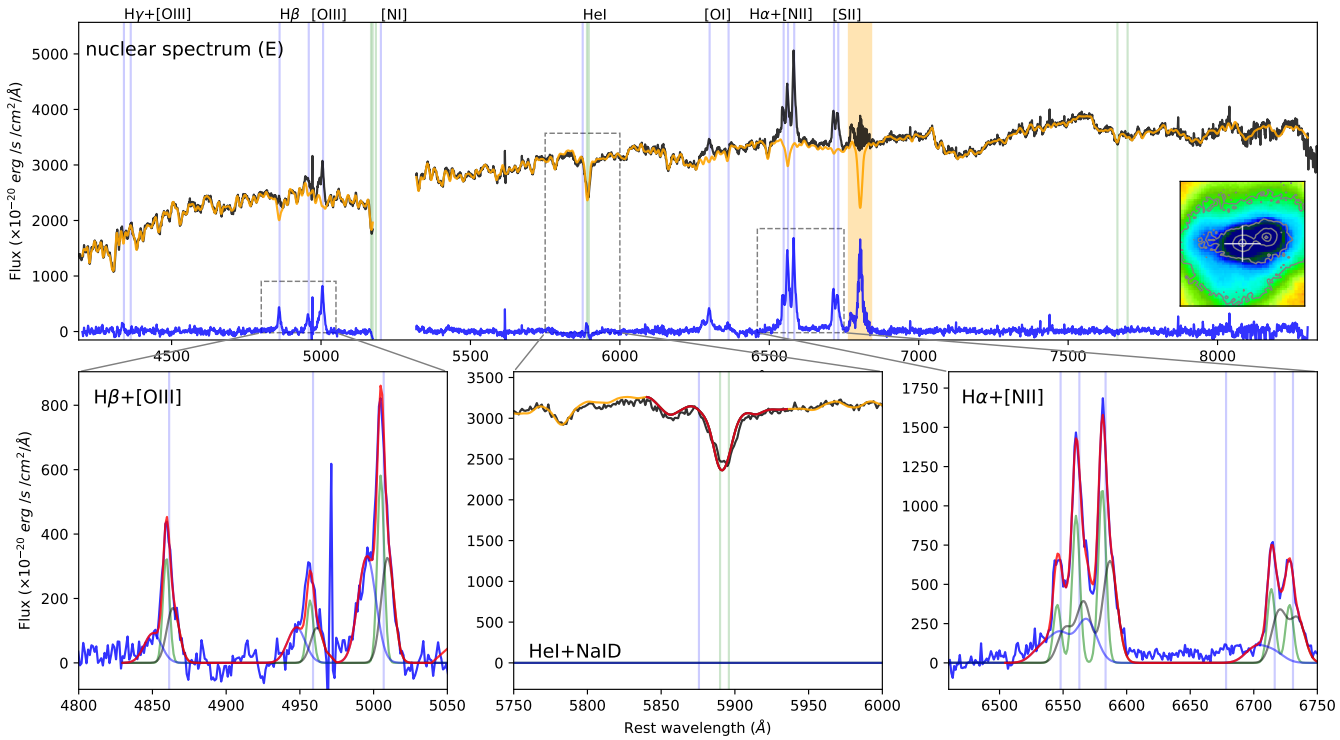

Fig. C.48. IRAS F13451+1232 E nuclear spectrum, extracted from a circular aperture with $r < 0.4''$, with the corresponding pPXF (top panel) and multi-component (bottom insets) best-fit models. See Fig. C.4 for details.

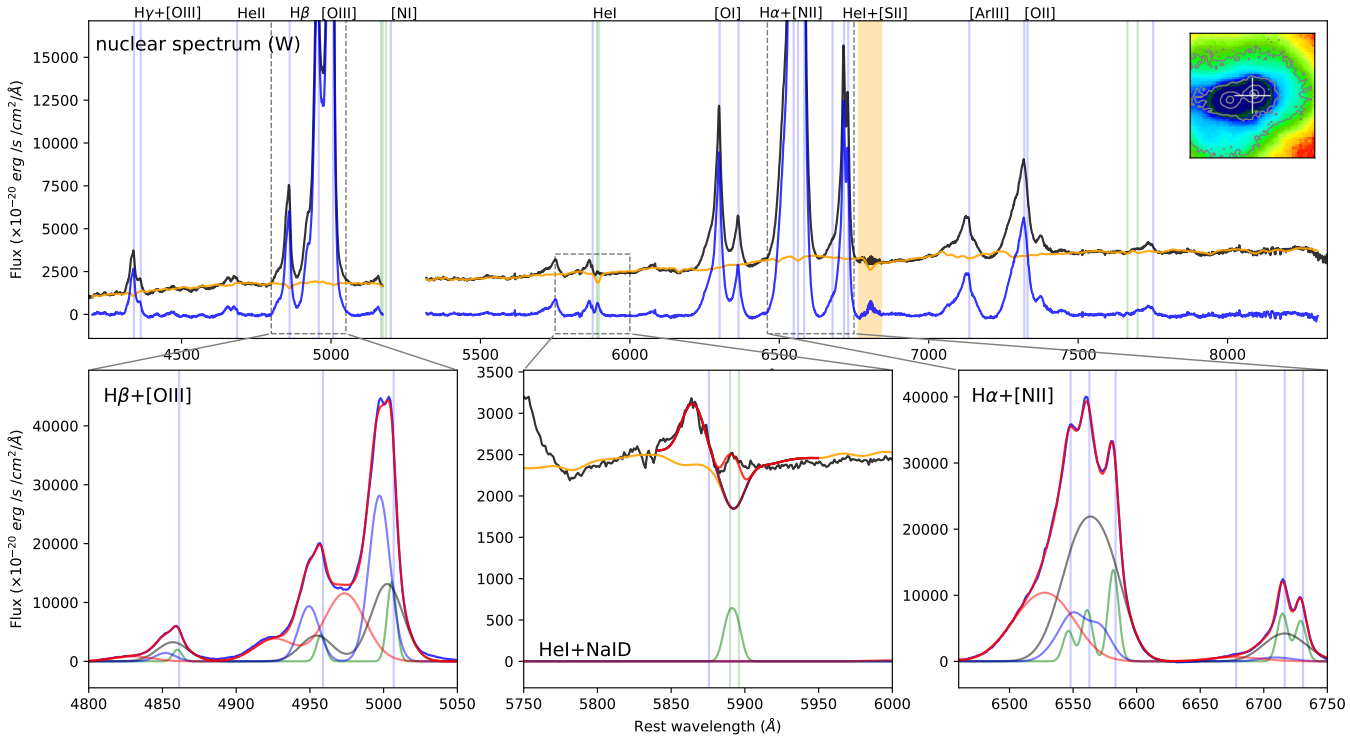

Fig. C.49. IRAS F13451+1232 W nuclear spectrum, extracted from a circular aperture with $r < 0.4''$, with the corresponding pPXF (top panel) and multi-component (bottom insets) best-fit models. See Fig. C.4 for details.

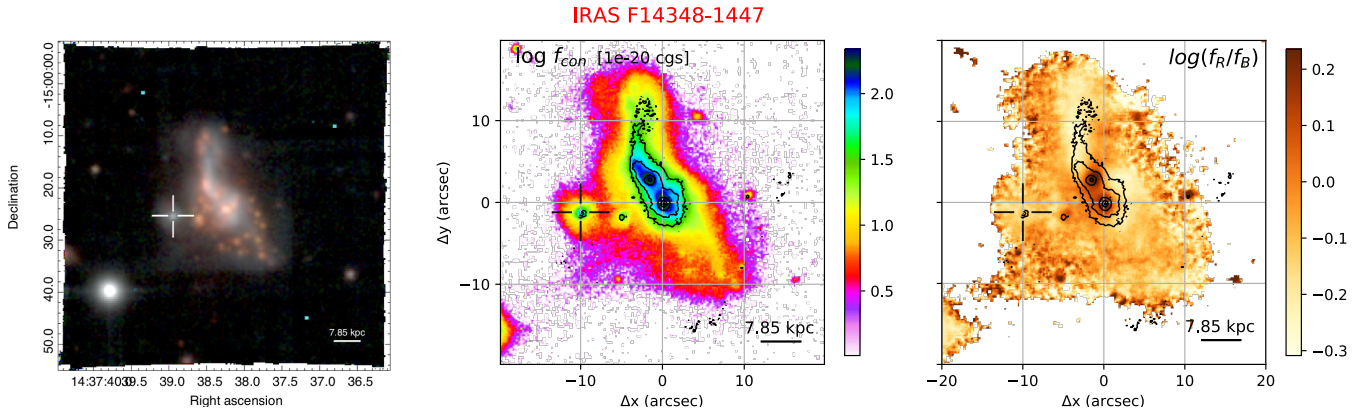

Fig. C.50. IRAS F14348-1447 images from MUSE observations with TOT = 0.68 hr. *Left*: colour composite optical image, showing [OIII] (green, from the wavelength range 4980 – 5020Å rest-frame), Hα (red, 6555 – 6575Å) and continuum (blue, 4590 – 4690Å). *Centre*: red (7890 – 8000Å) continuum image from MUSE , with contours from HST/F160W. *Right*: continuum colour map obtained from MUSE, by dividing the red continuum image (central panel) by a blue image obtained collapsing the stellar emission in the range 4590 – 4690Å; contours from HST/F160W. In all panels, we display the IRAS F14348-1447 companion galaxy with a cross marker.

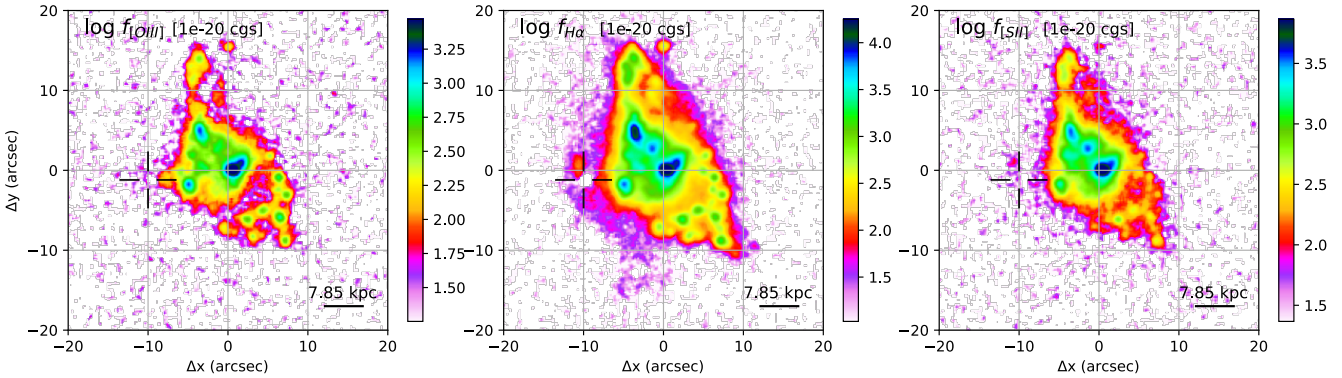

Fig. C.51. IRAS F14348-1447 emission lines images from MUSE observations. [OIII] (left, from the wavelength range 4980 – 5020Å rest-frame), Hα (centre, 6555 – 6575Å) and [SII] (right, 6686 – 6750Å) images have been obtained subtracting continuum emission using the adjacent regions at shorter and longer wavelengths with respect to the emission line systemics. In all panels, we display the position of the companion galaxy with a cross marker; the absence of line emission in the three maps is due to their faintness.

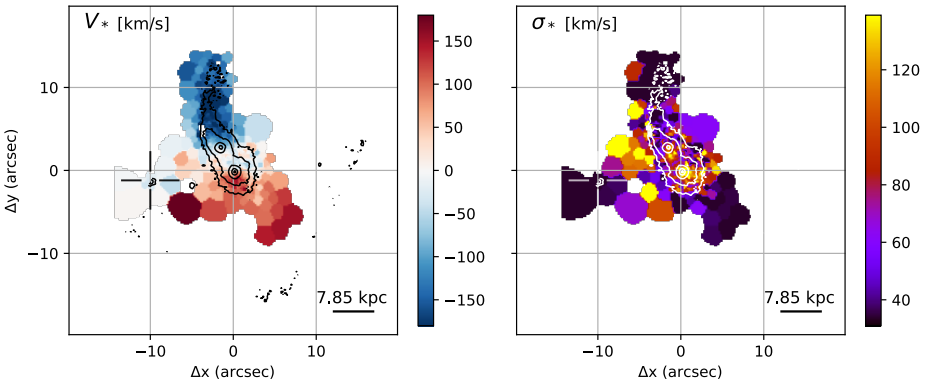

Fig. C.52. IRAS F14348-1447 stellar kinematic maps from pPXF analysis, with contours from HST/F160W. The left panel shows the stellar velocity V_*, while the right one represents the velocity dispersion σ_*.

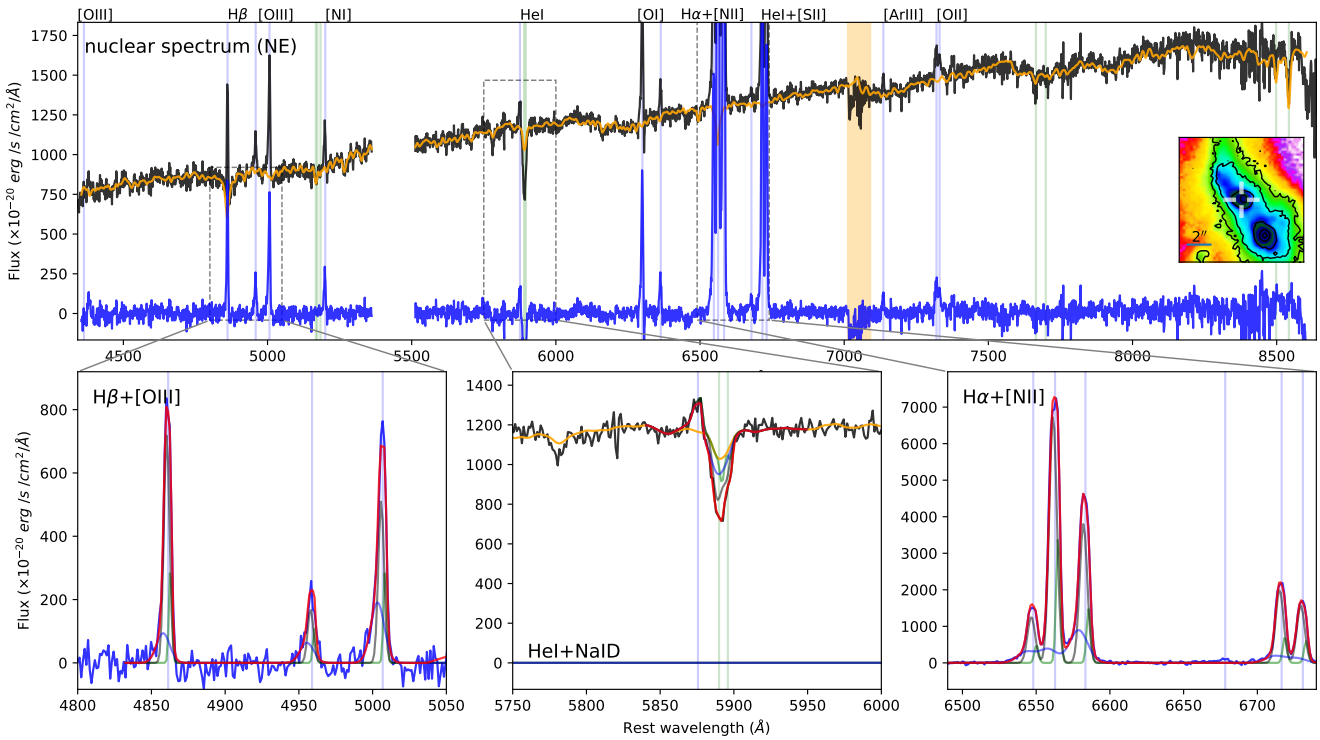

Fig. C.53. IRAS F14348-1447 NE nuclear spectrum, extracted from a circular aperture with $r < 0.4''$, with the corresponding pPXF (top panel) and multi-component (bottom insets) best-fit models. See Fig. C.4 for details.

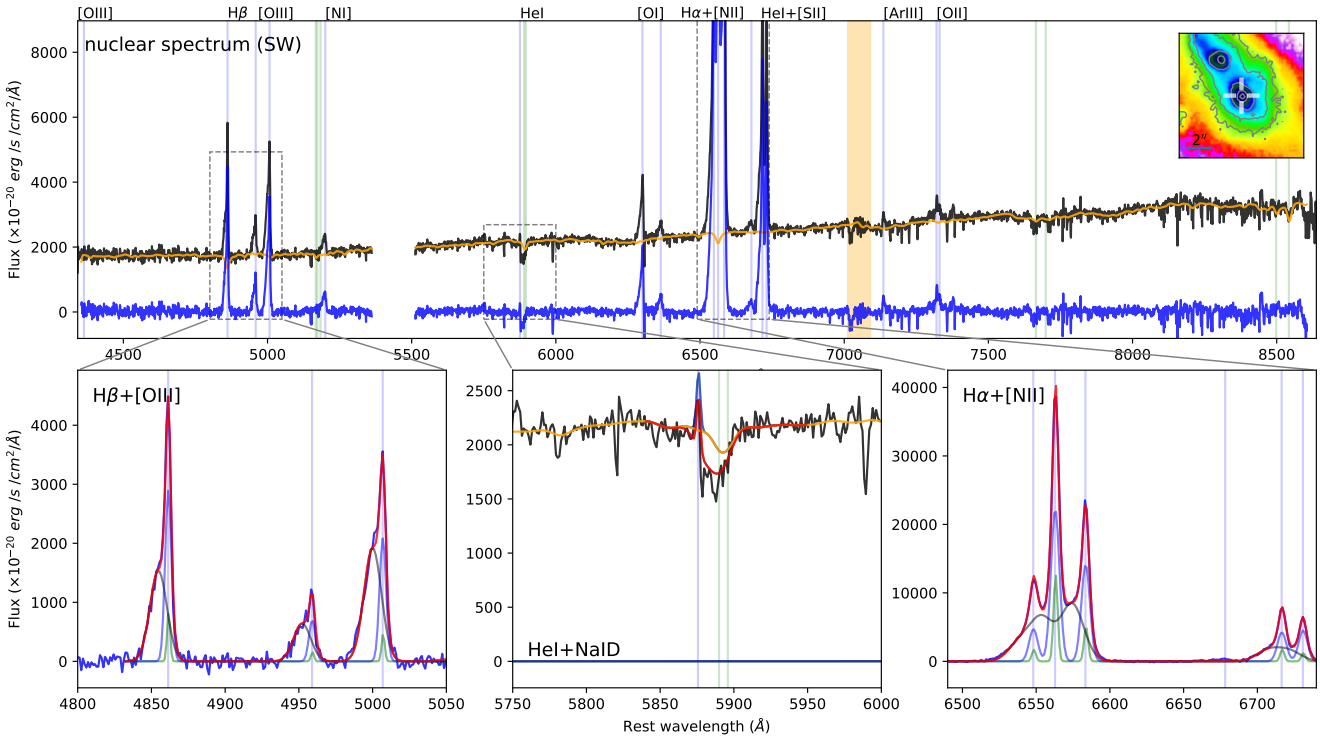

Fig. C.54. IRAS F14348-1447 SW nuclear spectrum, extracted from a circular aperture with $r < 0.4''$, with the corresponding pPXF (top panel) and multi-component (bottom insets) best-fit models. See Fig. C.4 for details.

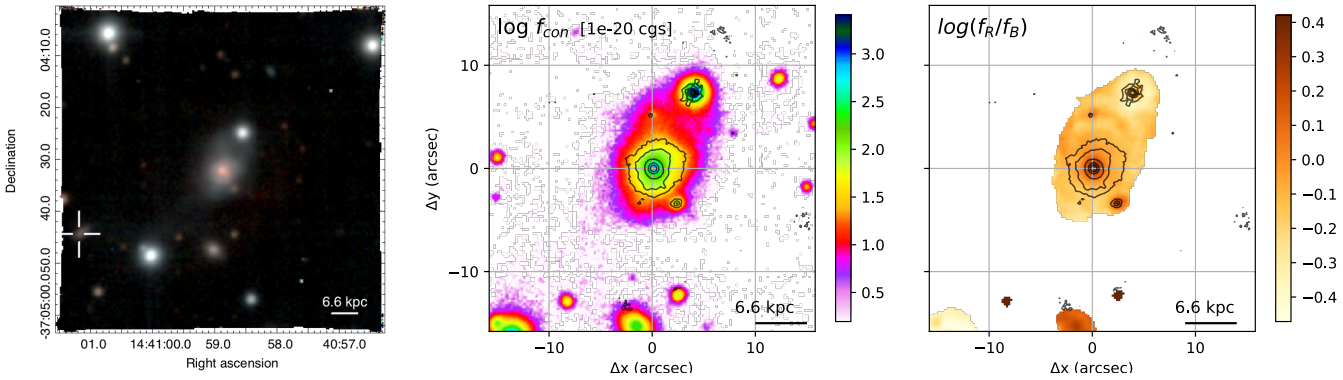

Fig. C.55. IRAS F14378-3651 images from MUSE-noAO observations with TOT = 0.47 hr. *Left*: colour composite optical image, showing [OIII] (green, from the wavelength range 4980 – 5015Å rest-frame), Hα (red, 6556 – 6572Å) and stellar continuum (blue, 4590 – 4790Å). *Centre*: red (7500 – 7600Å) continuum image from MUSE, with contours from HST/F160W. *Right*: continuum colour map obtained from MUSE, by dividing the red continuum image (central panel) by a blue image obtained collapsing the stellar emission in the range 4590 – 4790Å; contours from HST/F160W. In the left panel, we display the IRAS F14378-3651 companion galaxy with a cross marker.

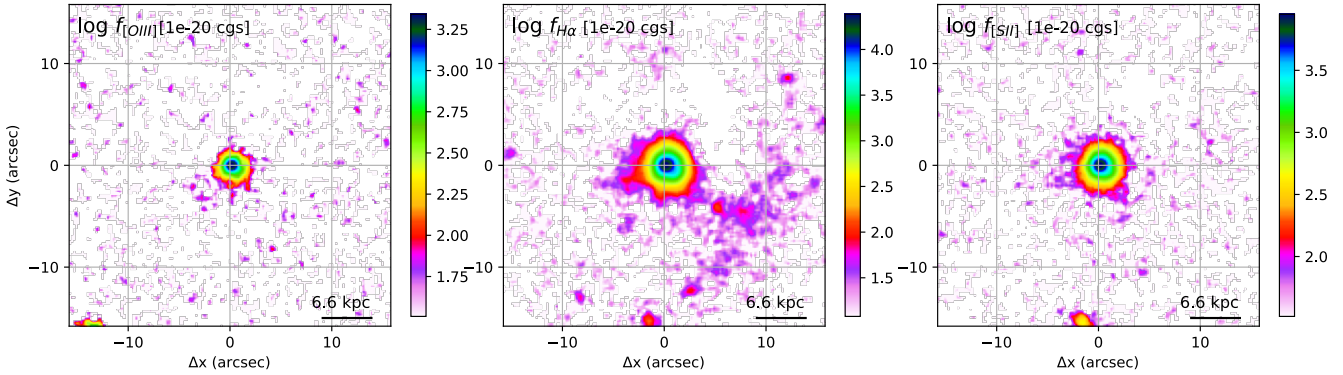

Fig. C.56. IRAS F14378-3651 emission lines images from MUSE observations. [OIII] (left, from the wavelength range 4980 – 5015Å rest-frame), Hα (centre, 6556 – 6572Å) and [SII] (right, 6695 – 6747Å) images have been obtained subtracting continuum emission using the adjacent regions at shorter and longer wavelengths with respect to the emission line systemics.

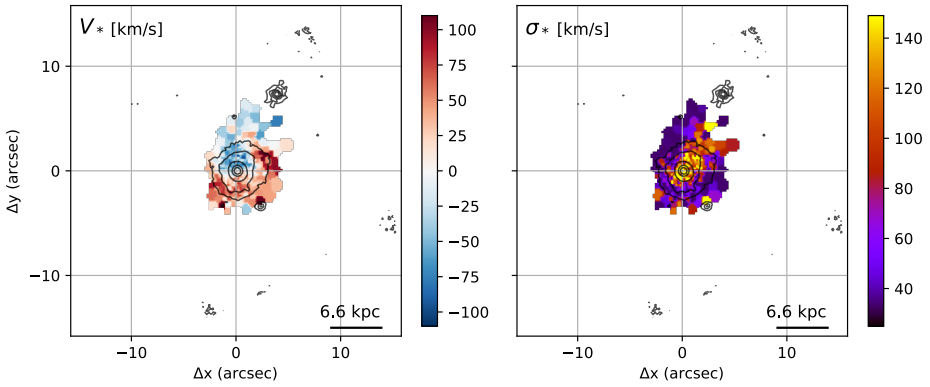

Fig. C.57. IRAS F14378-3651 stellar kinematic maps from pPXF analysis, with contours from HST/F160W. The left panel shows the stellar velocity V_*, while the right one represents the velocity dispersion σ_*.

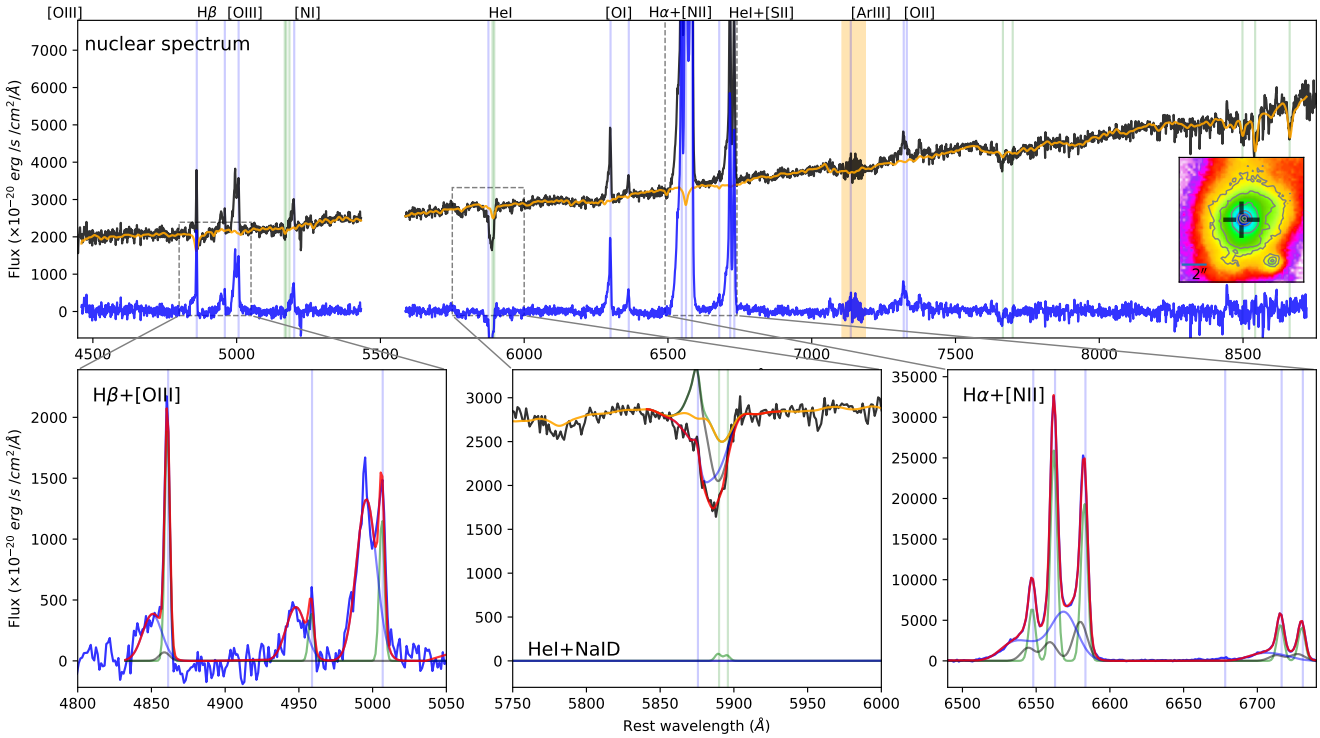

Fig. C.58. IRAS F14378-3651 nuclear spectrum, extracted from a circular aperture with $r < 0.4''$, with the corresponding pPXF (top panel) and multi-component (bottom insets) best-fit models. See Fig. C.4 for details.

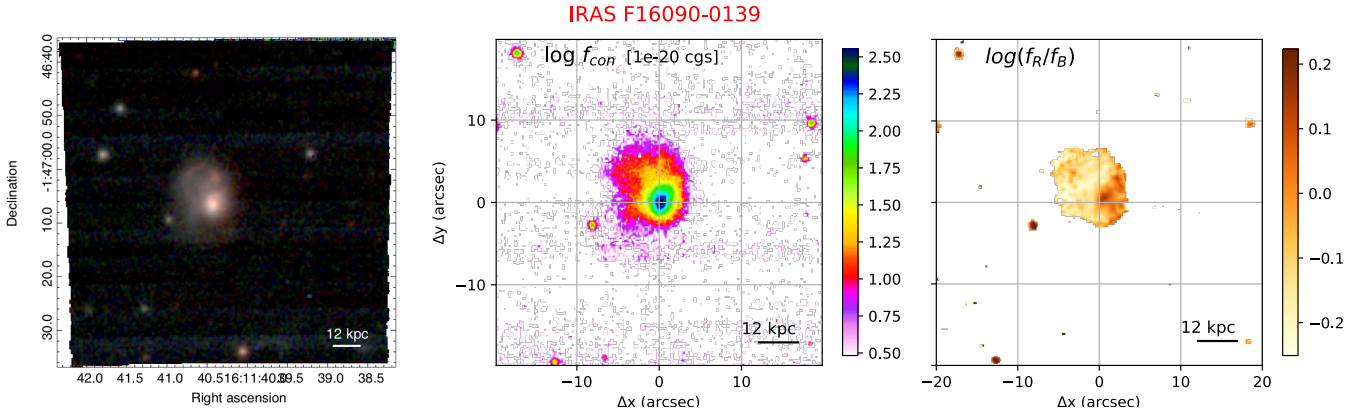

Fig. C.59. IRAS F16090-0139 images from MUSE observations with TOT = 0.17 hr. *Left*: colour composite optical image, showing [OIII] (green, from the wavelength range 4983 – 5016Å rest-frame), Hα (red, 6556 – 6573Å) and stellar continuum (blue, 4420 – 4480Å). *Centre*: red (7670 – 6730Å) continuum image from MUSE, with contours from HST/F160W. *Right*: stellar continuum colour map obtained from MUSE, by dividing the red continuum image (central panel) by a blue image obtained collapsing the stellar emission in the range 4420 – 4480Å.

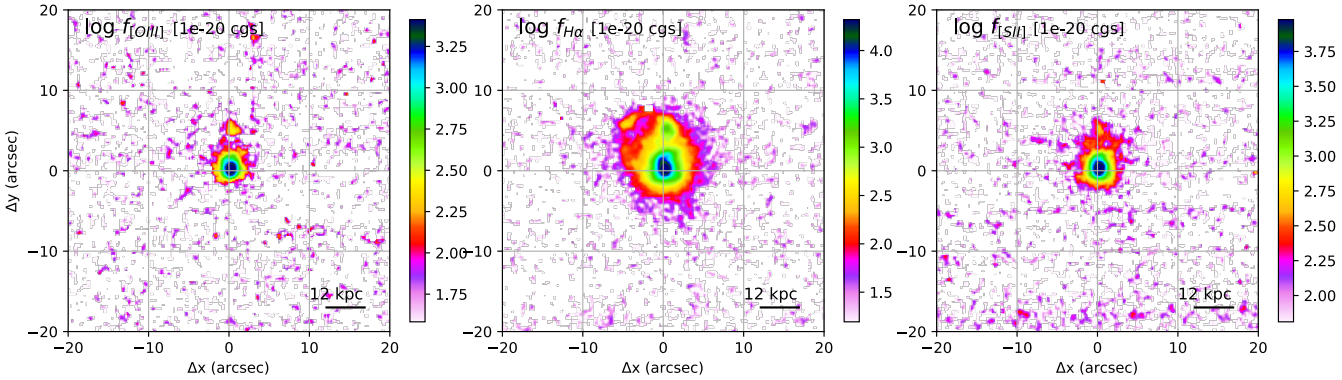

Fig. C.60. IRAS F16090-0139 emission lines images from MUSE observations. [OIII] (left, from the wavelength range 4983 – 5016Å rest-frame), Hα (centre, 6556 – 6573Å) and [SII] (right, 6690 – 6747Å) images have been obtained subtracting continuum emission using the adjacent regions at shorter and longer wavelengths with respect to the emission line systemics.

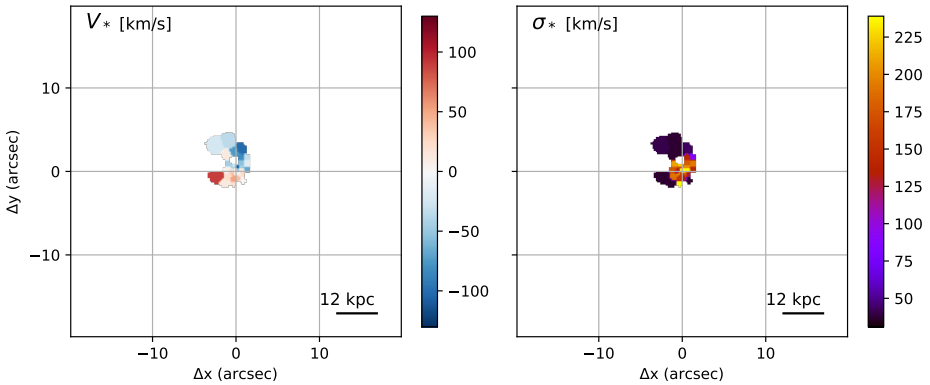

Fig. C.61. IRAS F16090-0139 stellar kinematic maps from pPXF analysis, with contours from HST/F160W. The left panel shows the stellar velocity V_*, while the right one represents the velocity dispersion σ_*.

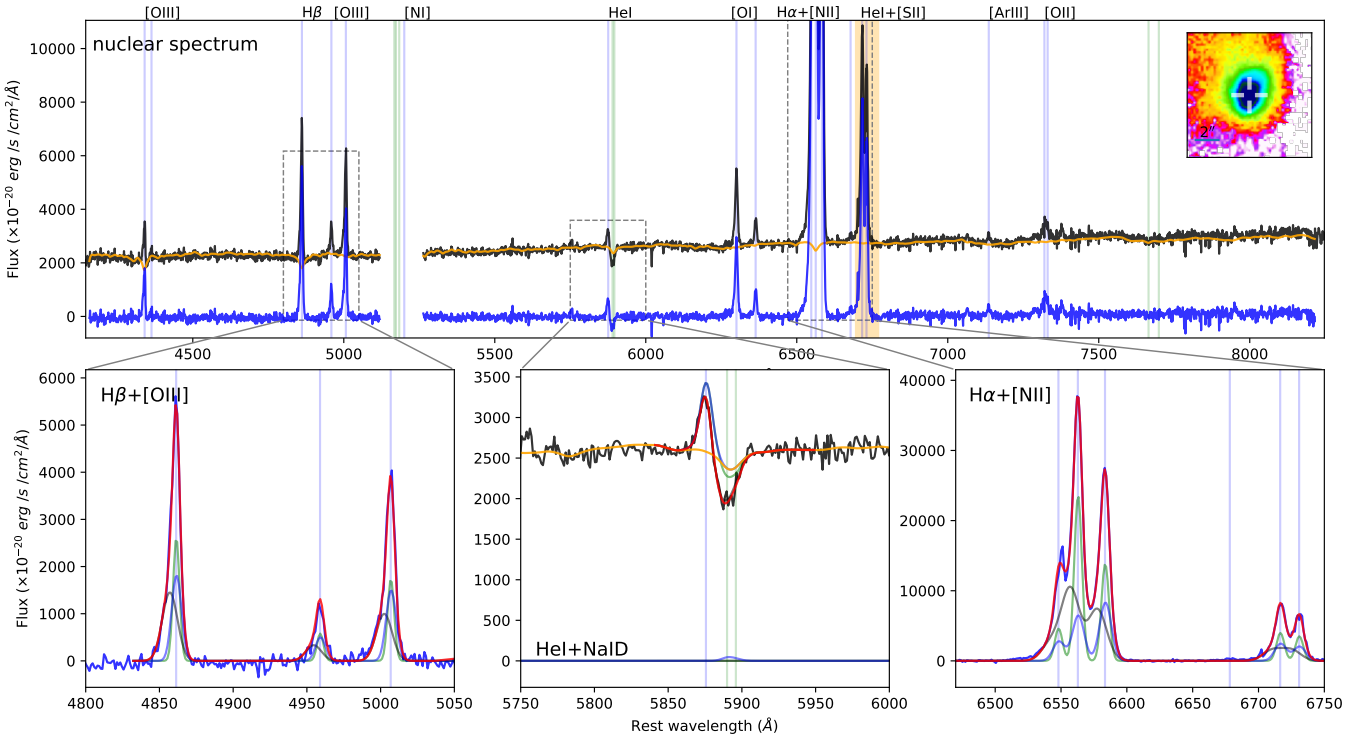

Fig. C.62. IRAS F16090-0139 nuclear spectrum, extracted from a circular aperture with $r < 0.4''$, with the corresponding pPXF (top panel) and multi-component (bottom insets) best-fit models. See Fig. C.4 for details.

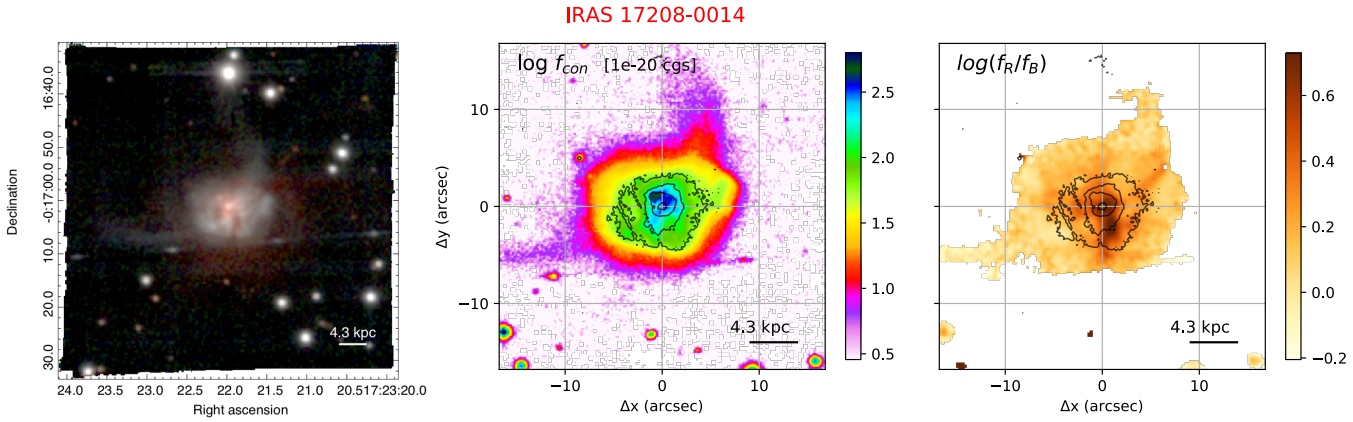

Fig. C.63. IRAS 17208-0014 images from MUSE observations with TOT = 0.39 hr. *Left*: colour composite optical image, showing [OIII] (green, from the wavelength range 4975 – 5032Å rest-frame), Hα (red, 6549 – 6576Å) and stellar continuum (blue, 4520 – 4490Å). *Centre*: red (7690 – 7760Å) continuum image from MUSE , with contours from HST/F160W. *Right*: stellar continuum colour map obtained from MUSE, by dividing the red continuum image (central panel) by a blue image obtained collapsing the stellar emission in the range 4520 – 4490Å. In all panels, the bottom part of the ULIRG shows a satellite trail resulting in three artificial blobs in the continuum emission.

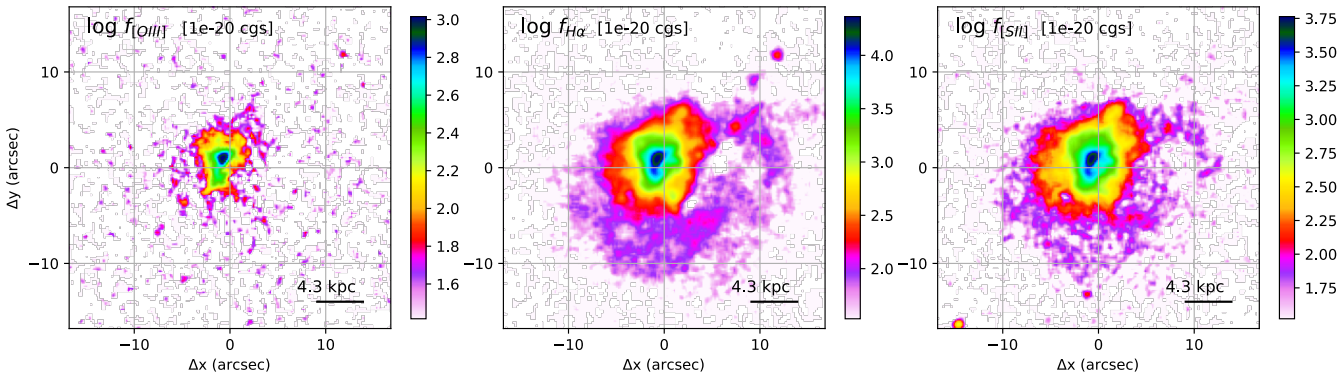

Fig. C.64. IRAS 17208-0014 emission lines images from MUSE observations. [OIII] (left, from the wavelength range 4975 – 5032Å rest-frame), Hα (centre, 6549 – 6576Å) and [SII] (right, 6695 – 6749Å) images have been obtained subtracting continuum emission using the adjacent regions at shorter and longer wavelengths with respect to the emission line systemics.

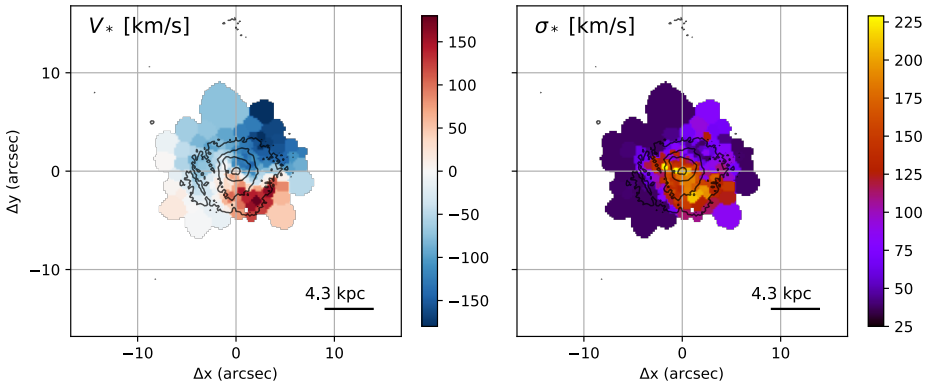

Fig. C.65. IRAS 17208-0014 stellar kinematic maps from pPXF analysis, with contours from HST/F160W. The left panel shows the stellar velocity V_*, while the right one represents the velocity dispersion σ_*.

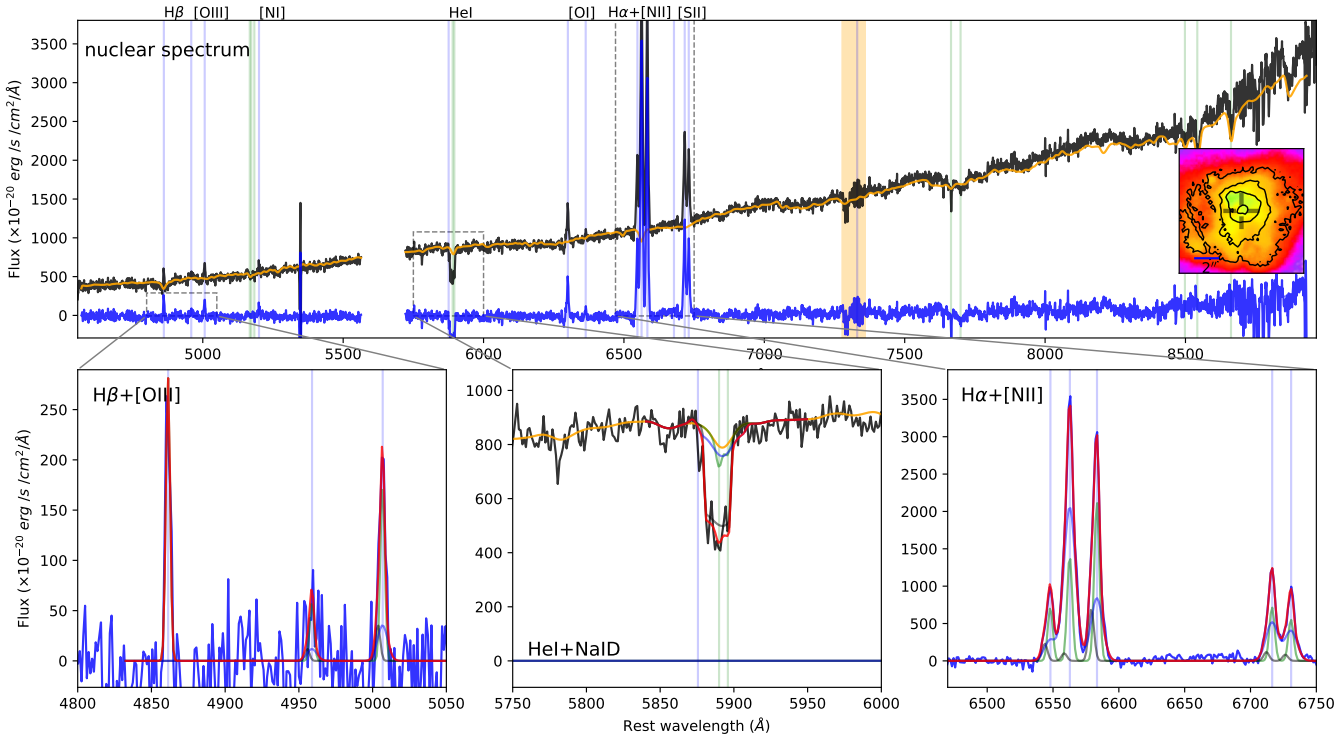

Fig. C.66. IRAS 17208-0014 nuclear spectrum, extracted from a circular aperture with $r < 0.4''$, with the corresponding pPXF (top panel) and multi-component (bottom insets) best-fit models. See Fig. C.4 for details.

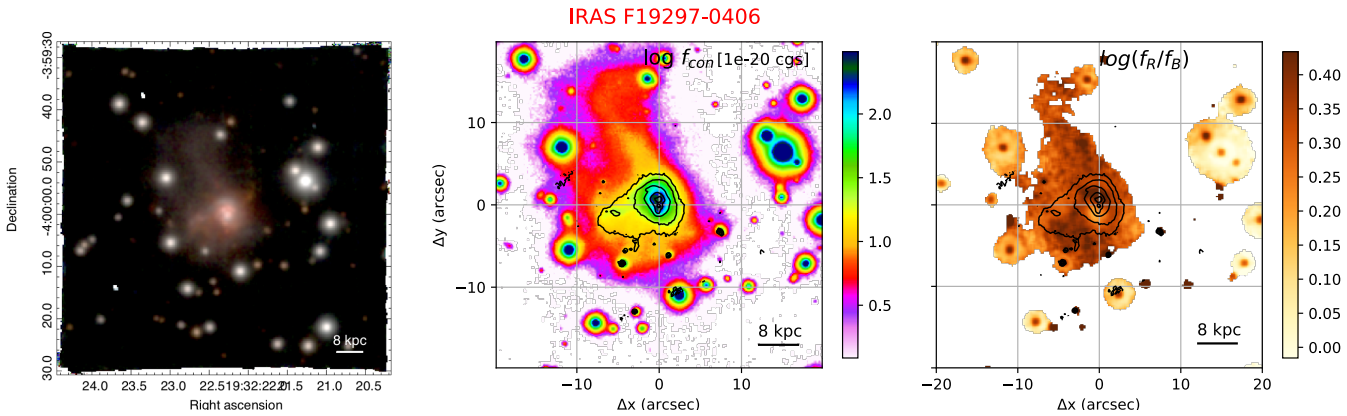

Fig. C.67. IRAS F19297-0406 images from MUSE observations with TOT = 2.04 hr. *Left*: colour composite optical image, showing [OIII] (green, from the wavelength range 4991 – 5021Å rest-frame), Hα (red, 6557 – 6579Å) and stellar continuum (blue, 4550 – 4620Å). *Centre*: red (7440 – 7590Å) continuum image from MUSE , with contours from HST/F160W. *Right*: stellar continuum colour map obtained from MUSE, by dividing the red continuum image (central panel) by a blue image obtained collapsing the stellar emission in the range 4550 – 4620Å.

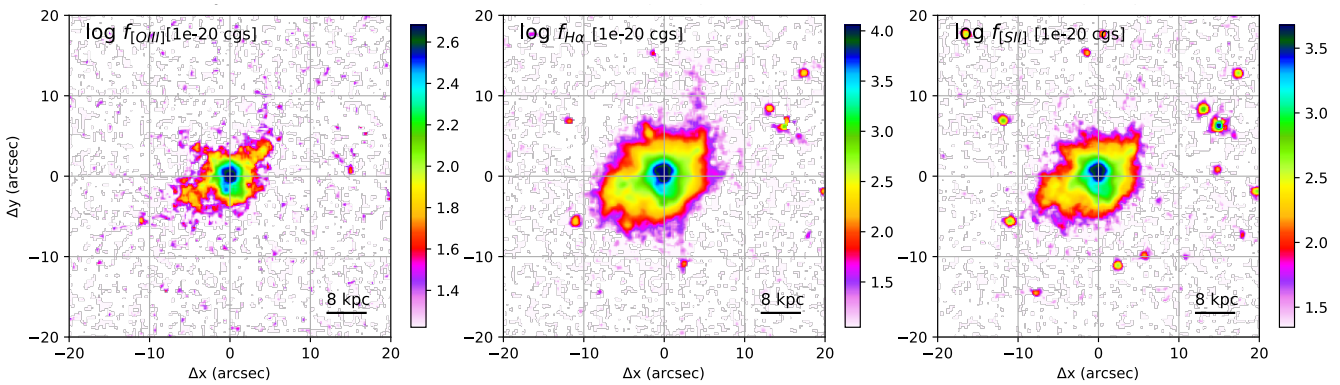

Fig. C.68. IRAS F19297-0406 emission lines images from MUSE observations. [OIII] (left, from the wavelength range 4991 – 5021Å rest-frame), Hα (centre, 6557 – 6579Å) and [SII] (right, 6700 – 6752Å) images have been obtained subtracting continuum emission using the adjacent regions at shorter and longer wavelengths with respect to the emission line systemics.

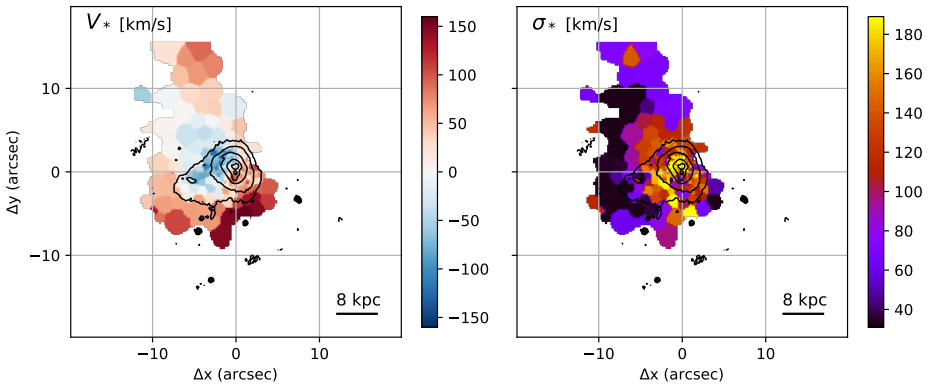

Fig. C.69. IRAS F19297-0406 stellar kinematic maps from pPXF analysis, with contours from HST/F160W. The left panel shows the stellar velocity V_*, while the right one represents the velocity dispersion σ_*.

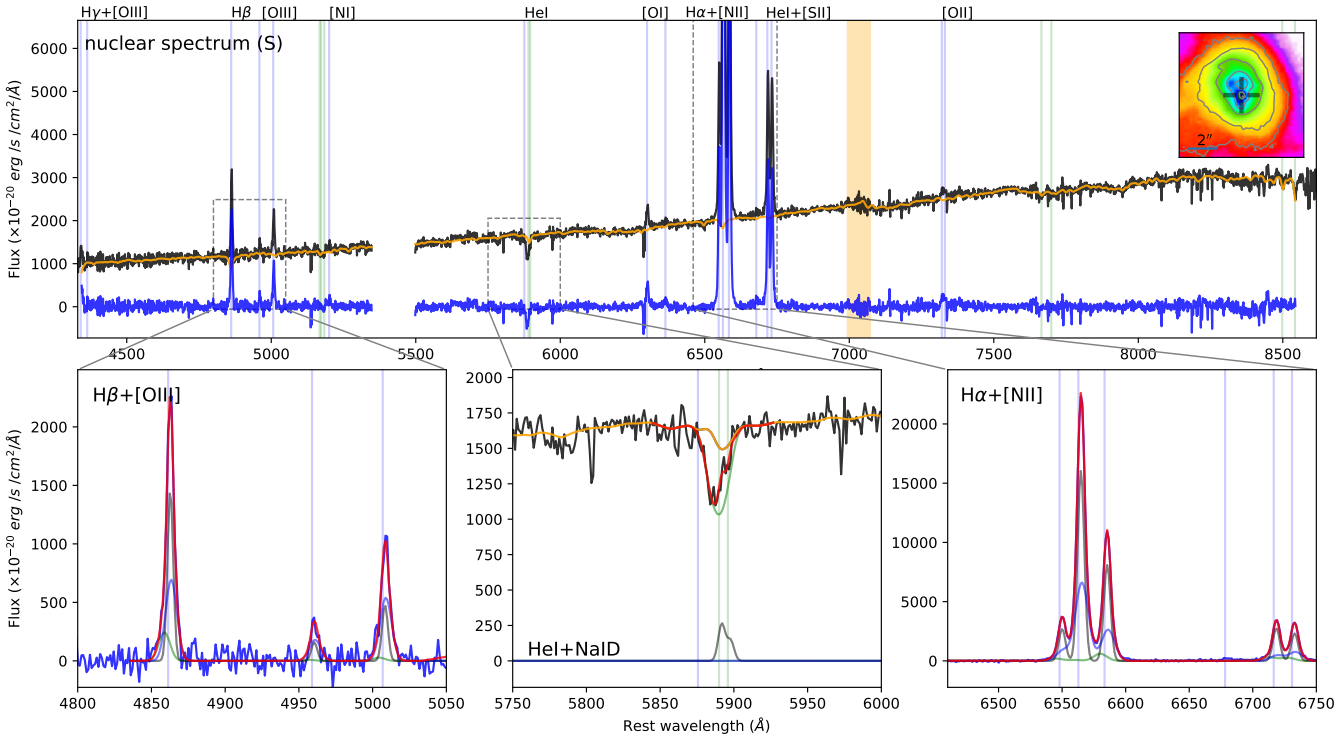

Fig. C.70. IRAS F19297-0406 (S) nuclear spectrum, extracted from a circular aperture with $r < 0.4''$, with the corresponding pPXF (top panel) and multi-component (bottom insets) best-fit models. See Fig. C.4 for details.

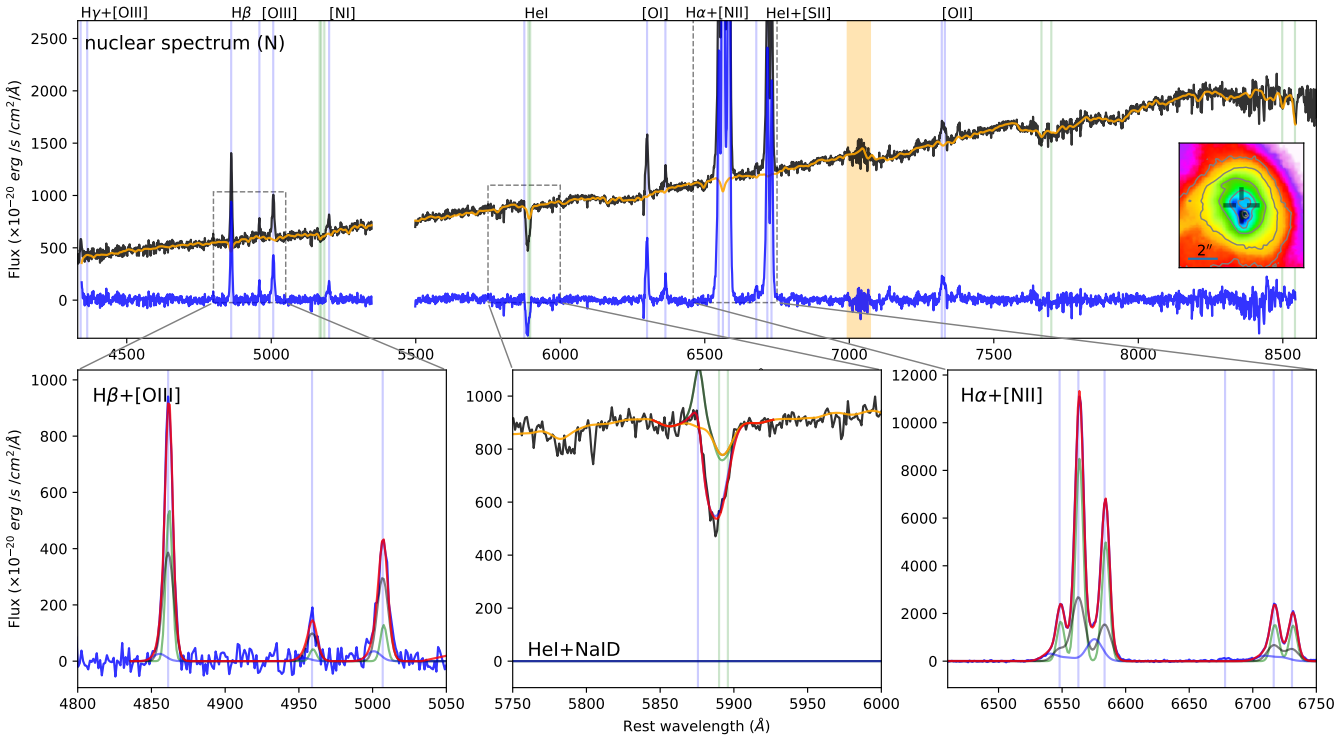

Fig. C.71. IRAS F19297-0406 (N) nuclear spectrum, extracted from a circular aperture with $r < 0.4''$, with the corresponding pPXF (top panel) and multi-component (bottom insets) best-fit models. See Fig. C.4 for details.

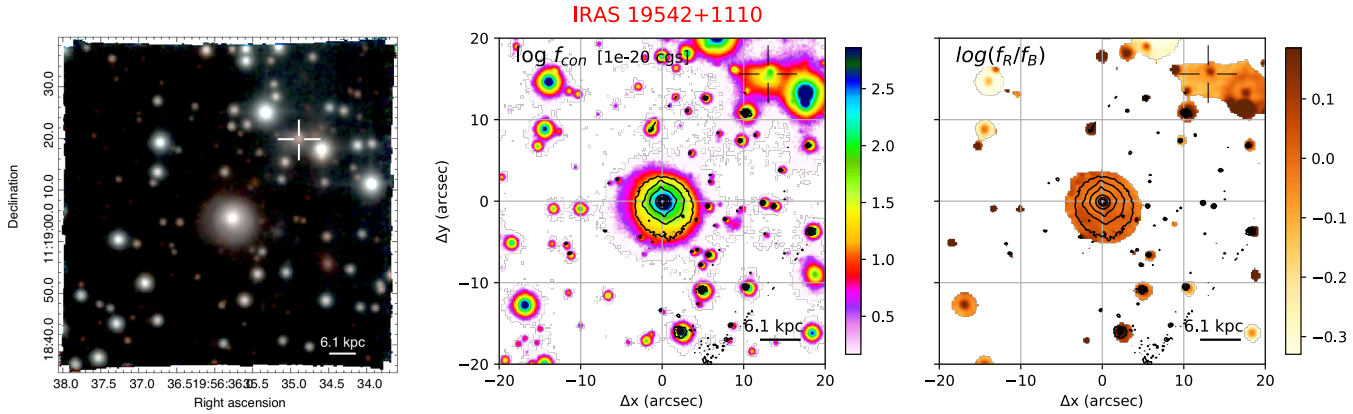

Fig. C.72. IRAS 19542+1110 images from MUSE observations with TOT = 2.04 hr. *Left*: colour composite optical image, showing [OIII] (green, from the wavelength range 4985 – 5016Å rest-frame), Hα (red, 6552 – 6573Å) and stellar continuum (blue, 4630 – 4740Å). *Centre*: red (7650 – 7750Å) continuum image from MUSE , with contours from HST/F160W. *Right*: stellar continuum colour map obtained from MUSE, by dividing the red continuum image (central panel) by a blue image obtained collapsing the continuum emission in the range 4630 – 4740Å; contours from HST/F160W. In all panels, we display the companion galaxy of IRAS 19542+1110 with a cross marker.

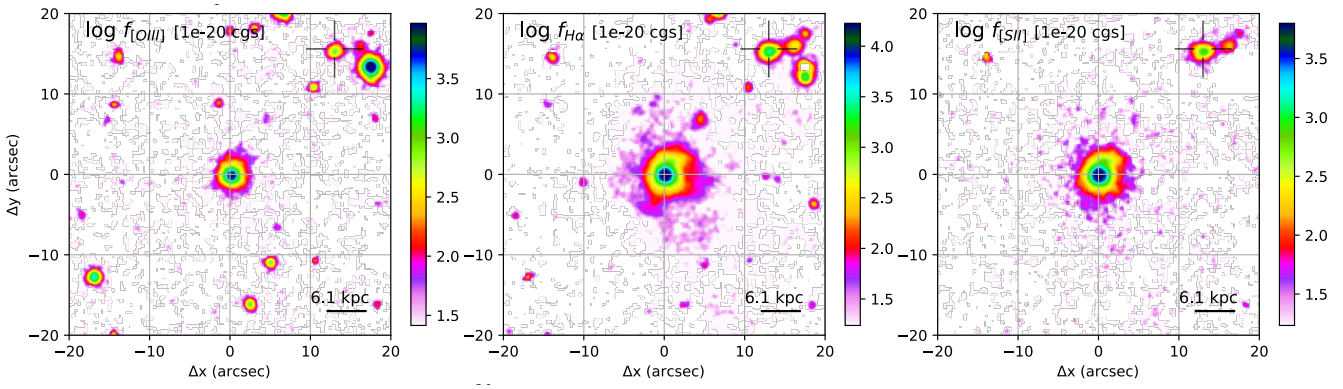

Fig. C.73. IRAS 19542+1110 emission lines images from MUSE observations. [OIII] (left, from the wavelength range 4985 – 5016Å rest-frame), Hα (centre, 6552 – 6573Å) and [SII] (right, 6700 – 6744Å) images have been obtained subtracting continuum emission using the adjacent regions at shorter and longer wavelengths with respect to the emission line systemics.

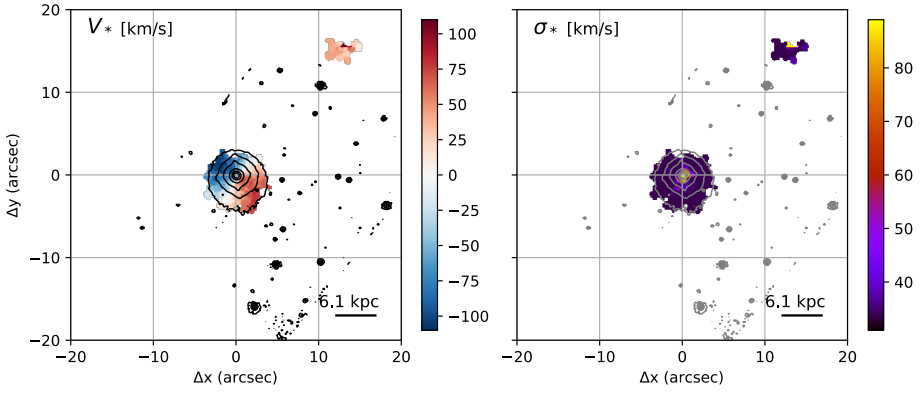

Fig. C.74. IRAS 19542+1110 stellar kinematic maps from pPXF analysis, with contours from HST/F160W. The left panel shows the stellar velocity V_*, while the right one represents the velocity dispersion σ_*.

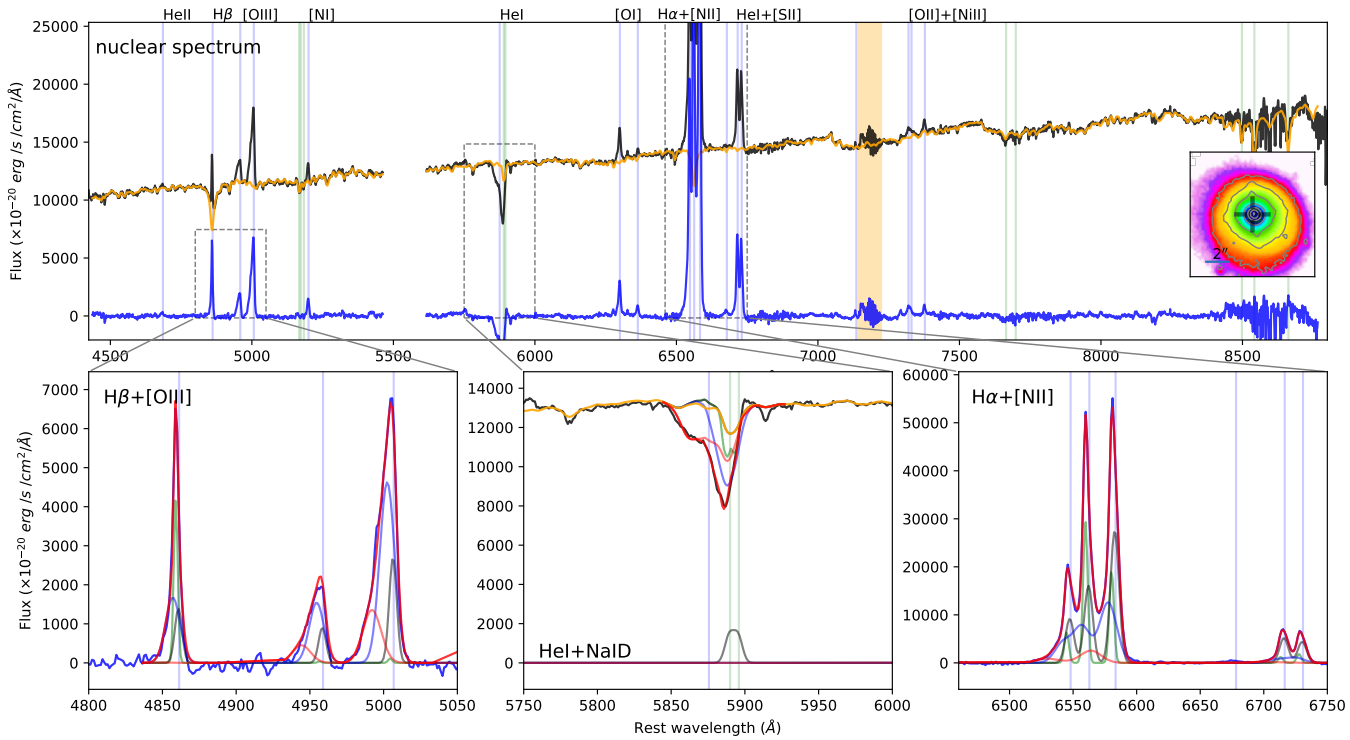

Fig. C.75. IRAS 19542+1110 nuclear spectrum, extracted from a circular aperture with $r < 0.4''$, with the corresponding pPXF (top panel) and multi-component (bottom insets) best-fit models. See Fig. C.4 for details.

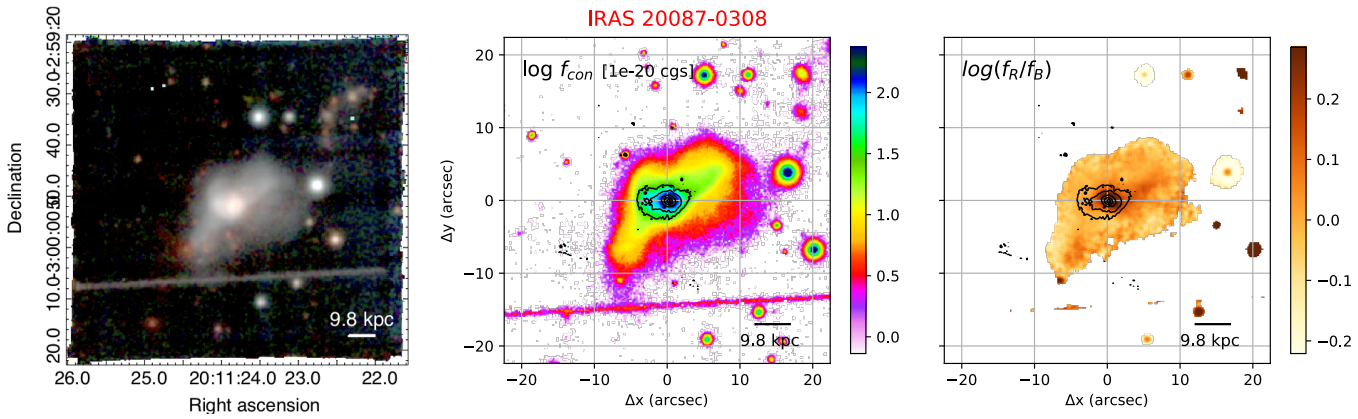

Fig. C.76. IRAS 20087-0308 images from MUSE observations with TOT = 2.04 hr. *Left*: colour composite optical image, showing [OIII] (green, from the wavelength range 4986 – 5020Å rest-frame), Hα (red, 6555 – 6574Å) and continuum (blue, 4600 – 4700Å). *Centre*: red (7780 – 7880Å) continuum image from MUSE , with contours from HST/F160W. *Right*: stellar continuum colour map obtained from MUSE, by dividing the red continuum image (central panel) by a blue image obtained collapsing the stellar emission in the range 4600 – 4700Å; contours from HST/F160W. In all panels, the bottom part of the FOV shows a satellite trail.

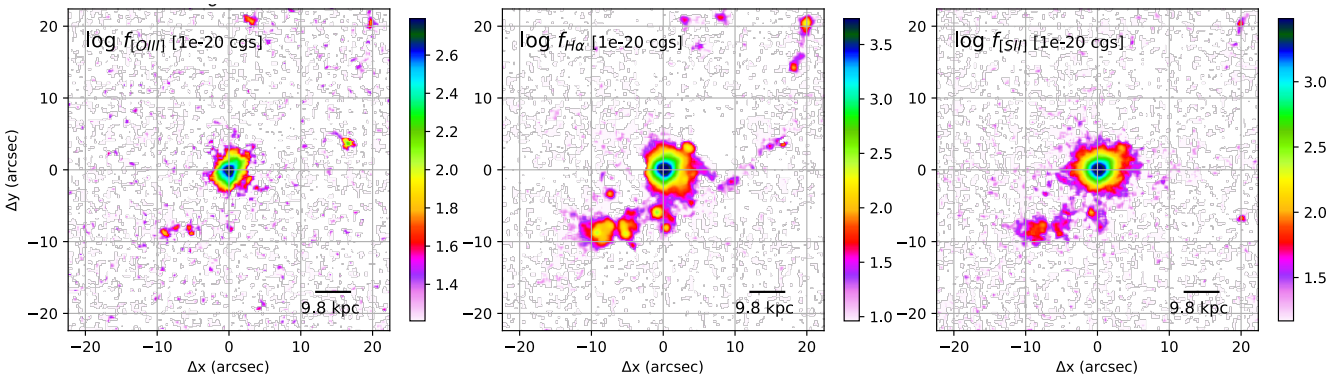

Fig. C.77. IRAS 20087-0308 emission lines images from MUSE observations. [OIII] (left, from the wavelength range 4986 – 5020Å rest-frame), Hα (centre, 6555 – 6574Å) and [SII] (right, 6700 – 6747Å) images have been obtained subtracting continuum emission using the adjacent regions at shorter and longer wavelengths with respect to the emission line systemics.

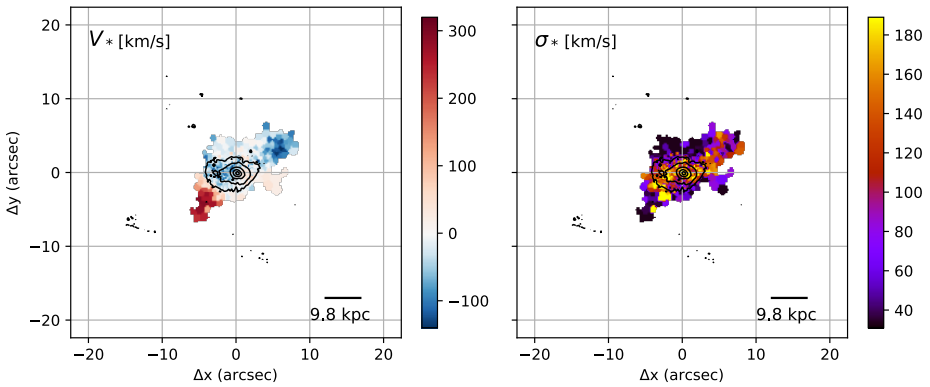

Fig. C.78. IRAS 20087-0308 stellar kinematic maps from pPXF analysis, with contours from HST/F160W. The left panel shows the stellar velocity V_*, while the right one represent the velocity dispersion σ_*.

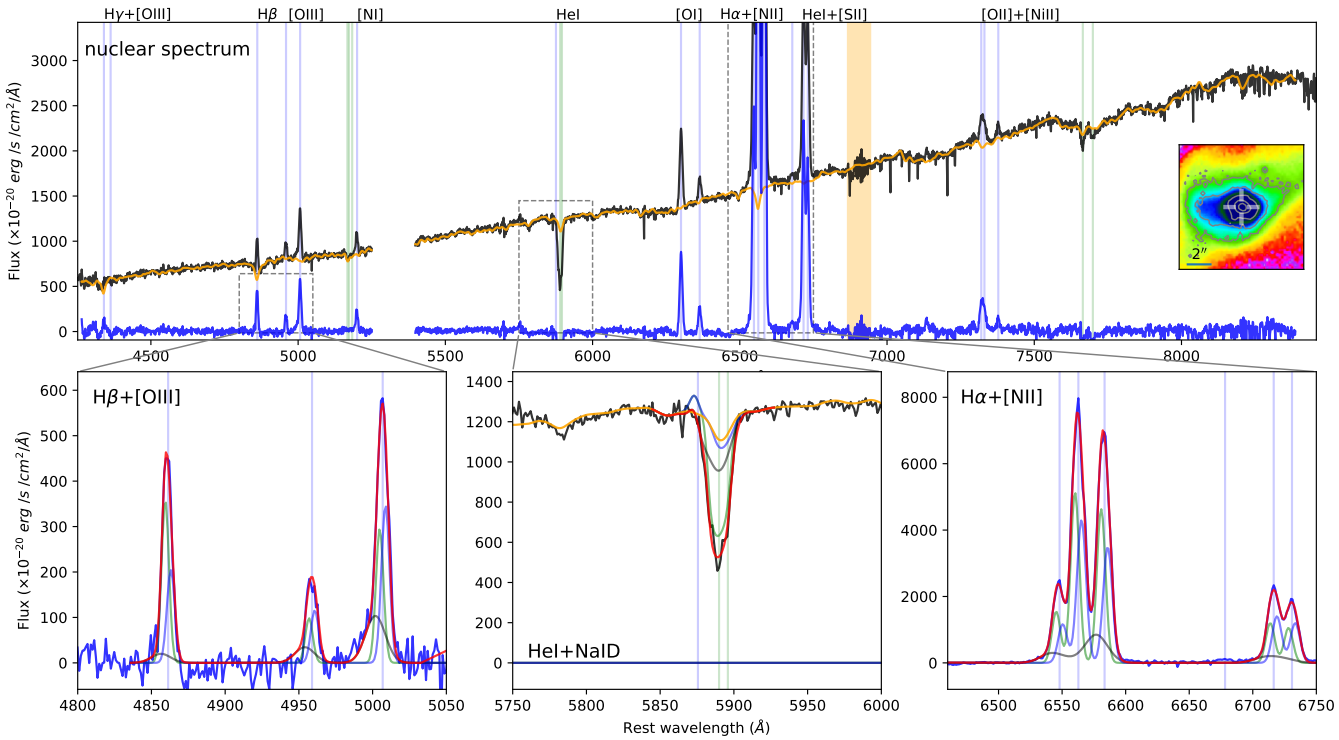

Fig. C.79. IRAS 20087-0308 nuclear spectrum, extracted from a circular aperture with $r < 0.4''$, with the corresponding pPXF (top panel) and multi-component (bottom insets) best-fit models. See Fig. C.4 for details.

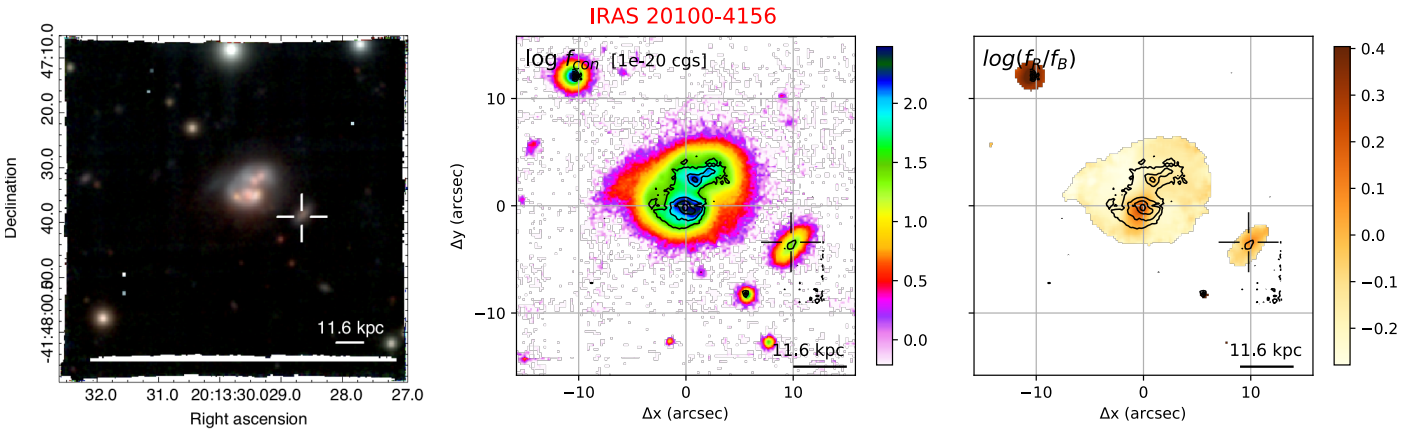

Fig. C.80. IRAS 20100-4156 images from MUSE observations with TOT = 2.04 hr. *Left*: colour composite optical image, showing [OIII] (green, from the wavelength range 4985 – 5022Å rest-frame), Hα (red, 6554 – 6579Å) and continuum (blue, 4450 – 4600Å). *Centre*: red (7500 – 7700Å) continuum image from MUSE , with contours from HST/F160W. *Right*: stellar continuum colour map obtained from MUSE, by dividing the red continuum image (central panel) by a blue image obtained collapsing the stellar emission in the range 4450 – 4600Å; contours from HST/F160W. In all panels, we display the IRAS 20100-4156 companion with a cross marker.

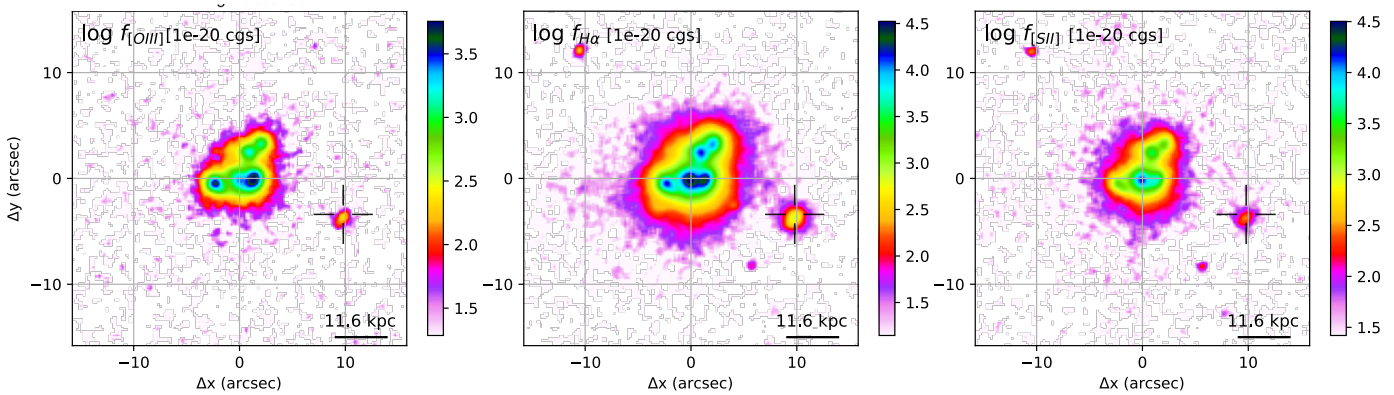

Fig. C.81. IRAS 20100-4156 emission lines images from MUSE observations. [OIII] (left, from the wavelength range 4985 – 5022Å rest-frame), Hα (centre, 6554 – 6579Å) and [SII] (right, 6691 – 6743Å) images have been obtained subtracting continuum emission using the adjacent regions at shorter and longer wavelengths with respect to the emission line systemics. In all panels, we display the 20100-4156 companion with a cross marker.

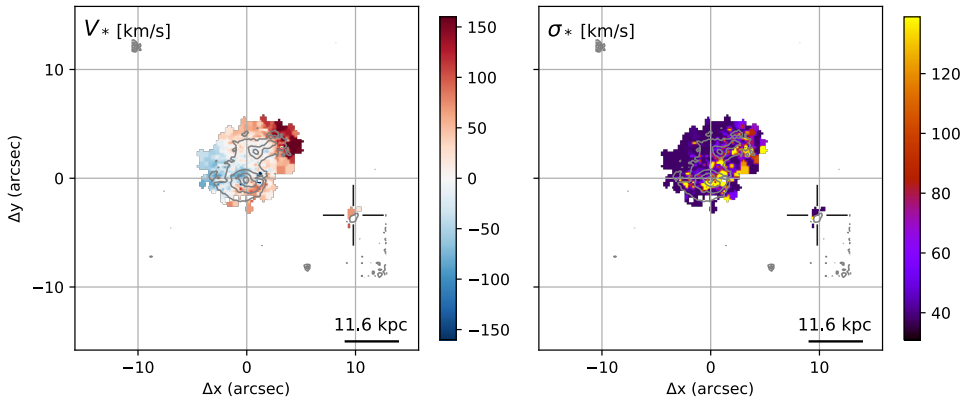

Fig. C.82. IRAS 20100-4156 stellar kinematic maps from pPXF analysis, with contours from HST/F160W. The left panel shows the stellar velocity V_*, while the right one represent the velocity dispersion σ_*.

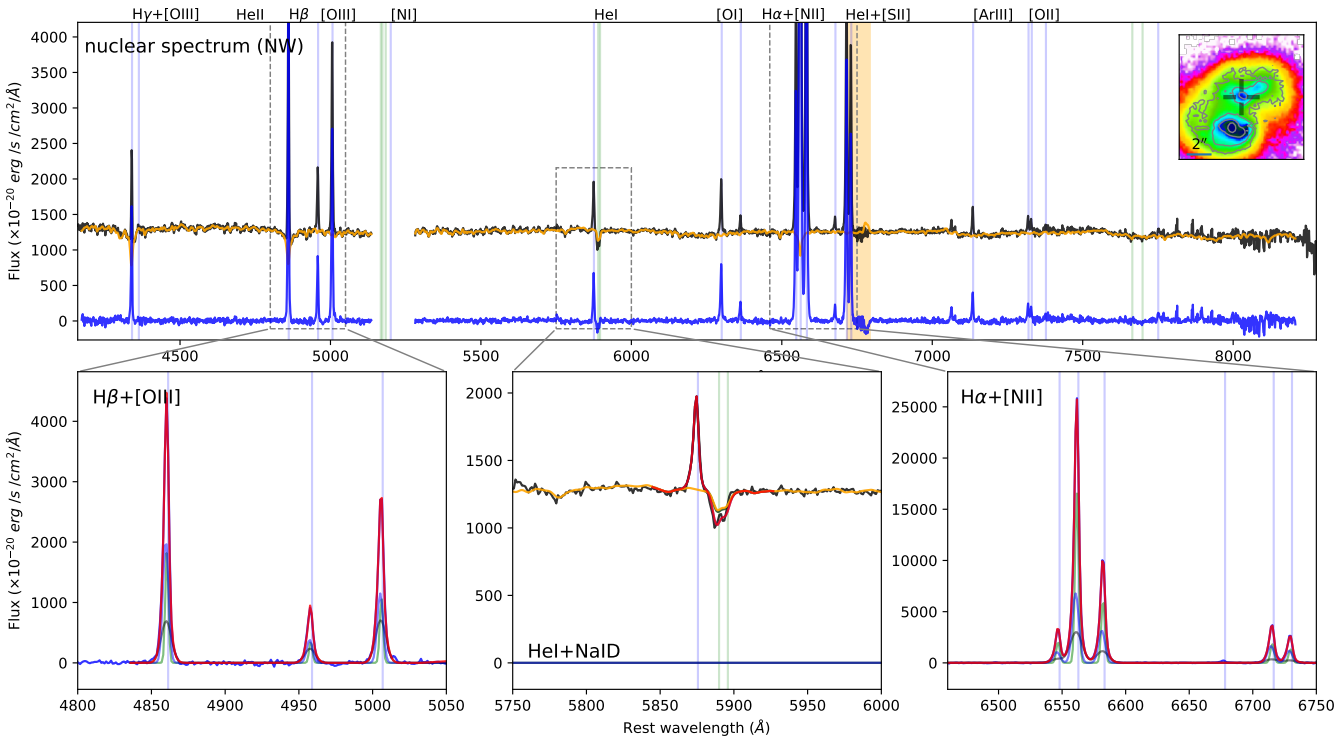

Fig. C.83. IRAS 20100-4156 NW nuclear spectrum, extracted from a circular aperture with $r < 0.4''$, with the corresponding pPXF (top panel) and multi-component (bottom insets) best-fit models. See Fig. C.4 for details.

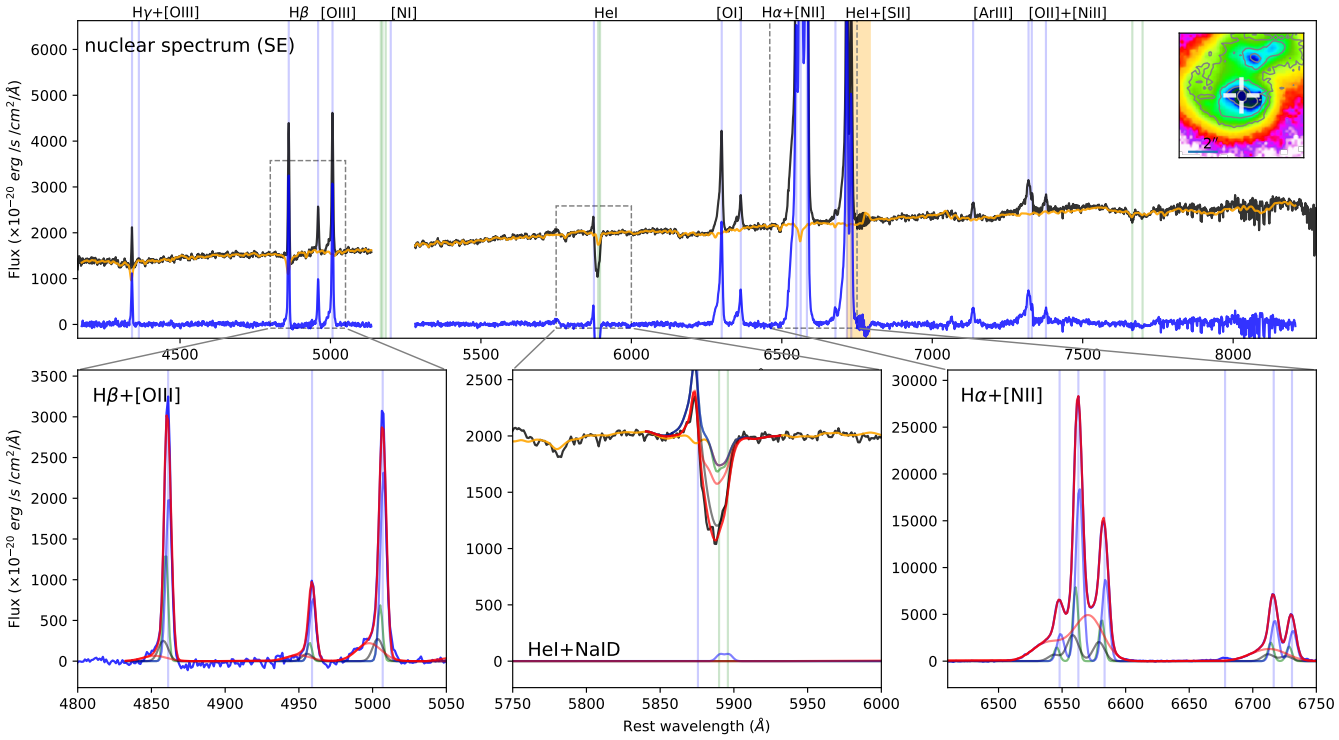

Fig. C.84. IRAS 20100-4156 SE nuclear spectrum, extracted from a circular aperture with $r < 0.4''$, with the corresponding pPXF (top panel) and multi-component (bottom insets) best-fit models. See Fig. C.4 for details.

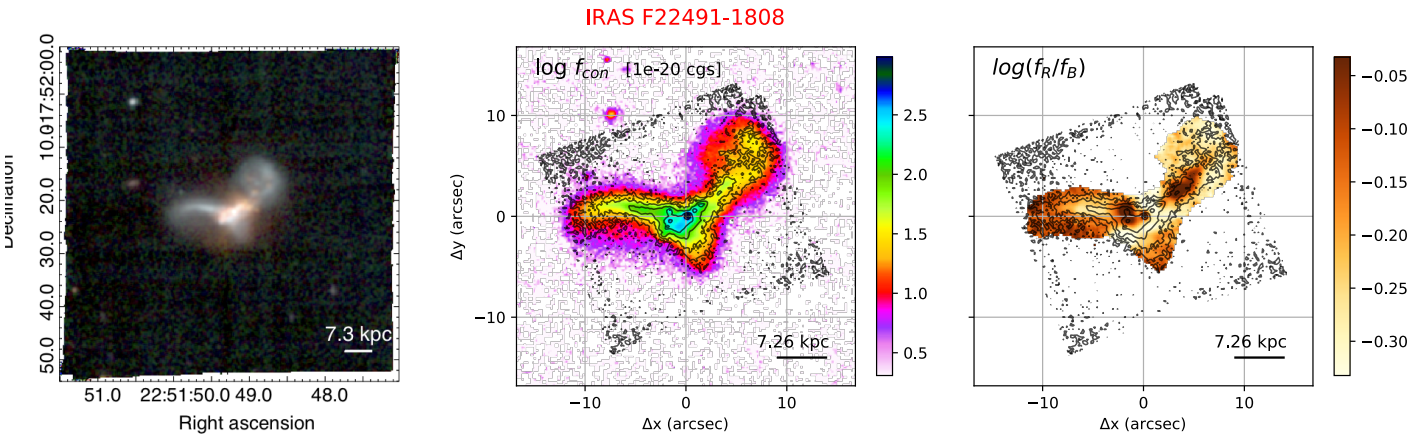

Fig. C.85. IRAS F22491-1808 images from MUSE observations with TOT = 0.41 hr. *Left*: colour composite optical image, showing [OIII] (green, from the wavelength range 4998 – 5017Å rest-frame), Hα (red, 6556 – 6575Å) and stellar continuum (blue, 4460 – 4740Å). *Centre*: red (8020 – 8120Å) stellar continuum image from MUSE, with contours from HST/F160W. *Right*: stellar continuum colour map obtained from MUSE, by dividing the red continuum image (central panle) by a blue image obtained collapsing the stellar emission in the range 4460 – 4740Å; contours from HST/F160W.

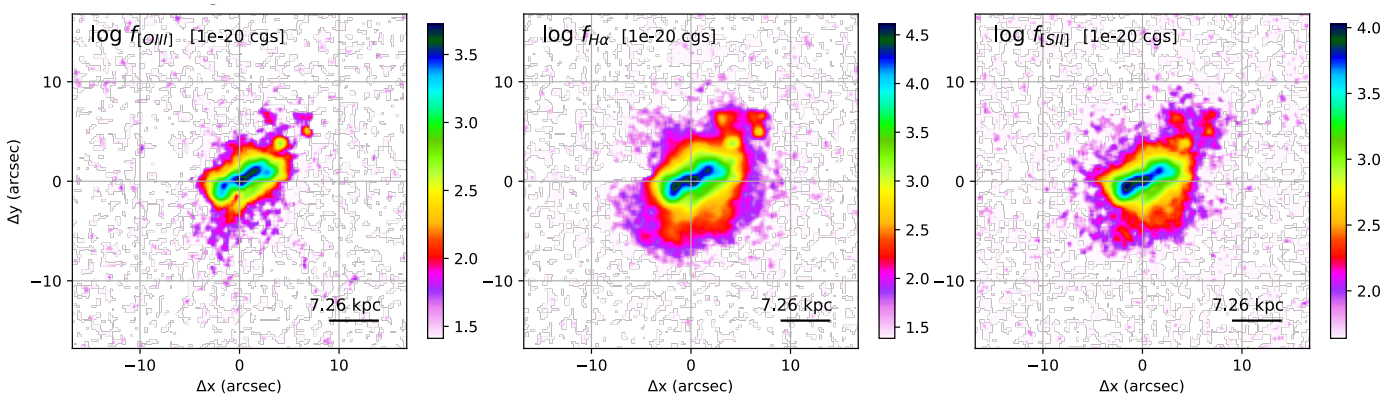

Fig. C.86. IRAS F22491-1808 emission lines images from MUSE observations. [OIII] (left, from the wavelength range 4998 – 5017Å rest-frame), Hα (centre, 6556 – 6575Å) and [SII] (right, 6707 – 6739Å) images have been obtained subtracting continuum emission using the adjacent regions at shorter and longer wavelengths with respect to the emission line systemics.

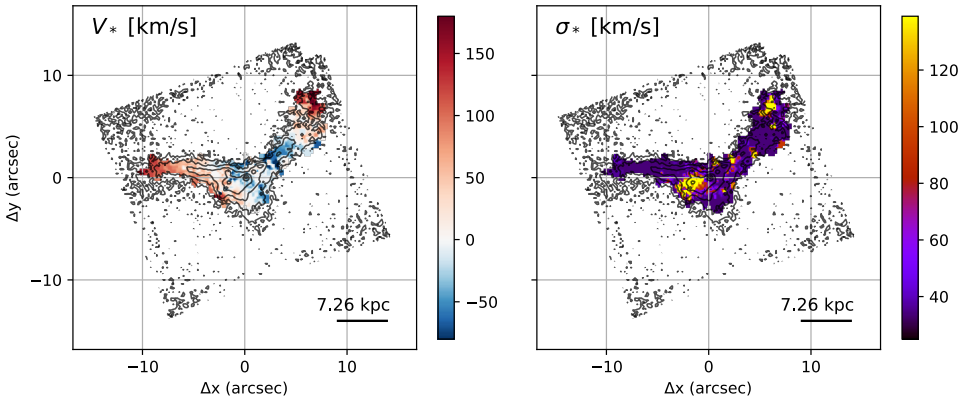

Fig. C.87. IRAS F22491-1808 stellar kinematic maps from pPXF analysis, with contours from HST/F160W. The left panel shows the stellar velocity V_*, while the right one represents the velocity dispersion σ_*.

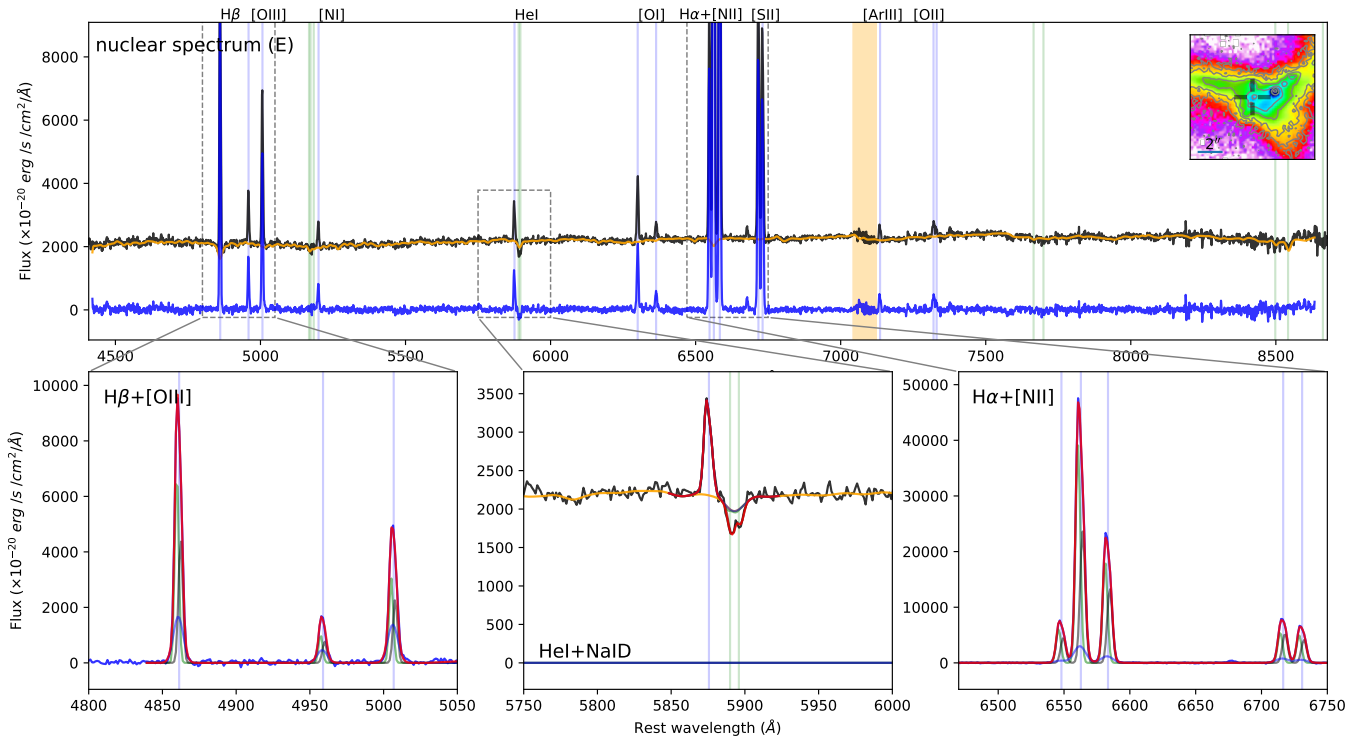

Fig. C.88. IRAS F22491-1808 E nuclear spectrum, extracted from a circular aperture with $r < 0.4''$, with the corresponding pPXF (top panel) and multi-component (bottom insets) best-fit models. See Fig. C.4 for details.

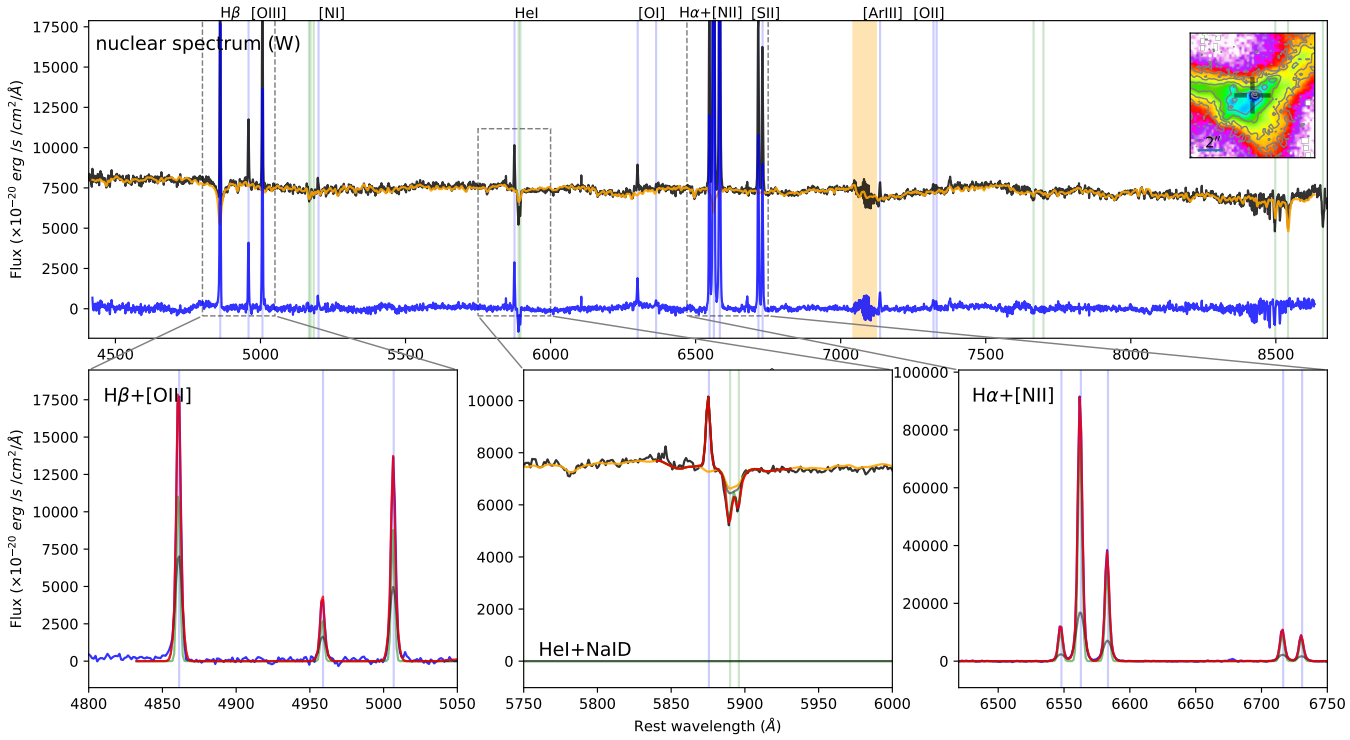

Fig. C.89. IRAS F22491-1808 W nuclear spectrum, extracted from a circular aperture with $r < 0.4''$, with the corresponding pPXF (top panel) and multi-component (bottom insets) best-fit models. See Fig. C.4 for details.